STARS

Electronic Theses and Dissertations, 2020-

2020

Climatic and Topologic Controls on the Complexity of River Networks

Sevil Ranjbar Moshfeghi
University of Central Florida

Find similar works at: https://stars.library.ucf.edu/etd2020

University of Central Florida Libraries http://library.ucf.edu

STARS Citation

University of Central Florida

STARS

Showcase of Text, Archives, Research & Scholarship

CLIMATIC AND TOPOLOGIC CONTROLS ON THE COMPLEXITY OF RIVER NETWORKS

by

SEVIL RANJBAR
B.S University of Tabriz, 2011
M.Sc University of Tabriz, 2014

A dissertation submitted in partial fulfillment of the requirements
for the degree of Doctor of Philosophy
in the Department of Civil, Environmental and Construction Engineering
in the College of Engineering and Computer Science
at the University of Central Florida
Orlando, Florida

Summer Term
2020

Major Professor: Arvind Singh

ABSTRACT

The emergence and evolution of channel networks are controlled by the competition between the hillslopes and fluvial processes on the landscape. Investigating the geomorphic and topologic properties of these networks is important for developing predictive models describing the network dynamics under changing environment as well as for quantifying the roles of processes in creating distinct patterns of channel networks. In this dissertation, the response of landscapes to changing climatic forcing via numerical-modeling and field observations was investigated. A new framework was proposed to evaluate the complexity of catchments using two different representations of channel networks. The structural complexity was studied using the width function, which characterizes the spatial arrangement of channels. Whereas, the functional complexity was explored using the incremental area function, capturing the patterns of transport of fluxes. Our analysis reveals stronger controls of topological connectivity on the functional complexity than on structural complexity, indicating that the unchannelized surface (hillslope) contributes to the increase of heterogeneity in transport processes.

Furthermore, the channel network structure was investigated using a physically-based numerical landscape evolution model for varying hillslope and fluvial processes. Different magnitudes of soil transport (D) and fluvial incision (K) coefficients represent different magnitudes of hillslope and fluvial processes. We show that different combinations of D and K result in distinct branching structure in landscapes. For example, for smaller D

and K combinations (mimicking dry climate), a higher number of branching channels was observed. Whereas, for larger D and K combinations (mimicking humid climate), a higher number of side-branching channels is obtained. These results are consistent with the field observations suggesting that varying climatic conditions imprint distinct signatures on the branching structure of channel networks.

To my lovely parents

For all your support and encouragements

ACKNOWLEDGMENT

TABLE OF CONTENTS

LIST OF FIGURES

Figure 2. A sample width function series $W(x)$ used to demonstrate the steps involved in the sample entropy calculations. In this example $m = 2$ [*Costa et al.*, 2002; 2005]. The first m-point pattern (sequence) is represented by $w1$-$w2$ (red-green) and $m+1$-point pattern by $w1$-$w2$-$w3$ (red-green-blue). The dashed lines around the data points represent $w1 \pm r$ (red), $w2 \pm r$ (green), and $w3 \pm r$ (blue), and indicate the tolerance for counting similar patterns. For the pattern with length $m = 2$ where the first point is $w1$ (red) and the second point is $w2$ (green), we count all the $w1$-$w2$ sequences, i.e. we count the number of times that a green data point appears right after a red data point. The number of the pairs that match the first 2-point pattern is referred to as Dm and in this example $Dm = 6$. Next, we add another point to the previously considered m-point pattern. This 3-point pattern ($m+1$ or longer pattern) can be represented by the sequence of $w1$-$w2$-$w3$ (shown as red-green-blue). We count the number of red-green-blue sequences and refer to it as $Dm + 1$. In this example $Dm + 1 = 2$. Following m-point and $m+1$-point patterns are $w2$-$w3$ and $w2$-$w3$-

xii

LIST OF TABLES

CHAPTER 1: INTRODUCTION

Landscapes evolve as a result of the interaction between uplift and erosion. This interaction leads to the emergence of hillslopes and fluvial processes that are dynamically connected while initiating and evolving channel networks. Channel networks transport water, sediment, and nutrients. Investigating the structural, topological and geometrical properties of river networks is important to understand and quantify the components affecting the formation of distinct patterns during the landscape evolution as well as to develop predictive models describing the network dynamics under the changing environment [*Abed-Elmdoust et al.*, 2016; *Basso et al.*, 2015; *Biswal and Marani*, 2010; *Czuba and Foufoula-Georgiou*, 2015; *Dietrich et al.*, 1993; *Goren*, 2016; *Hansen and Singh*, 2018; *Howard*, 1994; *Rodriguez-Iturbe and Rinaldo*, 2001; *Rodriguez-Iturbe et al.*, 2009; *Sarker et al.*, 2019; *Shelef and Hilley*, 2014; *Tejedor et al.*, 2017a]. Due to dissimilar balance between uplift and erosion, different shapes of landscapes are observed across the world. It has been argued that climate is one of the primary sources of erosion resulting in different surficial processes e.g. sediment transport on the landscapes [*Perron*, 2017]. Thus different climatic conditions may leave distinct fingerprints on the landscape such as its forming river networks. River networks' geometrical and topological structure can be described by several indices such as drainage density [*Abrahams*, 1984; *Rinaldo et al.*, 1995a; *Tucker and Slingerland*, 1997], Horton ratios [*Horton*, 1932; 1945], branching angle [*Devauchelle et al.*,

2012; *Hooshyar et al.*, 2017], branching and side branching percentages and width function [*Leopold*, 1971; *Snell and Sivapalan*, 1994; *Veitzer and Gupta*, 2001].

The quantitative classification of channel network's structure has been extensively studied over the past decades beginning with Horton's concept of studying channels by their orders [*Horton*, 1932; 1945]. *Strahler* [1952] modified Horton's theory which resulted in defining the Horton-Strahler's ratios of bifurcation, length, and area. Horton-Strahler laws have been used for channel network classification to study their self-similar nature [*Abed-Elmdoust et al.*, 2017; *Rodriguez-Iturbe et al.*, 1994; *Tarboton*, 1996; *Tarboton et al.*, 1988] and scaling properties [*Peckham and Gupta*, 1999; *Veitzer and Gupta*, 2000]. *Hooshyar et al.* [2017] and *Seybold et al.* [2017] suggested that junction angle is also a signature of climate on the channel network and can be used as a diagnostic tool to compare the channel network's geometry and topology.

Studying the influence of the past climate on the landscape for characterizing the effects of future climate on the landscape. In this research, we investigate the response of landscape to changing climatic forcing via numerical modeling and field observations. The goal of this research is to understand and quantify the response of landscapes to the changing climatic forcing. We hypothesize that "*climate imprints distinct signature on river network geometry and topology*".

In chapter 2, we investigate the effects of climatic forcing on river network topology and geometry beyond D_d. For this, we selected 26 basins across the United States with equal D_d, however, different climate aridity index (defined here as the ratio of mean annual potential evaporation to precipitation). The river networks of these basins were extracted,

using a curvature-based method, from high-resolution (1 m) digital elevation models, and several metrics such as width functions, branching angles, and side branching ratio were computed. We used a multiscale entropy approach to quantify the geometric and topologic irregularity and structural richness of these river networks[*Ranjbar et al.*, 2018].

In chapter 3, we use a physically-based numerical landscape evolution model to investigate the channel network structure for varying hillslope and fluvial processes represented by different magnitudes of the soil transport (D) and fluvial incision (K) coefficients. We show that landscapes with the same Péclet number (defined as the ratio between the timescales of advective (fluvial) to diffusive (hillslope) processes) and thus the same characteristic length scale, may exhibit different geomorphic and topologic characteristics [*Ranjbar et al.*, 2020b].

In chapter 4, we propose a new framework based on a multi-scale entropy approach to evaluate the complexity of catchments using two different representations of channel networks. First, we investigate the structural complexity using the width function, which characterizes the spatial arrangement of channels. Second, we utilize the incremental area function along the main channel to study the functional complexity that captures the patterns of transport of fluxes [*Ranjbar et al.*, 2020a].

In chapter 5, we employ the multiscale entropy (MSE) approach to characterize the observed variability in the fluctuations of bed elevation time series (e.g. a much smaller scale in rivers) under variable discharges obtained from a field-scale laboratory flume [*Ranjbar and Singh*, 2020]. Entropy is a measure of complexity and quantifies the lack of information

in a system. We use a refined definition of entropy, MSE, which accounts for the sequence of data points and characterizes the randomness in a series.

In chapter 6, we include a summary of each chapter and the concluding remarks as well as some future research directions.

CHAPTER 2: DEPENDENCE OF RIVER NETWORK BRANCHING STRUCTURE ON CLIMATE ACROSS SCALES

River networks are important spatially distributed features that affect catchment-scale runoff response, low-flows, sediment, and solute transport and allow quantification of various catchment properties and their interaction with physical, ecological, and biological processes operating upon the network [*Basso et al.*, 2015; *Biswal and Marani*, 2010; *Collins and Bras*, 2010; *Czuba and Foufoula-Georgiou*, 2015; *Dietrich et al.*, 1993; *Goren*, 2016; *Horton*, 1932; *Howard*, 1994; *Rodriguez-Iturbe and Rinaldo*, 2001; *Rodriguez-Iturbe et al.*, 2009; *Shelef and Hilley*, 2014; *Troch et al.*, 2009; *Tucker and Slingerland*, 1997; *Wagener et al.*, 2010; *Willett et al.*, 2014]. It is crucial to investigate the structural, geometrical and topological properties of river networks to understand and quantify the components that create these distinct patterns of river networks as well as for developing predictive models for better understanding of network dynamics under changing environment [*Abed-Elmdoust et al.*, 2016; *Bertuzzo et al.*, 2008; *Peckham*, 1995; *Shelef and Hilley*, 2014; *Tejedor et al.*, 2017a; *Willett et al.*, 2014; *Willgoose et al.*, 1991].

River networks emerge as a result of interaction between factors such as climate, tectonics, erosion, and vegetation [*Abrahams and Ponczynski*, 1984; *Kirkby*, 1971;

Montgomery and Dietrich, 1992]. Their network geometry and topology can be depicted by several indices such as Horton ratios [*Horton*, 1932; 1945], drainage density [*Abrahams*, 1984; *Rinaldo et al.*, 1995a; *Tucker and Slingerland*, 1997], branching angle [*Devauchelle et al.*, 2012; *Hooshyar et al.*, 2017], and width function [*Leopold*, 1971; *Snell and Sivapalan*, 1994; *Veitzer and Gupta*, 2001]. Among these metrics, drainage density (D_d), defined as the total length of channel per unit area, is an extensively used practical measure to characterize different landscapes and quantify runoff characteristics. Several studies have identified and quantified the controlling factors of D_d at different spatial and temporal scales [*Abrahams*, 1984; *Istanbulluoglu and Bras*, 2005; *Melton*, 1957; *Rinaldo et al.*, 1995a; *Sangireddy et al.*, 2016; *Tucker and Slingerland*, 1997]. Observations from natural catchments have revealed the controls of climate on D_d. For instance, using catchments located in relatively dry regions, *Melton* [1957] observed that D_d generally increases as the climate gets dryer. On the other hand, *Madduma Bandara* [1974] used data from relatively humid areas and reported the increasing trend of D_d as the climate gets more humid. Combining the data from *Melton* [1957] and *Madduma Bandara* [1974], *Abrahams* [1984] observed a U-shape relationship between D_d and climate; therefore, it is possible to have river networks with the same drainage density but in different climates (see also *Sangireddy et al.* [2016]). In this study, we utilize the width function to capture the shape and the topology of the river networks extracted from 5-m resolution digital elevation models (DEMs). We investigate the effects of varying climate on the topologic and geometric properties of river networks using width function signals from 26 basins across the United States with approximately equal D_d but distinct long-term climatic conditions. The climatic condition of the basins is

differentiated by the climate aridity index (AI), defined as the ratio of mean annual potential evaporation (E_p) to precipitation (P) [*Budyko*, 1974]. The main focus of this study is to detect the possible signatures of climate on the topology and geometry of river networks. In order to analyze the characteristics of the width function across different spatial scales, we use multiscale entropy, which measures complexity in a series (here width function) and is able to capture the meaningful structural richness of width functions. In recent years, the concept of entropy has been used in several studies pertaining to the field of hydrology [*Liu et al.*, 2013; *Mishra et al.*, 2009; *Nourani et al.*, 2015; *Porporato et al.*, 2007; *V P Singh*, 1997]. However, to the best of our knowledge, there is limited literature about the use of entropy in the field of river networks. For example, *Leopold and Langbein* [1962] applied the entropy concept to obtain additional information about the energy distributions in a river network and their relevance with spatial and temporal changes of landforms. They used an entropy approach to explain the paths taken by the movement of water particles on the uplifted landmass. *Fiorentino et al.* [1993] used an entropy-based approach in the morphological analysis of river basin networks assuming that the only available information on a drainage basin is its mean elevation and showed that the mean basin elevation has a linear relationship with the basin entropy. More recently, *Tejedor et al.* [2017b] developed an entropy measure for quantifying the partitioning in water and sediment flux delivery to the shoreline in delta channel networks.

2.1   Width function

In general, the width function $W(x)$ represents the number of channelized pixels that have the same distance from the basin outlet where the distances are measured along the flow path i.e.,

$$W(x) = \#\{channelized\ pixels\ P: x \leq l(P) \leq x + dx\} \qquad (2.1)$$

where, $l(P)$ is the distance of pixel P from the outlet and dx represents the length of bins for counting the number of pixels with the same distance from the outlet; in this study, dx is 5 m. In other words, the width function represents the two-dimensional river network as a one-dimensional signal, capturing the branching structure of a river network. This one-dimensional signal enables us to achieve a comprehensive understanding of a river network's scaling properties [*Abed-Elmdoust et al.*, 2016; *Lashermes and Foufoula-Georgiou*, 2007; *Marani et al.*, 1994].

The width function is a powerful tool for understanding the geomorphic structure of river network and its control on the basin's hydrologic response [*Gupta and Mesa*, 1988; *Snell and Sivapalan*, 1994; *Troutman and Karlinger*, 1985], and has been used to investigate catchments' characteristics for assessing channel network properties at different spatial scales [*Black et al.*, 2012; *Lashermes and Foufoula-Georgiou*, 2007]. The concept of the width function was first introduced by *Kirkby* [1976] and several studies have investigated the properties of river networks using this concept. For example, *Rodríguez-Iturbe and Valdes* [1979] argued that assuming constant flow velocity within a basin, the width function can represent the geomorphological unit hydrograph (GUH) and the distribution of travel times (see also, *Gupta and Mesa* [1988]). Therefore, the width function provides a reasonable

alternative approach for deriving the hydrological responses in ungauged basins [*Moussa*, 2008; *Rodriguez-Iturbe and Rinaldo*, 2001]. *Marani et al.* [1994] used width functions to examine the fractal structure of real basins and argued that the spatial patterns of aggregation share some common properties with random cascades. Random cascades are models used to analyze systems that contain fluctuations over several ranges of scales. More recently, *Lashermes and Foufoula-Georgiou* [2007] investigated the multifractal properties of width functions of real networks and studied the common properties of them with the stochastic self-similar trees. Furthermore, *Moussa* [2008] studied the morphometric properties controlling the shape of width function.

2.2   Entropy

In general, entropy quantifies the amount of information in a signal based on the probability of each value of the signal [*Shannon*, 1948]. In other words, entropy measures uncertainty in the occurrence of events over a space or time domain. Mathematically, the Shannon entropy of a signal represented by a vector $X = [x_1, x_2, ..., x_N]$ can be expressed as:

$$H(X) = -\sum_{i=1}^{N} p(x_i) \log p(x_i) \qquad (2.2)$$

where $p(x_i)$ is the probability of x_i and N is the sample size.

The entropy measure defined in Eq. (2.2) is not sensitive to the sequence of the values. However, in geomorphic or environmental signals, such as the width function of a river network, the sequence of data points directly represents the structural pattern of the topology of the river network. For example, Figure 1 shows two hypothetical basins with

approximately equal drainage area and cumulative drainage length (therefore, equal drainage density). The width function series of basins 1 and 2 as shown in Figure 1 can be expressed as $W_1 = \{1, 1, 2, 2, 4, 5, 4, 5, 5, 6, 5, 6, 7\}$ and $W_2 = \{1, 1, 2, 5, 6, 4, 7, 5, 2, 6, 5, 4, 5\}$, respectively (see Figure 1c for a graphical representation). From these width functions, one can compute the Shannon entropy using Eq. (2.2 by calculating the probability of each value of the width function.

Although these two networks have a distinct structural arrangement of channels and junctions, as is visually evident in Figure 1a and b, the entropy (Shannon) computed using Eq. (2.2) results in the same value (i.e. $H(W_1) = H(W_2) = 0.74$) for both cases. This example clearly demonstrates that the Shannon entropy measure cannot capture the difference in the structural organization of channels in a river network and thus the physical processes that create these complex patterns since the width functions of these basins contain the same numerical values but different ordering sequences.

To capture the structural arrangement of channels embedded in the width function and overcome the limitation of Shannon Entropy, we use multiscale entropy [*Costa et al.*, 2002; 2005] as a measure of complexity [*Abedin et al.*, 2017] that can capture the structural richness of river networks.
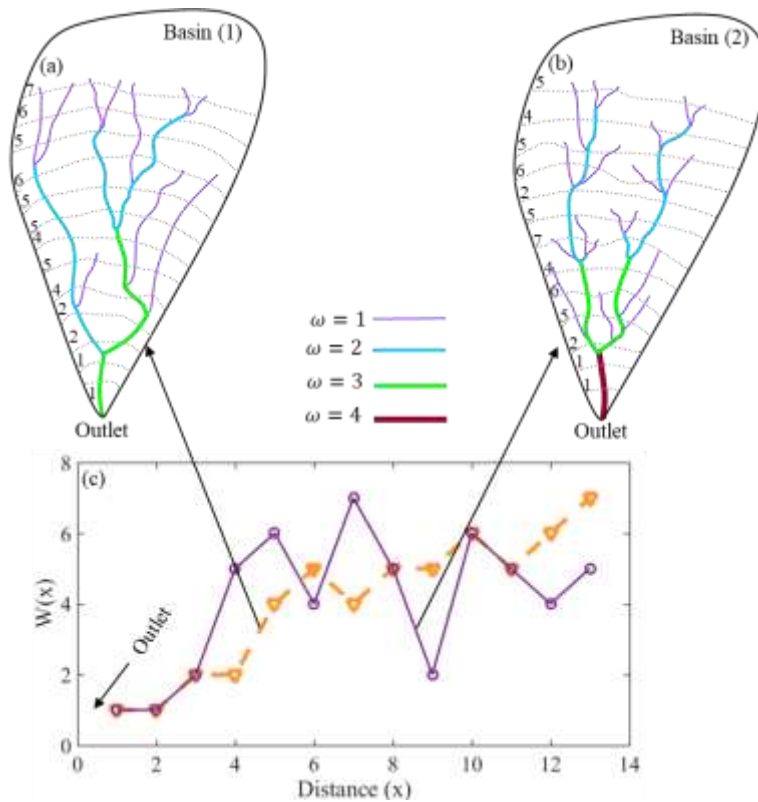
Figure 1. Schematic representation of hypothetical basins with the same drainage density (assigning an equal drainage area and an equal total drainage length for basin 1 (a) and basin 2 (b)) but distinct width function. Numbers on the left side of each basin show the number of channel pixels that have the same distance from the outlet in each basin. Width functions of basin 1 (solid line) and basin 2 (dashed line) are plotted in subplot (c). Stream orders (ω) are represented by different colors. Basin 1 contains channels up to order 3 whereas basin 2 contains 4th order channels.

2.3   Multiscale Entropy

Sample entropy, S_E, first proposed by *Richman and Moorman* [2000], is an alternative measure of entropy which considers the sequence in a series while computing its uncertainty and complexity. S_E represents the probability that two similar patterns containing *m*

sequential points in the signal remain similar if another point is added to the patterns (i.e. by increasing pattern length to $m + 1$). Here, the patterns with m sequential points are defined as vectors of size m that are moving through the length of the signal. The similarity in patterns is delineated by a tolerance denoted as r, which determines whether two vectors can be considered equal or close to each other. Particularly, the maximum difference across the components of the two vectors is defined as the distance d between two sequences. When d satisfies the condition $d \leq r$, the two vectors are considered as "close to each other within the tolerance r". S_E can be computed as:

$$S_E(m, r, N) = -\ln \frac{n_{m+1}(N, r)}{n_m(N, r)} \qquad (2.3)$$

where m is the number of data points in a pattern (also referred to as vector); r is the similarity criterion or tolerance; N is the length of the main series; and $n_m(N, r)$ and $n_{m+1}(N, r)$ are the total numbers of repetitions of vectors of length m and m+1 (m-point and m+1-point patterns), respectively. The total number of repetitions is defined as the number of times a pattern (vector of length m or m+1) has been repeated along the series with a tolerance r. For a series W of length N, the steps for calculating S_E are provided below:

1. Define m-point vectors W_m^i, W_m^j as:

$$W_m^i = \{W^i, W^{i+1}, \dots, W^{i+m-1}\}, \quad 1 \leq i \leq N - m$$

$$W_m^j = \{W^j, W^{j+1}, \dots, W^{j+m-1}\}, \quad 1 \leq j \leq N - m$$

where $i \neq j$.

2. Compare pairs of m-point vectors (W_m^i, W_m^j) to determine whether they have a distance d smaller than the specified tolerance r. To compute the number of

repetitions (D_m) for each m-length template vector, S_E uses a Heaviside function as:

$$D_m^{i,j}(r) = \begin{cases} 1 & d_m^{i,j} \le r \\ 0 & d_m^{i,j} > r. \end{cases} \tag{2.4}$$

For example, for m=2, $W_2^1 = \{W^1, W^2\}$ and $W_2^2 = \{W^2, W^3\}$. Distance d is computed as $d_2^{1,2} = max\{|W^1 - W^2|, |W^2 - W^3|\}$. If $d_2^{1,2} < r$, then $D_2^{1,2}(r) = 1$ and W_2^2 is refered to as a forward match (matched pair) for the pattern $W_2^1 = \{W^1, W^2\}$. $D_m^{i,j}(r)$ is computed for every pair of i and j ($1 \le i \le N - m$ and $1 \le j \le N - m$). Note that for a series with N data points only N-m vectors with length m are considered as the patterns, although N-m+1 patterns with length m exist in the series. This is in order to ensure that for a vector i with length m, where $1 \le i \le N - m$, the corresponding m+1 length vector also exists.

Costa et al. [2002] suggested a value of r as 15% of the standard deviation of the main series. Using r as a percentage of the standard deviation makes the value of S_E independent of the absolute values and variance of the main series. However, the sequential ordering of values creating the original series is the essential factor affecting S_E. In case of a large value of r, the vectors will be less distinguishable from each other and the signal appears to be more regular than it is. In other words, increasing r will decrease the accuracy of the analysis.

3. Sum the numbers of similar vectors (matched pairs) for every (W_m^i, W_m^j) to obtain the total number of repetition, i.e. $n_m(N, r)$, for the m-point pattern.

$$n_m(N, r) = \sum D_m^{i,j}(r) \tag{2.5}$$

4. Repeat steps 1 to 3 for vectors with length $m{+}1$. The total number of repetition

   for the $m+1$ -point pattern thus can be expressed as:

$$n_{m+1}(N,r) = \sum D_{m+1}^{i,j}(r)$$

(2.6)

5. Compute sample entropy using Eq. (2.3).

A smaller ratio of $\frac{n_m}{n_{m+1}}$ indicates i) more regularized features of a series, i.e. the

locations where the m-point pattern is present, the $m{+}1$-point pattern is likely to be present;

and ii) the signal is more self-similar. This approach requires an initial normalization to

ensure S_E is dependent on the distinct organizational structure but not on the variances of

the two series. Therefore, signals were centered by subtraction of the mean and normalized

to standard deviation [*Richman and Moorman*, 2000]. Figure 2 briefly illustrates the

computation of sample entropy using a simple example.

Figure 2. A sample width function series $W(x)$ used to demonstrate the steps involved in the sample entropy calculations. In this example $m = 2$ [*Costa et al.*, 2002; 2005]. The first m-point pattern (sequence) is represented by w_1-w_2 (red-green) and $m+1$-point pattern by w_1-w_2-w_3 (red-green-blue). The dashed lines around the data points represent $w_1 \pm r$ (red), $w_2 \pm r$ (green), and $w_3 \pm r$ (blue), and indicate the tolerance for counting similar patterns. For the pattern with length $m = 2$ where the first point is w_1 (red) and the second point is w_2 (green), we count all the w_1-w_2 sequences, i.e. we count the number of times that a green data point appears right after a red data point. The number of the pairs that match the first 2-point pattern is referred to as D_m and in this example $D_m = 6$. Next, we add another point to the previously considered m-point pattern. This 3-point pattern ($m+1$ or longer pattern) can be represented by the sequence of w_1-w_2-w_3 (shown as red-green-blue). We count the number of red-green-blue sequences and refer to it as D_{m+1}. In this example $D_{m+1} = 2$. Following m-point and $m+1$-point patterns are w_2-w_3 and w_2-w_3-w_4, respectively. After computing D_m and D_{m+1} for every m-point and $m+1$-point patterns, the total number of repetition can obtained using Eqs. (2.5) and (2.6).

The S_E approach only quantifies pattern irregularity at one scale; however, natural systems such as river network width functions exhibit variability across a range of scales. Moreover, the S_E approach assigns higher entropy values to surrogate signals (with increments Gaussian distributed) of the main series than the main series, although main series (also referred here to as original signal/series) may contain structural nonlinearity than in a surrogate signal where the nonlinearities are destroyed by randomizing the signal [*Costa et al.*, 2005; *A Singh et al.*, 2009a]. Note that the surrogate series maintain the probability density function (pdf) and the linear correlation structure of the original series. *Costa et al.* [2002; 2005] also used sample entropy to evaluate white noise [*Hosking*, 1981; *Mandelbrot and Van Ness*, 1968] versus 1/f noise (pink noise [*Costa et al.*, 2002; 2005]) and observed that sample entropy assigned a higher value to white noise compared to 1/f noise. However, 1/f noise encompasses more complex structure due to its long-range correlation.

In order to resolve this limitation, *Costa et al.* [2002] proposed to evaluate sample entropy at multiple scales considering the interrelationship between scales and entropy. The multiscale entropy (*MSE*) computation includes two steps: i) generating the consecutive coarse-grained signals corresponding to each scale, and ii) computing the sample entropy for each coarse-grained series that is generated in the previous step. Thereafter, a series of entropy values is generated which reveals the amount of complexity in a signal at multiple scales. Note that, r is not recalculated throughout each scale and remains the same for all scales.

For coarse-graining the original series, the series is divided into non-overlapping windows of length equal to scale s, and the data points within each window are averaged. Generally, each data point of the coarse-grained series at each scale s is computed as:

$$\omega_j^s = \frac{1}{s} \sum_{i=(j-1)s+1}^{js} W^i, \quad 1 \le j \le \frac{N}{s} \tag{2.7}$$

where $\omega^s = \left\{\omega_1, \omega_2, \ldots, \omega_j, \ldots, \omega_{\frac{N}{s}}\right\}$ is the coarse-grained series at scale s. For example, $\omega^1 = \left\{\omega_1 = W^1, \omega_2 = W^2, \ldots, \omega_{\frac{N}{1}} = W^N\right\}$ is the coarse-grained series at scale 1, $\omega^2 = \left\{\omega_1 = \frac{W^1+W^2}{2}, \omega_2 = \frac{W^3+W^4}{2}, \ldots, \omega_{\frac{N}{2}} = \frac{W^{N-1}+W^N}{2}\right\}$ is the coarse-grained series at scale 2, and $\omega^3 = \left\{\omega_1 = \frac{W^1+W^2+W^3}{3}, \omega_2 = \frac{W^4+W^5+W^6}{3}, \ldots, \omega_{\frac{N}{3}} = \frac{W^{N-2}+W^{N-1}+W^N}{3}\right\}$ is the coarse-grained series on scale 3.

Although only $m = 2$ and $m + 1 = 3$ patterns are considered in our analysis, considering patterns corresponding to these m values at higher scales, indirectly allows examination of larger m patterns. For example, at the 2nd aggregation scale, the original width functions are averaged in non-overlapping windows of length 2 data points. Correspondingly, $m = 2$ in 2nd aggregation scale includes 4 data points of the original width function; whereas, $m+1 = 3$ at the same scale includes 6 points. The reason for not using higher values of m is the fact that within a series it is highly improbable to find a pattern of length 4, 5, or larger exactly being repeated throughout the series. In this case, there may not be any forward matches for the longer length patterns which will result in $n_m(N,r) = 0$ and/or $n_{m+1}(N,r) = 0$. Thereafter, the ratio of $\frac{n_{m+1}(N,r)}{n_m(N,r)}$ will be undefined. Thus, the choice

of coarse-grained series with a higher length of non-overlapping windows, instead of using higher values of m, partly prohibits from obtaining undefined entropy.

Essentially, using the *MSE* approach one can demonstrate that the correlated random signals such as 1/f noise exhibit more complexity than white noise, which is an uncorrelated random noise. For example, as shown in Figure 3, for the first few scales the amount of entropy for white noise is higher than that for 1/f noise. However, with an increase in scale the entropy for white noise decreases monotonically; whereas, for the 1/f noise, it remains constant at almost all scales > 4. This distinct behavior can be explained by considering the complex structures (correlations) over multiple scales. For example, in white noise as the length of the coarse-graining window increases, the average value within each window converges to a fixed value such that no new information is revealed at the higher scales. Whereas, in the case of 1/f noise with increasing scale, the statistical properties of the values inside the window do not converge to a constant value since new information is aggregated in each scale (see for more details [*Costa et al.*, 2002]). Figure 3 also shows examples for increment series of fractional Brownian motion (fBm) with Hurst exponent $H = 0.6$ and $H = 0.8$. As the signal with $H = 0.8$ contains more correlation structure than $H = 0.6$ [*A Singh et al.*, 2009a], the *MSE* approach is able to identify this complexity by assigning higher entropy values to $H = 0.8$ as compared to $H = 0.6$. Thus *MSE* enables us to quantify the difference between random noise and structural complexity of a signal across a range of scales.
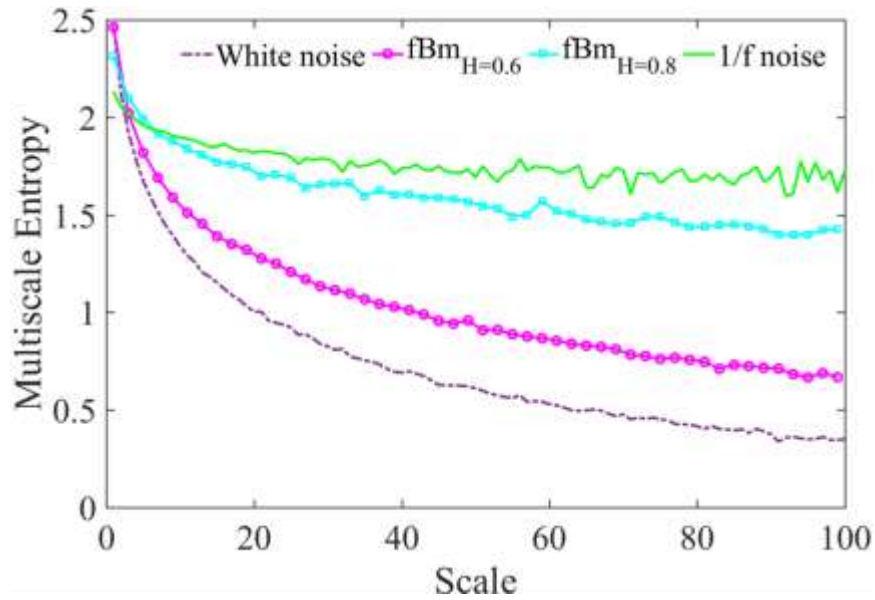
Figure 3. Multiscale entropy (*MSE*) computed for theoretical signals, i.e. 1/f noise, white noise, and fractional Brownian motion (fBm) with Hurst components of 0.6 and 0.8. Each *MSE* curve was computed and averaged for 15 signals each individually containing 10,000 data points using MATLAB 2016. For all cases, *m* and *r* were 2 and 0.15, respectively.

2.4   Fuzzy Multiscale Entropy

In the *MSE* calculation, S_E is not defined if no forward matches occur, i.e. if no pairs of template vectors satisfy $d_m \leq r$ or $d_{m+1} \leq r$. This may occur when the length of a signal (e.g. width function here) and/or the similarity criterion (*r*) is small [*Chen et al.*, 2007; *Richman and Moorman*, 2000]. Therefore, the robust computation of the *MSE*, as discussed above, requires long signals of data. However, physical data such as the width functions may have limited length due to the size of the basin and/or the resolution of DEMs. *Chen et al.* [2007] developed fuzzy entropy approach in order to prevent obtaining undefined entropy

values by employing an exponential function (Eqs. (2.6) and (2.7)) as the fuzzy measurement [*Abedin et al.*, 2020; *Zadeh*, 1965] of the two template vectors' similarity ($\mathcal{D}_m$, $\mathcal{D}_{m+1}$) instead of the Heaviside function used in S_E calculation (see also, *Azami et al.* [2017]). The closer the $\mathcal{D}_m$ and $\mathcal{D}_{m+1}$ values are to 1, the more similar are the template vectors. $\mathcal{D}_m$ and $\mathcal{D}_{m+1}$ can be expressed as:

$$\mathcal{D}_m(z,r) = \exp\left(-\frac{(d_m)^z}{r}\right) \tag{2.8}$$

$$\mathcal{D}_{m+1}(z,r) = \exp\left(-\frac{(d_{m+1})^z}{r}\right) \tag{2.9}$$

where, z determines the gradient of the boundary of the exponential function. *Chen et al.* [2007] suggested using $z=2$. The total fuzzy numbers of repetition for m-point and $m+1$-point patterns are computed using the fuzzy number of repetition, $\mathcal{D}_m$ and $\mathcal{D}_{m+1}$ and can be defined as:

$$\eta_m(N,r,z) = \sum \mathcal{D}_m^{i,j}(r) \tag{2.10}$$

$$\eta_{m+1}(N,r,z) = \sum \mathcal{D}_{m+1}^{i,j}(r) \tag{2.11}$$

The fuzzy sample entropy at each scale (hereafter called *MSE*) is computed using η_m and η_{m+1}, characterizing the total fuzzy number of repetition for m-point and $m+1$-point patterns as:

$$E(m,r,N,z) = -\ln\frac{\eta_{m+1}(N,r,z)}{\eta_m(N,r,z)} \tag{2.12}$$

To accommodate shorter lengths of signals, we incorporate fuzzy entropy approach Eq. (2.12), in the *MSE* calculations that abstain undefined entropy by employing an

exponential function for counting similar patterns (see, *Chen et al.* [2007] and *Azami et al.* [2017]). Note that Fuzzy *MSE* demonstrates the same results (Figure 3) analyzing the white and 1/f noises as *MSE* discussed in section 2.3 [*Azami et al.*, 2017].

2.5   Data and site description

In this study, we investigate the structure of the width function for basins under different climatic conditions. In order to understand the distinct geometric and topologic signature of climate on river basins, we selected 26 basins with equal drainage density located in 9 states across the United States, 13 basins in dry, and 13 basins in humid climate, based on the availability of LiDAR data [*Hooshyar et al.*, 2016; *Lashermes et al.*, 2007; *Passalacqua et al.*, 2010; *Rajabi*, 2018; *Rajabi et al.*, 2018]. The LiDAR data was obtained from https://lta.cr.usgs.gov/lidar_digitalelevation. Figure 4 shows the locations of basins used in this study. Note that the drainage density D_{d_i} is defined as total drainage length over the total basin area, i.e. $D_{d_i} = \frac{L_{T_i}}{A_i}$ (here constant), where L_{T_i} is the total length of channels for basin i with a total drainage area A_i. The average drainage density used in this study was 10.5 km^{-1}, with the standard deviation of 1.4 km^{-1} and the long-term climate was quantified based on the AI. Here, basins with $3.10 \leq \frac{E_p}{P} \leq 10.64$ are referred to as dry basins; whereas basins with $0.25 \leq \frac{E_p}{P} \leq 1.36$ are considered humid basins. These ranges are determined based on previous studies [*Arora*, 2002; *Budyko*, 1974; *Ponce et al.,* 2000]. For example, based on *Budyko* [1974], regions where the aridity index is higher than 1 are generally classified as dry since the evaporation demand cannot be compensated by precipitation (water-limited). Whereas, regions with aridity index less than 1 are classified

as humid regions (energy-limited). The aridity index has also been related to broader range climatic regimes; i.e., arid, semi-arid, sub-humid, and humid which are categorized as $12 > AI \geq 5, \; 5 > AI \geq 2, \; 2 > AI \geq 0.75$, and $0.75 > AI \geq 0.375$, respectively [*Arora*, 2002; *Ponce et al.,* 2000]. In this study, arid and semi-arid regions are referred to as dry regions and sub-humid and humid areas are considered as humid regions.

Table 1, shows the properties of the studied basins such as climate aridity index, total channel length, drainage area, drainage density, concavity index and relative relief. The drainage networks of the selected basins were extracted using a curvature-based method developed by *Hooshyar et al.* [2016] using high-resolution topographic data. The width function of each basin was computed based on the extracted river networks using bins of 5-m distance and the length of the width function depended on the longest flow length in the basin. Figure 5 shows two river basins with superimposed river networks in dry (red) and humid (blue) climatic conditions and associated width functions. The two selected basins, shown for visualization purposes, have approximately the same longest flow length (i.e. ~ 600 m). Relative relief was computed as the ratio of the maximum elevation of the basin to the length to the outlet in each basin. Concavity index was computed as the slope of a linear line regressed through the log-log plot of channel slope (percent rise) versus drainage area (m^2).
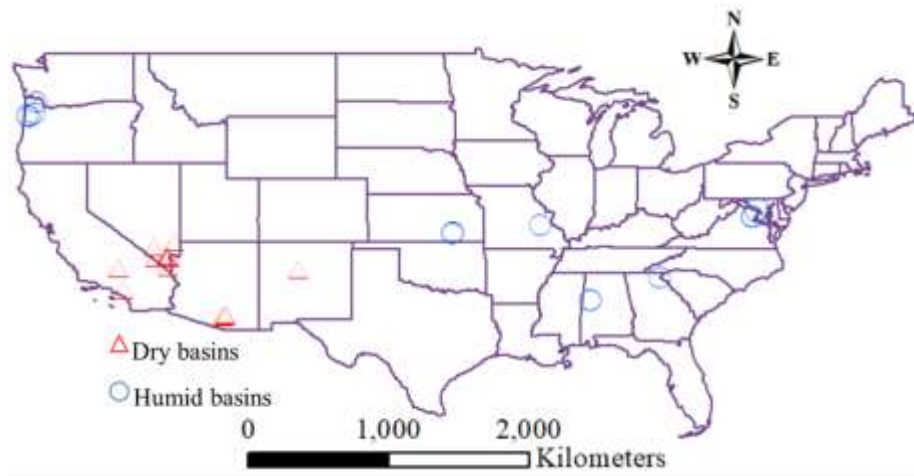
Figure 4. The locations of the dry and humid basins across the United States.
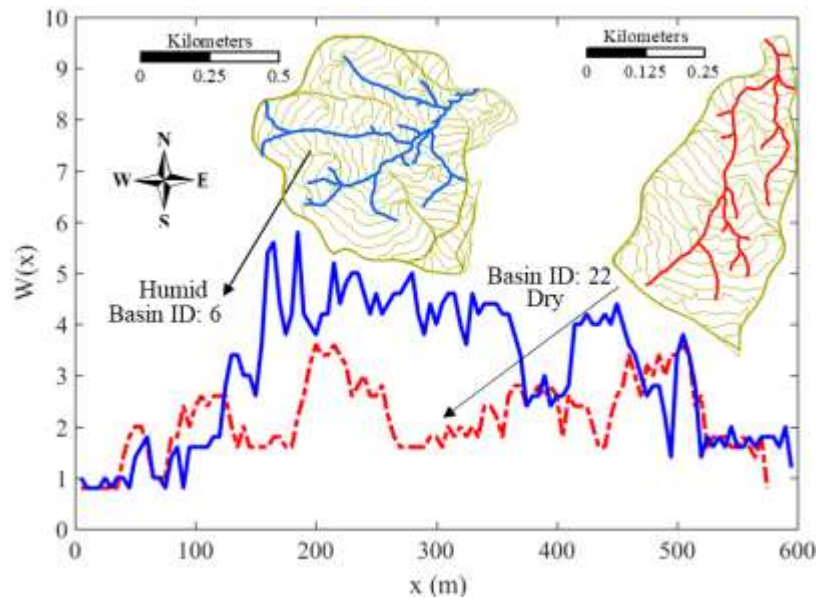
Figure 5. The width functions and river networks of two basins located in humid (blue) and dry (red-dashed) regions. The two basins were selected based on similar longest channel length for illustration purposes. Notice, it is difficult to distinguish, visually, climate conditions from the corresponding width functions.

Table 1. Climate aridity index, total channel length, drainage area, drainage density, concavity index, and relative relief of the basins used in this study.

Climate	Basin ID	Climate Aridity Index (Ep/P)	Total Channel Length (km)	Drainage Area (km^2)	D_d (km/km^2)	Concavity Index	Relative Relief
Humid	1	0.25	14.39	1.38	10.44	-0.11	0.67
	2	0.30	10.57	1.16	9.09	-0.14	0.24
	3	0.39	9.35	1.03	9.06	-0.11	0.42
	4	0.46	4.18	0.52	8.07	-0.14	0.30
	5	0.73	22.43	2.28	9.84	-0.29	0.27
	6	0.96	1.81	0.18	9.84	-0.18	0.23
	7	0.96	24.77	2.00	12.41	-0.26	0.06
	8	1.11	24.84	2.34	10.60	-0.16	0.05
	9	1.12	29.65	2.56	11.58	-0.18	0.06
	10	1.13	24.80	2.19	11.35	-0.21	0.04
	11	1.17	26.09	2.27	11.49	-0.28	0.13
	12	1.34	20.97	2.11	9.95	-0.20	0.13
	13	1.36	23.46	2.33	10.07	-0.17	0.13
Dry	14	3.10	5.06	0.54	9.33	-0.28	2.02
	15	3.72	3.29	0.37	8.97	-0.22	2.34
	16	4.73	7.93	0.77	10.34	-0.25	0.66
	17	5.15	3.12	0.39	7.99	-0.29	0.83
	18	5.27	5.01	0.60	8.29	-0.29	0.59
	19	8.42	2.56	0.21	12.45	-0.26	0.95
	20	8.53	2.79	0.23	12.04	-0.25	1.15
	21	8.92	3.12	0.27	11.56	-0.13	2.01
	22	9.16	1.25	0.10	12.49	-0.25	1.72
	23	9.32	1.49	0.14	10.48	-0.23	1.42
	24	9.73	2.70	0.25	10.87	-0.18	1.04
	25	10.19	0.93	0.07	12.43	-0.10	1.83
	26	10.64	11.77	0.96	12.23	-0.16	0.47

2.6 Results and discussion

The *MSE* approach discussed in section 2.4 was used to compute the scale-dependent entropy of the width functions of 26 basins under different climatic conditions. Figure 6a shows the average entropy curves for 13 dry (red curve) and 13 (blue curve) humid basins. The *MSE* was computed with parameter settings of $m = 2$, $r = 0.15 \times \sigma$ (σ is the standard deviation of the signal) and $z = 2$ as suggested by *Costa et al.* [2002; 2005] and *Chen et al.*

24

[2007]. Figure 6b shows the total number of repetition (η_{m+1} and η_m) curves for 13 dry (red curve) and 13 (blue curve) humid basins.

From Figure 6a, the following observations can be made: 1) the average scale-dependent entropy of width functions increases with scale for both dry and humid basins; 2) the entropy across all scales is higher for dry basins as compared to humid basins; and 3) the rate of increase in entropy is much larger for dry basins as compared to humid basins. The increase in entropy with scale is since the number of longer sequences ($m+1=3$) reduces, for both dry and humid basins, at a rate comparatively larger than the number of shorter sequences ($m=2$). However, both smaller (m-point) and larger ($m+1$-point) patterns coexist with much similar frequencies across scales in humid basins indicating a more homogeneous (regularized) channel branching structure (Figure 6b). Note that a constant MSE curve represents a perfectly regularized branching structure, i.e. both m and $m+1$ patterns are repeated with the same frequency across all scales.

The higher entropy observed in dry basins across all scales suggests that dry basins, in general, contain more complex (less regular) organizational structure of channels in river networks over multiple scales. In particular, as discussed above, a larger entropy value, i.e. larger $\frac{\eta_m}{\eta_{m+1}}$, indicates that the total number of repetitions for the shorter patterns (m-point) is considerably larger than the longer pattern ($m+1$-point), i.e. $\eta_m > \eta_{m+1}$, suggesting a less regularized channel branching pattern. This can be seen from Figure 6b where the difference between the two patterns' repetition represented by η_m and η_{m+1} curves is slightly larger in dry basins as compared to humid basins. In addition, the slope, depicting the rate of decrease of average η_m and η_{m+1} as a function of scales, denoted by λ_D and λ_H for dry and

humid basins, respectively, is larger in dry basins than humid basins, again suggesting higher structural irregularity in dry basins than humid basins.

The difference between *MSE* curves (Figure 6a) of dry and humid basins increases more rapidly at larger scales specifically at scales greater than ~ 65 m which corresponds to the median length of second order channels in all the study basins (66 m, see Table 2). This increase in *MSE* at larger scales in dry basins suggests a higher degree of heterogeneity at larger scales compared to smaller scales. Along with this, in addition, the higher overall entropy in dry basins indicates that the observed structural heterogeneity across scales may be manifested in junction angles and channel lengths. Junctions' angles are formed by two intersecting channels and are detected as the pixels with more than one immediate upstream pixels (see, *Hooshyar et al.* [2017]). The channel length here is referred to as the link length. To further investigate the causes of organizational irregularity (i.e. heterogeneity) in dry basins as compared to humid basins, we explore the geometry and topology of the river networks expressed in channel lengths and junction angles. We remind the reader again that the basins considered in this study correspond to similar drainage density which can be seen from the plot of the total length versus their total drainage area for both dry and humid basins (Figure 7a). The data points in Figure 7a follow a linear trend with slope ≈ 1, which indicates almost equal drainage density (10.5 km^{-1}) for all the basins.
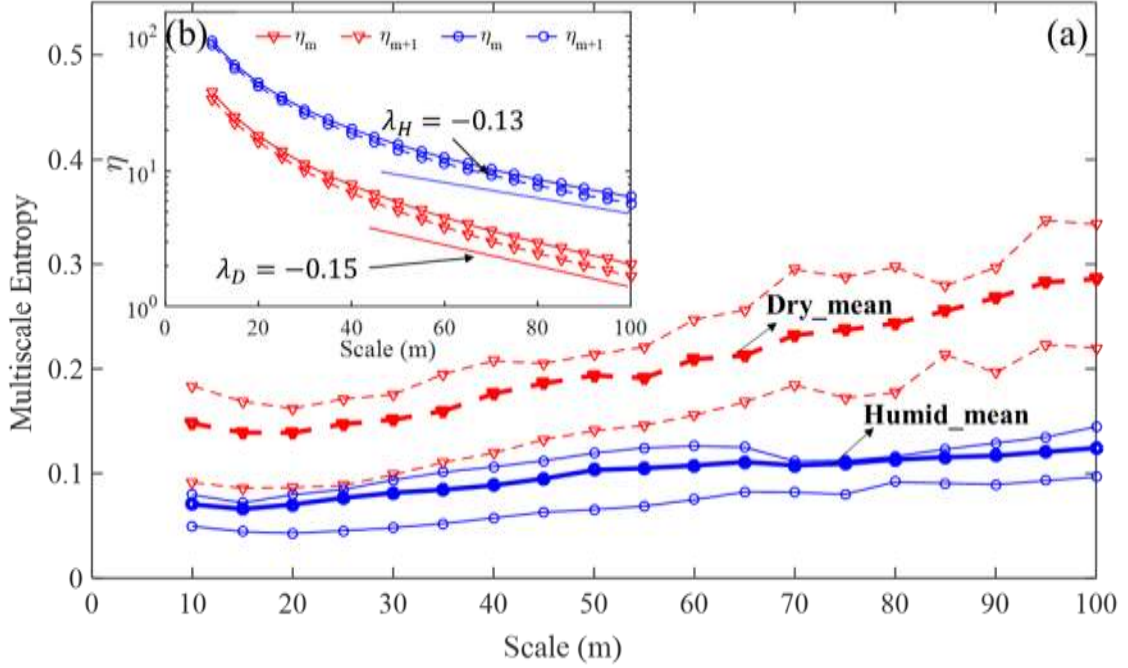
Figure 6. a) Average *MSE* curves for 13 dry (dashed red) and 13 humid (blue) basins. Thin dashed red and blue curves show the 25th and 75th percentile curves for dry and humid basins respectively. *m*, *r* and *z* are set to 2, 0.15, and 2, respectively, based on *Costa et al*. [2002; 2005] and *Chen et al.* [2007]. The *x*-axis shows the scales representing the length of non-overlapping windows for coarse-graining the original width function [*Hooshmand et al.*, 2018]. b) The average total fuzzy number of repetitions (frequency) for patterns with *m* data points, η_m (dashed) and with *m*+1 data points, η_{m+1} for both dry (red) and humid basins (blue). λ_D and λ_H represent the rate of decrease of average η_m and η_{m+1} as a function of scales, for dry and humid basins, respectively.

Figure 7b shows the pdfs of junction angles for dry and humid basins indicating that dry basins have larger junction angles compared to humid basins (see, *Hooshyar et al.* [2017] for details about junction angle computation). These pdfs showed significant difference which was tested using Kolmogorov-Smirnov test at 95% confidence interval (P-values = 0.03). This characteristic of dry basins, i.e., exhibiting larger junction angles, makes them

restricted to containing only the smaller patterns (*m*-point sequences) and not the larger patterns (*m*+1-point sequences) in width function. In other words, dry basins, due to larger junction angles, have higher complexity since the shorter and longer patterns are not being repeated with a similar frequency at each scale. Figure 7b (inset) further illustrates schematically how the junction angle can affect the repetition of patterns in dry and humid basins. Considering two small tributaries (1st order links) in dry and humid basins, for equal distance lines (grey lines in Figure 7b), both *m* and *m+*1 patterns exist in the humid basin with similar frequencies (i.e. $\eta_m \sim \eta_{m+1}$). However, in the dry basin, the junction angle is larger such that the channel does not intersect the last distance line. Note that channel length is equal for both dry and humid basins in this example. The larger junction angle may cause an increase in the area or the width of the basin, which was independently verified using aspect ratio (basin-width/basin-length) that showed higher average aspect ratio for dry basins as compared to humid basins (Table 2).

Based on the above discussion, branching pattern of river networks, especially the structural organization of channels is related to the link (channel segments) length and channel junction angle, and is manifested in the width function. This indicates that the channel length and the bifurcation angle that these channels are intersecting at can affect the shape of the width function. However, the width function does not distinguish between channels of different orders. To explore the relationship between the channel characteristics of different orders and their junctions, we decompose the channel networks as a function of orders (ω) and compare the geometric properties such as length-area relationship in different orders across varying climates.

Table 2. Statistical characteristics of river network topology and geometry. *L, A* and α represent the median length, area, and junction angle. J_d represents the average junction density defined as the number of junctions normalized by the total channel length. Branching percentage represents channels that follow Horton-Strahler ordering [*Horton*, 1945], whereas side branching indicates the percentage of channels of order ω intersecting channels with order $\omega' > \omega$. To compare dry and humid basins for all the parameters, the larger values are indicated with bold numbers. Numbers in subscripts and superscripts represent 25th and 75th percentiles, respectively.

`		L (m)	A (m^2)	α	Aspect ratio	J_d	Branching (%)	Side-branching (%)
ω_1	Dry	$\mathbf{50^{84}_{31}}$	$\mathbf{3304^{6453}_{1690}}$	$\mathbf{64^{75}_{51}}$	**1.16**	7.5	**28**	72
	Humid	27^{56}_{14}	1326^{4026}_{339}	60^{74}_{48}	1.15	9.6	25	**75**
ω_2	Dry	66^{148}_{32}	$\mathbf{15675^{30507}_{7913}}$	$\mathbf{72^{79}_{55}}$	**0.67**	1.6	**33**	67
	Humid	66^{145}_{27}	10088^{27856}_{4317}	65^{79}_{53}	0.55	1.9	30	**70**
ω_3	Dry	$\mathbf{308^{595}_{140}}$	$\mathbf{116082^{224200}_{62337}}$	$\mathbf{77^{85}_{69}}$	**0.41**	0.15	**38**	62
	Humid	177^{396}_{68}	62919^{159137}_{21596}	65^{82}_{50}	0.39	0.53	33	**67**
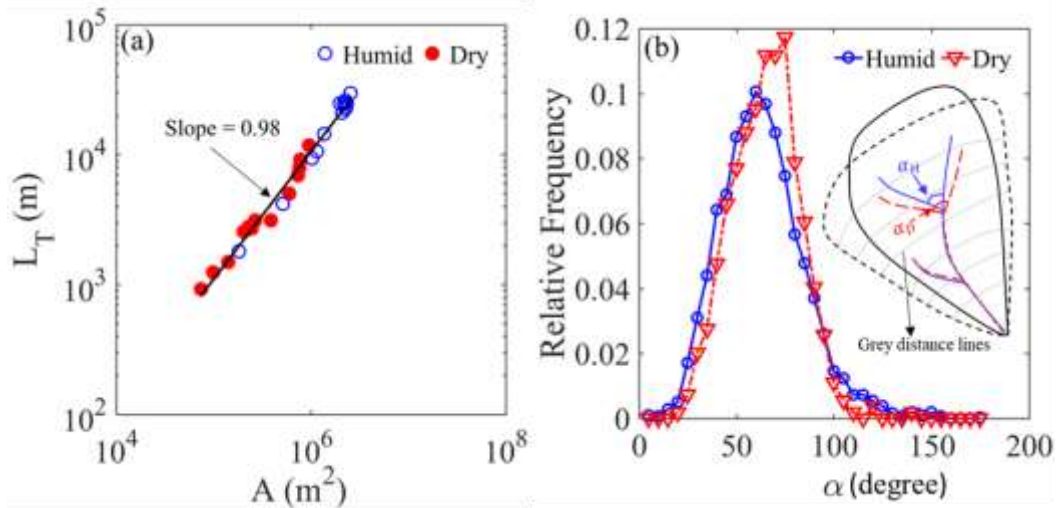
Figure 7. a) Total channel length versus drainage area for the 26 study basins. Humid and dry basins are shown with blue and red (solid) circles, respectively. b) The pdfs of junction angles for humid (blue circle) and dry basins (red triangle). Inset in (b) shows hypothetical dry and humid sub-basins. It is assumed that channel length is same but junction angles are different. The red-dashed line represents channels in the dry basin and the blue line represents channels in the humid basin. The grey lines inside the hypothetical basins represent the pixels that have the same distance from the outlet. Kolmogorov-Smirnov test was used to determine if the two distributions are significantly different. Results show that within the 95% confidence interval the dry basins have larger angles than humid basins (P-value=0.03).

Figure 8a, b and c show the length of 1st, 2nd and 3rd order channels (referred to as channel links, interchangeably) versus the corresponding drainage area [*Rigon et al.*, 1996]. Note that these data have been binned along the horizontal axis with the bin size of 0.3 m^2 for demonstration purposes. Although some basins contain channels with order higher than 3, to be consistent, we only show results up to 3rd order. In addition, the effect of climate is

more likely associated with smaller channel orders as compared to larger orders [*Mutlu et al.*, 2019; *Zanardo et al.*, 2013].

Figure 8a, b and c show the power-law exponent fitted to the length-area plots which is akin to Hack's exponent [*Biswal and Marani*, 2010; *Rigon et al.*, 1998; *Rigon et al.*, 1996]. Fo all three orders, this exponent is relatively higher for dry basins compared to humid basins. For example, average slope, i.e. the average of slopes of all three orders shown in Figure 8a, b and c, for dry basins is $\beta_D=0.73$ as compared to the average slope of humid basins, which is $\beta_H=0.60$. In addition, Figure 8d, e, and f show a larger average junction angle for dry sub-basins as compared to humid sub-basins for all channel orders indicating that dry sub-basins are in general wider than humid sub-basins under the constraint of equivalent drainage density, as observed above for the basins. Note that, although the drainage density was equal for the dry and the humid basins in this study, the dry basins exhibited a higher relative relief and higher concavity index compared with the humid basins (Table 1). Also note that the T-test was performed to quantify whether the two distributions shown in Figure 8d, Figure 8e, and Figure 8f were significantly different. For all cases, the P-values were found to be < 0.05 at 95 % confidence interval (Table 3), suggesting the pdfs are indeed significantly different.

The slope difference in the length-area relationship of humid and dry basins further indicates a lack of similarity in the topologic and geometric structure of the channel networks in distinct climatic conditions. River basins might be distinguishable based on the fundamental difference in their behavior in terms of forming river networks with specific junction angles, drainage lengths, and drainage areas. The maximum slope difference in

length-area curves (Figure 8) between humid and dry basins is observed for the 2nd order

channels where the median length of channels is 66 m in both humid and dry basins. For this

order (ω =2), the slope of the length-area curve for dry basins is ~ 0.85 whereas for humid

basins this slope is 0.66. This observation of larger slope difference is consistent with the

scale ~ 65 m at which a transition is observed in *MSE* curve of the dry basin, suggesting the

essential difference in the topologic organization between dry and humid basins is more

persistent at scales larger than this scale (~65 m).

Based on Figure 8a, b, and c, for the majority of 1st, 2nd and 3rd order channels, for a

given length, the channels in dry basins have larger drainage areas. For example, for $\omega = 2$,

96% and for $\omega = 3$, 77% of channels in dry basins, on an average, have a larger area than

humid channels for the same channel length. Note that, however, for $\omega = 1$, 30% of channels

in dry basins and 58% of channels in humid basins follow similar characteristics. Also note

that, these percentages were computed for a given length below the intersection point of dry

and humid curves which refers to the range of length scales in which for a given link

(channel) length, the link in dry basin corresponds to a larger area than humid basins (see

also inset in Figure 7b). Furthermore, Table 2 shows that the junction density J_d (defined

here as the ratio of number of junctions to total channel length of a basin) in humid basins,

on an average, is larger than the junction density in dry basins. Given a constant D_d and

smaller junction angle in humid basins, this observation suggests that the humid basins/sub-

basins are, in general, relatively smaller in size than dry basins (see also Table 2). Moreover,

these results suggest, that the only way to have a larger junction density J_d and smaller

junction angle (for a constant D_d) is to have smaller link length (channel length of a given order) which was independently calculated and shown in Table 2.

In contrast to the junction angle, the percentage of side branching, i.e. merging of branches (channel links) of different orders, in humid basins is higher than that in dry basins (Table 2). For example, for $\omega =1$, 2 and 3, the percentage of side branching is 75%, 70% and 67% for humid basins; whereas, for the dry basin, it is 72%, 67% and 62%, respectively. This observation of increasing side branching is consistent with findings of *Zanardo et al.* [2013] where they showed that with increasing rainfall the Tokunaga parameter *c* increases, suggesting higher channel feathering in humid conditions. This inference of less feathering in dry basins together with observation that for a given incremental change in contributing area (a proxy for discharge or precipitation), the change in channel length is larger in dry basins than humid basins (Figure 8a, b and c), further suggest that dry basins may have higher potential to change under external forcing (e.g. climate) and are more dynamic as compared to the humid basins [*Zaliapin et al.*, 2010; *Zanardo et al.*, 2013].

Figure 8. a) Length of channels versus drainage area for 1st order (a), 2nd order (b), and 3rd order (c) channels. d), e) and, f) show the pdfs of junction angles for 1st, 2nd, and 3rd order channels, respectively. The red and blue vertical lines in the right panels show median values.

Table 3. Significance test (T-test) performed to differentiate distribution of angles at the 95th %

confidence interval.

pdf (angle)	P-value (T-test)
Total junction angle (dry vs humid)	0.0004
First order junction angle (dry vs humid)	0.0060
Second order junction angle (dry vs humid)	0.0225
Third order junction angle (dry vs humid)	0.0272

In contrast to the junction angle, the percentage of side branching, i.e. merging of branches (channel links) of different orders, in humid basins is higher than that in dry basins (Table 2). For example, for ω =1, 2 and 3, the percentage of side branching is 75%, 70% and 67% for humid basins; whereas, for the dry basin, it is 72%, 67% and 62%, respectively. This observation of increasing side branching is consistent with findings of *Zanardo et al.* [2013] where they showed that with increasing rainfall the Tokunaga parameter *c* increases, suggesting higher channel feathering in humid conditions. This inference of less feathering in dry basins together with observation that for a given incremental change in contributing area (a proxy for discharge or precipitation), the change in channel length is larger in dry basins than humid basins (Figure 8a, b and c), further suggest that dry basins may have higher potential to change under external forcing (e.g. climate) and are more dynamic as compared to the humid basins [*Zaliapin et al.*, 2010; *Zanardo et al.*, 2013].

CHAPTER 3: ROLE OF VARYING CLIMATE ON GEOMORPHIC AND TOPOLOGIC CHARACTERISTICS OF CHANNEL NETWORKS

Landscapes emerge as a result of the interaction between uplift, erosion, subsidence, and sedimentation. This interaction leads to hillslope and fluvial processes which are dynamically coupled while initiating and evolving erosional paths (i.e. channel network). Erosion occurs through two distinct sediment transport processes: fluvial incision and soil creep. Erosion caused by overland flow is described by advection which creates concave-up topographic profiles in the downslope direction. Whereas, erosion caused by soil creep such as resulting from rain splash on hillslopes is described by diffusion which dampens the perturbations and leads to concave-down profiles near the drainage divide [*Gilbert*, 1877; *Hooshyar et al.*, 2019a; *Howard*, 1994; *Kirkby*, 1971; *Perron et al.*, 2009; *Perron et al.*, 2012; *Tucker and Slingerland*, 1997; *Tucker and Bras*, 1998].

Previous studies showed the existence of a characteristic length scale in drainage basins and its relation to the transition from hillslopes to fluvial processes. Arguing that the development of uniform spacing in landscapes is tied to the competition between hillslope and fluvial processes, *Perron et al.* [2008] showed that the valley spacing in a landscape is mainly controlled by a quantity Péclet number (Pe), defined as the dimensionless ratio of advection to diffusion timescales by analogy to a linear advection-diffusion system. However, it remains unclear whether the landscapes with the same Pe exhibit different

channel branching structure although they may have the same valley spacing. The same Pe for two landscapes can imply that the competition between hillslope and fluvial processes in these landscapes is similar although the magnitudes of them can be significantly different which may result in distinct branching patterns of channel networks.

Channel networks are erosional features that transport environmental fluxes such as runoff, sediment, and nutrients [*Basso et al.*, 2015; *Biswal and Marani*, 2010; *Collins and Bras*, 2010; *Czuba and Foufoula-Georgiou*, 2015; *Dietrich et al.*, 1993; *Goren*, 2016; *Horton*, 1932; *Howard*, 1994; *Kelly et al.*, 2016; *Rodriguez-Iturbe and Rinaldo*, 2001; *Rodriguez-Iturbe et al.*, 2009; *Shelef and Hilley*, 2014; *Troch et al.*, 2009; *Wagener et al.*, 2010; *Willett et al.*, 2014]. Several metrics have been used to characterize channel networks' branching pattern. For example, drainage density (D_d), shows the degree of dissection in the landscape. A large body of studies have investigated the relationship between D_d and different processes such as climate, tectonics, soil creep, and fluvial incision [*Abrahams*, 1984; *Collins and Bras*, 2010; *Hooshyar et al.*, 2019b; *Istanbulluoglu and Bras*, 2005; *Kirkby*, 1971; *Madduma Bandara*, 1974; *Melton*, 1957; *Moglen et al.*, 1998; *Sangireddy et al.*, 2016; *Tucker and Slingerland*, 1997; *Tucker and Bras*, 1998]. For example, using catchments located in relatively dry regions, *Melton* [1957] observed that as the climate aridity index (AI) increases, D_d generally increases. AI is defined as the potential evaporation divided by the precipitation. Thus, a higher AI represents a drier climate, whereas a lower AI is associated with a more humid climate [*Budyko*, 1974; *Wang and Tang*, 2014; *Zomer et al.*, 2007]. On the other hand, *Madduma Bandara* [1974] used data from relatively humid areas and reported that D_d shows an increasing trend, as the climate gets more humid. Combining the data from

Melton [1957] and *Madduma Bandara* [1974], *Abrahams* [1984] observed a U-shape relationship between D_d and climate in which an increase or decrease in AI results in an increase in D_d. *Kirkby* [1987] studied the relationship between the source area and valley gradient and predicted a positive relationship between D_d and relief for humid and an inverse relationship for semi-arid regions. *Schumm* [1956] observed a positive relationship between D_d and relief in humid badlands. In contrast to the above findings, *Oguchi* [1997] detected an inverse relationship between D_d and relief in a humid steep mountainous area in Japan. More recently, *Hooshyar et al.* [2019a] showed that there is a strong power-law relationship between the characteristic length and D_d exhibiting two scaling regimes with slopes of -0.63 and -1.01. D_d provides meaningful information about the concentration of channel networks in a specific drainage area; however, it does not describe the spatial topologic arrangement and pattern of these branching networks (i.e. branching structure).

The branching structure of channel networks is related to various hydrologic, geomorphic, and environmental properties of the land surface [*Kirkby*, 1976; *Rodriguez-Iturbe and Valdes*, 1979; *Rodriguez-Iturbe and Rinaldo*, 2001]. Knowledge of the structural, topological and geometrical properties of the channel networks is important to understand and quantify the components affecting the formation of distinct patterns during the landscape evolution as well as to develop predictive models describing the network dynamics under changing environment [*Abed-Elmdoust et al.*, 2016; *Devauchelle et al.*, 2012; *Hooshyar et al.*, 2017; *Horton*, 1932; *Leopold*, 1971; *Snell and Sivapalan*, 1994; *Tokunaga*, 1966; 1978; *Veitzer and Gupta*, 2001]. *Zanardo et al.* [2013] studied the topology of river networks of catchments across the United States using the Tokunaga self-similarity

framework and revealed a significant dependence of the degree of side-branching on the hydro-climatic variables. *Ranjbar et al.* [2018] used an entropy-based approach to analyze the width functions of the natural basins with the same D_d which were located in different climates. Width function is the one-dimensional representation of a two-dimensional channel network and contains critical information about the arrangement of channel networks [*Kirkby*, 1976; *Lashermes and Foufoula-Georgiou*, 2007]. They showed that width functions of the channel networks in dry climate exhibit higher entropy. Higher entropy implies higher complexity and heterogeneity in branching patterns of channel networks. Although these studies provide novel insights about the structure of channel networks under different climates, the knowledge of the quantitative relationship between the emergence of the distinct branching patterns of channel networks and the erosional mechanisms (such as soil creep and fluvial incision) resulting in these patterns is still lacking.

The goal of this chapter is to identify the signature of the varying climate on the topography. As the topographic evolution can be modeled using a numerical landscape evolution model, we assume that different combinations of soil transport and fluvial incision coefficients mimic different climates. Note that transport processes (hillslope and fluvial processes) can be controlled by climate and/or material properties, however here we focus on how the fluvial incision coefficient (K) and the soil transport coefficient (D) may be influenced by climate instead of other factors, such as bedrock type. In particular, we assume that increasing D and K mimic an increase in the rainfall intensity and thus humid conditions. Whereas, decreasing D and K is assumed as a proxy of decreasing rainfall intensity and thus mimicking dry conditions [*Perron*, 2017; *Richardson et al.*, 2019]. By

changing D and K systematically in the governing equation of our landscape evolution model (LEM), we show that having the same Pe we obtain different geomorphic (e.g. D_d) and topologic (e.g. number of junctions and number of branching and side-branching junctions) characteristics. We define junctions as the intersection of two channels (links) and use Horton-Strahler scheme to define the channel orders. When two channels with the same order ω meet at a junction they result in a downstream channel with order $\omega + 1$; this junction is defined as a branching junction. Whereas, when two channels with different orders meet at a junction, the junction is referred to as a side-branching junction [*Abed-Elmdoust et al.*, 2016; *Horton*, 1945; *Peckham*, 1995].

3.1   Landscape evolution model

We model the landscape evolution using the following nonlinear advection-diffusion equation:

$$\frac{\partial h}{\partial t} = D\nabla^2 h - K(A^m |\nabla h|^n - \theta_c) + U, \tag{3.1}$$

where h and t denote the surface elevation and time, respectively; D is the soil transport coefficient; K is a constant characterizing fluvial transport and m and n are exponents; A is the upslope contributing area; θ_c is the fluvial incision threshold; and U is the uplift rate [*Han et al.*, 2015; *Han et al.*, 2014; *Howard*, 1994; *Rinaldo et al.*, 1995b; *Shelef*, 2018; *Smith and Bretherton*, 1972]. The first term on the right-hand side of Eq. (3.1) is a linear diffusion term that characterizes soil creep caused by the mass movement of sediment and naturally smooths the perturbations which can result in increasing (deposition) or decreasing (erosion) the elevation depending on the sign of the Laplacian of the elevation.

The second term is the advection term that characterizes the channelized fluvial erosion and is a nonlinear term since n can be a non-unity number. Also, this term contains A which is a non-local quantity and a function of both position and time. The advection term in Eq. (3.1) can only result in erosion. The third term, tectonic uplift rate U, is the source term that feeds the evolution processes through time. In order to investigate how different terms of Eq. (3.1) control the model topography, *Perron et al.* [2008] proposed a dimensional analysis by non-dimensionalizing Eq. (3.1) with two physical properties of surface topography. Using the relief R, as a vertical length scale and defining l as the characteristic horizontal length scale, the parameters of Eq. (3.1) can be non-dimensionalized and compared with each other. The ratio of dimensionless K and D describes the strength of channel incision relative to soil creep at a chosen scale l. This ratio is analogous to the Pe in a linear advection-diffusion system [*Hooshyar et al.*, 2019a; *Perron et al.*, 2008; *Yao et al.*, 2018]. For $\theta_c = 0$, Pe can be calculated as:

$$Pe = \frac{Kl^{2(m+1)-n}}{DR^{1-n}},$$ (3.2)

where l is the horizontal length scale of the basin. When $n = 1$, Eq. (3.2) can be written as [*Perron et al.*, 2009; *Willgoose et al.*, 1991]:

$$Pe = \frac{Kl^{2m+1}}{D};$$ (3.3)

and Eq. (3.1) can be expressed as:

$$\frac{\partial h}{\partial t} = D\nabla^2 h - K(A^m|\nabla h|) + U.$$ (3.4)

From Eq. (3.2) it can be seen that Pe is a function of relief, R when n is not equal to 1. However, the effect of relief is eliminated from Pe as shown in Eq. (3.3) when n is assumed to be equal to 1. In this case, varying the advection and diffusion coefficients with the same ratio does not affect the Pe value, while leading to significant variations in the vertical scale (relief) but no change in the valley spacing (see Figure 9). Note that with $n \neq 1$, Pe calculation requires the knowledge of relief. However, the relief is not known a priori, and it is not clear how different features of topography emerge as the landscape evolves based on the nonlinear model (Eq. (3.1)). Thus, it is not possible to select landscapes with the same Pe only based on their model parameters when $n \neq 1$. We use $n = 1$, in order to eliminate the relief from Pe calculation.

Setting $Pe = 1$ and solving Eq. (3.3) for l yields a characteristic length shown in Eq. (3.5) that can be defined as the length at which the timescales of diffusive and advective transports are equal.

$$L_c = \left(\frac{D}{K}\right)^{\frac{1}{2m+1}}. \tag{3.5}$$

3.2   Topographic analysis of natural basins

In order to understand the branching behavior in channel networks, we studied 100 natural basins across the United States with various climatic conditions. The study sites covered a wide range of mean annual precipitation (MAP) from 130 mm to 1641 mm and the AI from 0.25 (more humid) to 4.45 (drier). The drainage area of these sites ranged from 0.04 to 4.44 km². The sites were chosen based on the availability of LiDAR data and minimal anthropogenic activities. We calculated D and K from digital elevation models (DEMs) based

on the method proposed by *Perron et al.* [2009] describing the properties of the landscape in terms of advective and diffusive transports. A summary of this method is presented through the Eq. (3.6) to (3.8). The DEMs were sampled at a resolution of 1 m. The diffusion term $D\nabla^2 h$ (see Eq. (3.1)) characterizes the sediment transport on hillslopes; whereas the advection term $KA^m|\nabla h|^n$ is responsible for the sediment transport in channels [*Dietrich et al.*, 1993; *Dietrich et al.*, 2003; *Roering et al.*, 2001; *Smith and Bretherton*, 1972; *Tucker and Slingerland*, 1997]. In order to calculate the local slope ($|\nabla h|$) and laplacian ($\nabla^2 h$) from the DEMs, central finite difference discretization was used. For a steady-state condition, Eq. (3.4) can be expressed as $\frac{\partial h}{\partial t} = 0$, therefore:

$$\frac{D}{U} = \frac{1}{\nabla^2 h}\left(\frac{K}{U}A^m|\nabla h| - 1\right),$$ (3.6)

where $\frac{D}{U}$ can be computed based on the pixels that have a negligible $A^m|\nabla h|$. The average laplacian of those pixels ($\overline{\nabla^2 h_0}$) can be represented as:

$$\frac{D}{U} = -\frac{1}{\overline{\nabla^2 h_0}}.$$ (3.7)

$\overline{\nabla^2 h_0}$ is calculated from the curve of $\nabla^2 h$ versus $A|\nabla h|$. Using the calculated D parameter (Eq. (3.7)), Eq. (3.4) can be expressed as:

$$\frac{\overline{\nabla^2 h_0} - \nabla^2 h}{|\nabla h|\overline{\nabla^2 h_0}} = \frac{K}{U}A^m.$$ (3.8)

Thus, the parameters $\frac{K}{U}$ and m can be further computed by fitting a power function to the curve of $\frac{\overline{\nabla^2 h_0} - \nabla^2 h}{|\nabla h|\overline{\nabla^2 h_0}}$ versus A.

3.3   Results

In order to investigate the landscapes that have the same Pe but different soil transport and fluvial incision, we simulate 19 different landscapes within a fixed grid with a Pe equal to 2600 which is in the defined range of Pe for the branching landscapes (see *Perron et al.* [2008]). This Pe falls in the range where landscapes contain a well dissected branching structure (at least 3rd order channel network). The goal of this chapter is to explore the effects of different hillslope and fluvial processes on the branching structure of the landscapes that exhibit the same Pe. The main hypothesis we put forth is that "landscapes with the same Pe (competition between hillslope and fluvial processes, i.e. erosional processes) can contain different branching patterns representing distinct signatures of climate on channel network topology". We solve Eq. (3.3) for $\frac{K}{D}$ using $Pe = 2600$. Parameter l is determined based on the model domain size (Figure 10). Also, parameter m is selected based on previous studies [*Montgomery and Foufoula-Georgiou*, 1993; *Perron et al.*, 2008; *Perron et al.*, 2009]. In order to consider different soil creep and fluvial incision, multiple values of D and K are selected to satisfy the obtained ratio of $\frac{K}{D}$ and be in the physically possible range, with known m and l. This way we achieved different landscapes maintaining a constant Pe and L_c. For all of our simulations $L_c = 5.5\ m$. Note that for all simulated landscapes, model parameters including m, l and $\frac{K}{D}$ are kept constant and the only varying parameters are D and K. Table 4 shows the LEM parameters, whereas Table 5 shows the different D and K for all the scenarios considered in this study.

In particular, we select our first set of D and K (original landscape) based on the D and K of natural basins computed using the framework presented in section 3.2 and then: i) increase both D and K, and ii) decrease both D and K systematically with increments of 10%, while all other parameters are kept constant such that Pe and L_c are constant for the entire parameter sets. For example, a 10% increase in D and K implies that $D_{10\% \text{ inc}} = 1.1 \times D_{\text{original}}$ and $K_{10\% \text{ inc}} = 1.1 \times K_{\text{original}}$; whereas, 10% decrease in D and K denotes $D_{10\% \text{ dec}} = 0.9 \times D_{\text{original}}$ and $K_{10\% \text{ dec}} = 0.9 \times K_{\text{original}}$, respectively.

Table 4. Model parameters, which are constant in this study.

Description	Parameter	
Advection exponent	m	0.3
Advection exponent	n	1
Used for solving eq. 4	$dt\ (yr)$	370
Cell size	$dx\ (m)$	5
Number of cells in x direction	N_x	300
Number of cells in y direction	N_y	300
Uplift rate	$U\ (m\ yr^{-1})$	0.0001
Péclet number	Pe	2600
Characteristic length	$L_C\ (m)$	5.5

Table 5. Summary of different scenarios and their D and K coefficients.

Scenario	Description	$D\ (m^2\ yr^{-1})$	$K\ (m^{1-2m}yr^{-1})$
Original	First landscape	$D_0 = 0.003523$	$K_0 = 0.00023$
Humid	Increased D and K mimicking more humid climate (varied systematically from 10-90% with increments of 10%).	$D = 1.1 \times D_0$ $.$ $.$ $.$ $D = 1.9 \times D_0$	$K = 1.1 \times K_0$ $.$ $.$ $.$ $K = 1.9 \times K_0$
Dry	Decreased D and K mimicking drier climate (varied systematically from 10-90% with increments of 10%)	$D = 0.9 \times D_0$ $.$ $.$ $.$ $D = 0.1 \times D_0$	$K = 0.9 \times K_0$ $.$ $.$ $.$ $K = 0.1 \times K_0$

After calculating D and K, we simulate the landscape using the LEM discussed in section 3.1. A constant uplift rate $U = 0.0001$ m/year was used in these modeling experiments. The LEM governed by Eq. (3.4) was solved numerically using a finite difference discretization (central in space and forward in time) with a 5-m discretization size in both x and y directions. The stability of the Eq. (3.4) is only dependent on that of the advection term since the diffusion term is unconditionally stable. The stability of the numerical solutions to the kinematic wave equations is subject to the Courant-Friedrichs-Lewy stability criterion. This criterion for the advection term of Eq. (3.4) can be expressed as (see *Perron et al.* [2008]):

$$\frac{\sqrt{2}KA^m|\nabla z|^{n-1}dt}{dx} \leq 1. \tag{3.9}$$

In order to satisfy the stability criterion, a sufficiently small dt was used in simulations that satisfies Eq. (3.9) over the entire domain for all simulations. The simulation domain was 300 by 300 cells ($N_X = N_y = 300$) with a grid size of 5 m ($dx = 5\,m$) which resulted in a 1.5-km by 1.5-km rectangular grid and a 1-m relief and superimposed random noise as the initial conditions [*Hooshyar et al.*, 2019a; *Shelef*, 2018]. Dirichlet boundary conditions (constant elevation) at two lower boundaries and periodic boundary conditions at the other two sides were imposed as the boundary conditions. Periodic boundary conditions in the longitudinal axis (here, x-axis) imply that the x-direction of the studied grid is periodic, i.e. the ridgeline of the x-direction in the model periodically extends to infinity with a period of $N_X dx$. The D_∞ algorithm was used to calculate the upslope area [*Tarboton*, 1997].

Previous studies have investigated the relationship of D and K with climate proxies. For example, *Hanks* [2000] and *Hurst et al.* [2013] suggested that D may be larger in more humid climates. *Richardson et al.* [2019] compared D with MAP and AI and observed a power-law relationship between D and both MAP and AI. *Ferrier et al.* [2013] found that K for Kauai's rivers increases as a power function of MAP. In contrast, *Molnar* [2001] suggested that dry landscapes may experience higher K due to changes in flood frequency even though dry landscapes receive less rainfall. More recently, *Perron* [2017] showed that both D and K exhibit a power-law relationship with MAP. In summary, D and K may exhibit varying trends. However, in this study, in order to investigate the landscapes with the same characteristic length, but different D and K, we assume that the proportional increase in D and K implies a more humid basin. As mentioned before, we selected our first D and K based on D and K computed for the natural basins. We selected the average D and K parameters of the basins with an AI close to 1 as the first set of parameters in a way that they satisfy $Pe = 2600$ with known m, l, and $\frac{K}{D}$. We refer to this landscape as the original landscape. Consequently, increasing D and K may imply more humid climates whereas decreasing D and K may imply drier climates. We refer to the scenarios with increased D and K (9 landscapes) as "humid scenario", and the scenarios with decrease D and K (9 landscapes) as "dry scenario".

Figure 9(a) shows the average profiles of the topographic elevation of the simulated landscapes. Note that all of our simulated landscapes have the same Pe and L_c. The relief profile of the original scenario is shown by a yellow solid line. The 9 profiles shown with the dashed lines (colder colors) are associated with the landscapes where D and K are increased

(humid scenario), whereas solid lines (warmer colors) correspond to the landscapes where D and K are decreased (dry scenario). As demonstrated in Figure 9(a), landscapes with the same Pe but different D and K exhibit different reliefs. When D and K of the humid and dry landscapes are compared to those of the original scenario, it can be observed that a systematic increase and decrease in D and K of the original scenario, result in a decrease and increase in the relief, respectively. The relief change varies for the increase and decrease of D and K. Figure 9(b) shows the ratio of the average relief (measured from main drainage divide to the outlet) in the landscapes with increased (cold colors) and decreased (warm colors) D and K to the original (yellow) landscape, versus the percent change in D and K compared to the original landscape. For the landscapes with increased D and K, the decrease in the relief is much smaller and follows almost a linear relationship (exponent of the fitted exponential curve is close to zero; see Figure 9(b)). In contrast, the increase in the relief of the landscapes with decreased D and K follows an exponential behavior with an exponent of 0.02, representing higher rate of change in relief.

Figure 10 shows the schematic view of three landscapes obtained by the LEM discussed in section 3.1: i) the original landscape (yellow in Figure 9), ii) 60% increase in both D and K (a case in humid climate), and iii) 60% decrease in both D and K (a case in dry climate). As shown in this figure, by increasing D and K with the same percentage, the relief of the landscape decreases and by decreasing D and K with the same percentage the relief of the landscape increases (although much drastic in the case of decrease in D and K).
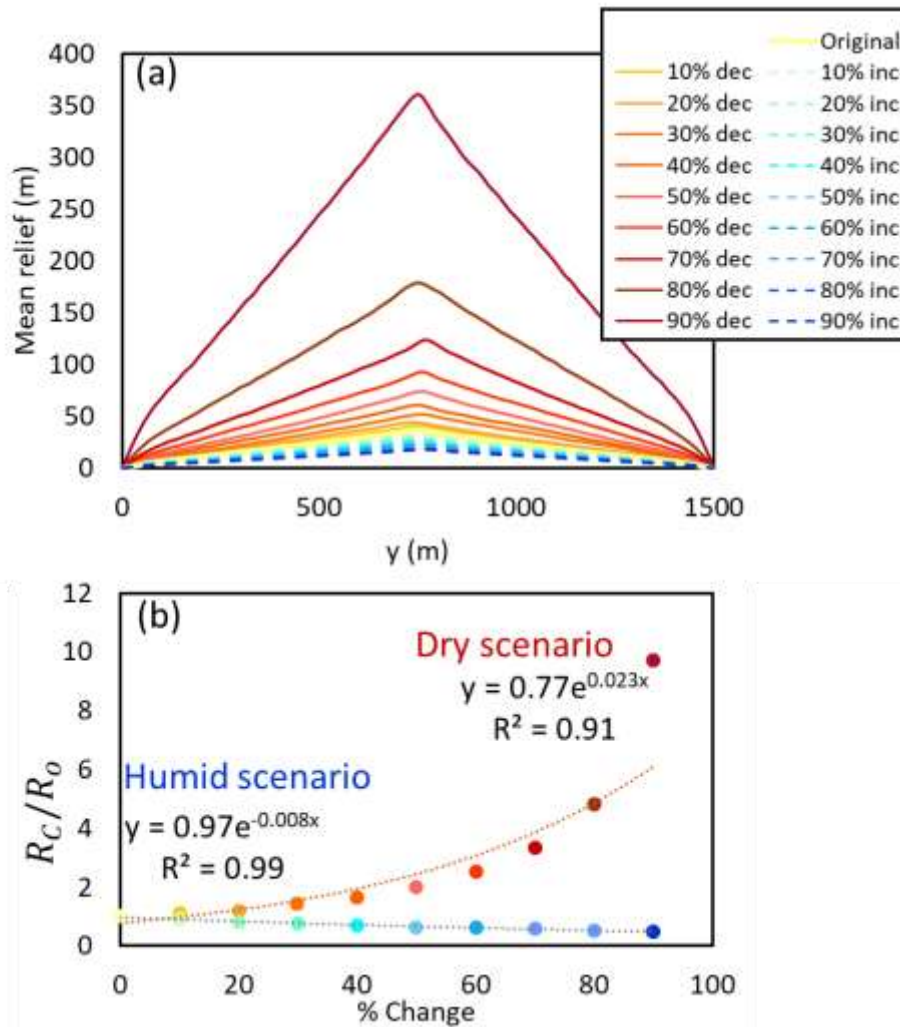
Figure 9. (a) Average elevation profiles of the simulated landscapes in original, dry and humid scenarios. The thick yellow line shows the average profile of the landscape from original scenario, and the dashed lines (colder colors) are associated with the landscapes where D and K are increased (humid scenario), whereas solid lines (warmer colors) correspond to the landscapes in where D and K are decreased (dry scenario). (b) Plot of the ratio of mean relief (R_c) in humid and dry scenarios and the mean relief of the landscape in original scenario (R_0), versus percent change in D and K parameters in humid and dry scenarios.
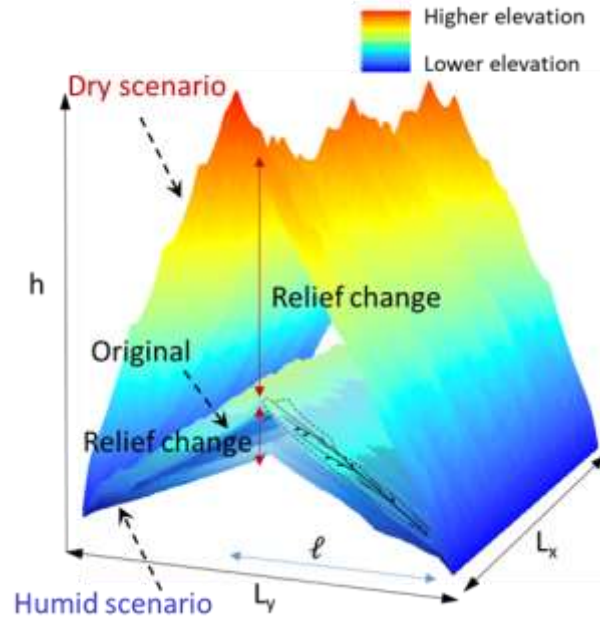
Figure 10. Schematic representation of three different landscapes with the same Pe. The original landscape (which is referred to as original scenario) is generated using $D_0 = 0.003523$ and $K_0 = 0.00023$ and the set of parameters shown in Table 4. Different colors represent the elevation of the surface. The domain size is shown by L_x and L_y. The landscape with the lowest relief corresponds to a case in humid scenario (60% increase in D and K), whereas the landscape with the highest relief is associated with a case in dry scenario (60% decrease in D and K). As can be seen, the relief change for dry scenario is much larger than that in humid scenario.

To identify the effects of relief change on the evolved landscapes with different combinations of D and K, however, with the same ratio (same Pe), we compared their channel branching structures via commonly used geomorphic (e.g. D_d) and topologic (e.g. number of junctions and number of branching and side-branching junctions) properties of the landscapes. Note that although the simulations achieved steady-state (the mean elevation does not change [*Hack*, 1957; *A Singh et al.*, 2015]; here achieved at ~ 5 Myr for the elevation) earlier, the simulations were run for a longer time (40 Myrs) in order to minimize

the D_d fluctuations (i.e. to achieve a steady behavior of D_d with time). The DEMs were recorded at each time step.

The drainage networks of the landscapes were extracted at every 370,000 years using a curvature-based method developed by [*Hooshyar et al.*, 2016]. In this method, the surface convergence is computed by the curvature using equation 10.

$$\kappa = \nabla.\frac{\nabla h}{|\nabla h|}. \tag{3.10}$$

This equation quantifies the divergence/convergence of the water flow and represents the contour curvature. In order to compute the curvature, the DEMs were smoothed using the Perona-Malik nonlinear diffusive filter *[Perona and Malik, 1990]*. The pixels with a curvature higher than a threshold at which the distribution of the curvature deviates from normal distribution were defined as the convergent pixels [*Lashermes et al.*, 2007; *Passalacqua et al.*, 2010]

After extracting the channel networks of the simulated landscapes, D_d was computed for the original landscape and compared with the average D_d of the landscapes with i) increased D and K, and ii) decreased D and K. Figure 11(a) shows that D_d increases, compared to the original landscape, either by increasing D and K (landscapes from humid scenario) or by decreasing D and K (landscapes from dry scenario). 'Humid' and 'Dry' in this figure represent the average D_d for all 9 landscapes in humid and dry scenarios, respectively.

As shown in Figure 11(b) for both cases of increasing and decreasing D and K, the number of junctions increases. However, the additional junctions emerged in these landscapes are a consequence of two distinct combinations of erosional processes.

Therefore, they may contain information about the formative processes. We categorize them into branching and side-branching junctions and calculate their numbers in the simulated landscapes. Figure 11(c) shows the number of branching junctions in the landscape for the original scenario and compares it with the average number of branching junctions in the landscapes for humid and dry scenarios. The number of branching junctions increases when D and K are decreased. However, this number does not change when D and K are increased. This observation suggests that the extra junctions added to the river network in the case of increasing D and K are mostly side-branching junctions since the number of branching junctions remains almost unchanged.

The inset in Figure 11(c) shows the comparison between the exceedance probabilities of the number of branching junctions for landscapes of humid and dry scenarios. From this figure, it can be seen t

hat more than 50% of the humid scenario landscapes have more than 37 branching junctions. Whereas, more than 50% of the dry scenario landscapes have more than 45 branching junctions. Based on this figure, it can be inferred that the number of branching junctions is generally higher in the landscapes of dry scenario compared to the landscapes of humid scenario. Note that this figure contains every recorded landscape through time for all 9 landscapes in humid and dry scenarios. Similar to the number of side-branching junctions, the percentage of side-branching junctions defined as the number of side-branching junctions divided by the total number of junctions is also larger for the landscapes in humid scenario (not shown here for brevity).

Figure 11(d) shows the comparison of the number of side-branching junctions for the landscape of original scenario and the average number of side-branching junctions for the landscapes in humid and dry scenarios. From this figure, it can be seen that the number of side-branching junctions is the largest for the landscapes from humid scenario. The inset in this figure shows the exceedance probability of number of side-branching junctions for humid and dry scenarios. For instance, more than 50% of the landscapes in humid scenario have more than 230 side-branching junctions. However, for dry scenario, more than 50% of the landscapes have more than 210 side-branching junctions. Figure 11(e) and (f) show simulated landscapes and their superimposed channel networks as examples from the dry and humid scenarios, respectively.
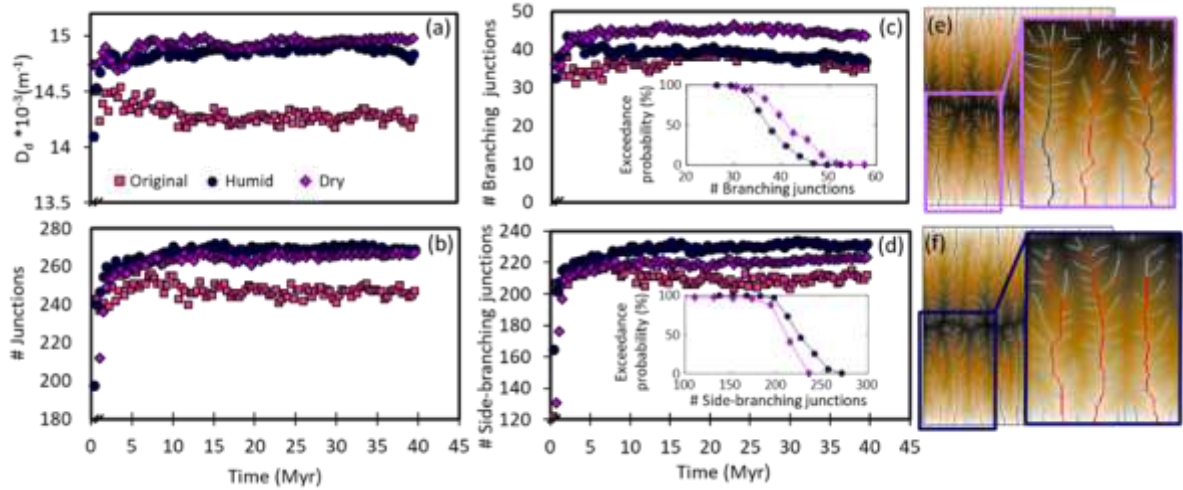
Figure 11. (a) Drainage density, D_d, (b) number of junctions, (c) number of branching junctions and, (d) number of side-branching junctions of the landscape in original scenario compared with their average in humid and dry scenarios. Insets in (c) and (d) show the exceedance probability of branching and side-branching junctions in all landscapes of humid and dry scenarios during the evolution, respectively. From the insets in (c) and (d) it can be observed that the number of branching junctions is higher for the dry scenario landscapes compared to the humid scenario landscapes and the number of side-branching junctions increases when the landscape transitions to a more humid conditions (i.e. changing from original scenario to humid scenario). (e) and (f) show examples from the landscapes in dry and humid scenarios, respectively. The 1st, 2nd, and 3rd-order channels are shown in blue, red, and black, respectively.

3.4   Discussion

In Figure 12, we show the results of the simulated landscapes at the steady-state condition for every 19 simulations. As can be seen from Figure 12 (a), D_d increases in almost all scenarios including 9 humid and 9 dry scenarios compared to the original landscape. The average increase in D_d is approximately 4 % for both scenarios. Figure 12(a1) and (a2) demonstrate schematic representation of two different possible ways of increase in D_d: i) by

increasing the link length without adding new junctions in the river network (as depicted by extended dashed lines in Figure 12(a_1)), and ii) by adding new junctions to the river network (Figure 12(a_2)). D_d can also increase as a combination of (i) and (ii). In order to detect how D_d increases for the humid and dry scenarios, the number of junctions for every scenario is computed and shown in Figure 12(b). As can be seen from this figure, for both humid and dry scenarios, on average, the number of junctions increases as compared to original landscape. This increase for the dry scenario is 8.5 % whereas for the humid scenario it is 8 %. Therefore, extending the link length for increasing D_d, without adding new junctions as shown in Figure 12(a_1) is not the case for either of the scenarios. New junctions are added to the channel networks in both humid and dry scenarios. As mentioned above, a junction can be branching or side-branching. Figure 12(b_1) and (b_2) show schematically, two different possible ways of increase in the number of junctions in a channel network. In Figure 12(b_1) the number of junctions is increased by adding new branching junctions, whereas, in Figure 12(b_2) it is increased by adding new side-branching junctions to the channel network. In order to explore how the number of junctions has increased in humid and dry scenarios, we show the number of branching and side-branching junctions in every humid and dry scenarios.

As can be seen from Figure 12(c) and (d), the number of branching is higher on average in dry scenarios, suggesting the case shown in Figure 12(b_1). The increase in the branching junctions for the dry scenario is about 18 %. However, in humid scenarios the number of side-branching junctions is higher, therefore, may represent the case shown in Figure 12(b_2). The increase in the side-branching junctions in humid scenario is about 11 %.

From Figure 12, it can be concluded that when the soil creep and fluvial incision increase, more side-branching junctions are added to the channel network (Figure 12(b$_2$)). However, in the case of decreasing the soil creep and fluvial incision, more branching junctions are added to the channel network (Figure 12(b$_1$)). It should be noted that, in general, the channel networks in different cases of dry and humid scenarios remained 3rd-order channels and the order did not change compared to the original scenario. The increase in the number of branching junctions in dry scenarios is a consequence of new channels added to the 1st-order channels. Whereas, in humid scenarios the new channels (e.g. 1st-order channels) are added to the higher-order channels, i.e. 2nd or the 3rd-order channels as side-branching channels. In other words, our results indicate that decreasing D and K influences smaller scale features (i.e. by branching 1st-order channels) whereas increasing D and K results in side-branching that may influence larger-scale features (e.g. by 1st-order channels attaching themselves to higher-order channels). A similar observation can be made from Figure 11(e) and (d) where zoomed-in landscapes obtained from numerical modeling are shown. For example, Figure 11(e), a case from dry scenario where D and K are decreased, contains more branching junctions as evidenced from larger number of 2nd-order channels, whereas Figure 11(f), a case from humid scenario where D and K are increased, contains more side-branching junctions and less number of 2nd-order channel.
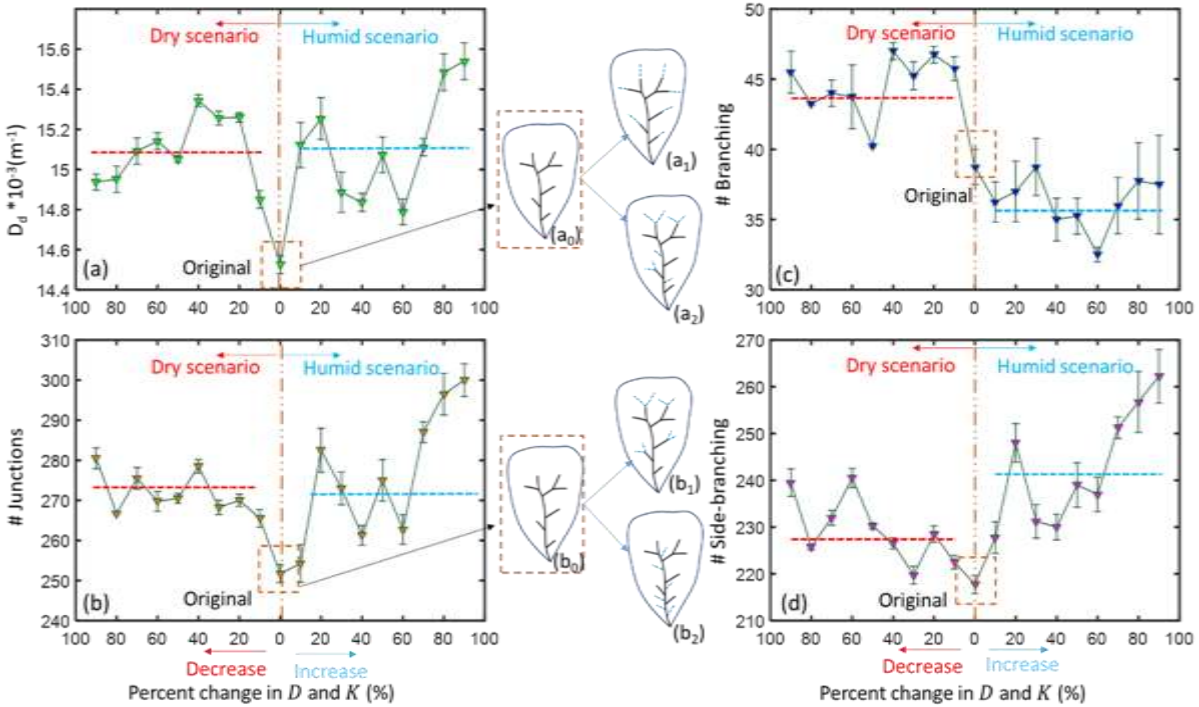
Figure 12. (a) Drainage density, D_d, (b) number of junctions, (c) number of branching junctions, and (d) number of side-branching junctions for every humid and dry scenario. The x-axis shows the percentage change in D and K for each scenario. 0 on the x-axis implies the original scenario. Horizontal dashed bars show the average quantities for dry (red) and humid (blue) scenarios. (a0) and (b0) are schematic representations of a simple channel network. (a1) and (a2) are two different ways of increasing D_d from (a0). (b1) and (b2) are two different ways of increasing the number of junctions from (b0). The error bars represent one standard deviation from the mean computed for multiple simulations starting with different initial noise.

To further illustrate the relationship between the branching structure and climate, we performed an analysis on 100 natural basins across the United States to characterize the branching structure quantitatively. One formal way to characterize branching river network is via Tokunaga self-similarity (see section 4.2). Note that, the robust calculation of Tokunaga

parameter requires channel networks > 4th or 5th order; therefore, Tokunaga analysis was only performed on natural basins.

Figure 13(a) shows the correlation between the Tokunaga parameter (c-value) of the studied basins with MAP. It can be seen that the c-value is positively correlated with MAP for 100 studied basins with various climatic conditions. The correlation is evaluated by the Pearson linear coefficient, r. Further statistical tests show that the correlation is considerably significant (P-value = 0.001). This suggests that changing to humid conditions the basin initiates new channels that are side-branched rather than branched. This further implies that, under changing climate to a more humid climate, for a basin to account for additional water and sediment to be drained, new channels may need to emerge and one way for the basin to accomplish this is via initiating side-branching.

In Figure 13(b) and (c) we analyzed the relationship between D and K obtained from the natural DEMs and climate (MAP) of these study basins. From these figures, it can be seen that basins with higher precipitation exhibit higher D and K. Although the correlation values are not extremely high, further statistical analysis show that the correlation is significant (i.e. P-value < 0.01 for Figure 13(b) and P-value ~ 0.05 for Figure 13(c)). The observations from Figure 13(b) and (c) confirm that by increasing both D and K parameters the landscape may experience a more humid climate, whereas by decreasing D and K one may mimic drier climatic conditions. The observed scatter in these plots (Figure 13) might be due to the fact that the studied catchments are located in spatially distinct environments with varying geologic and hydrologic conditions.
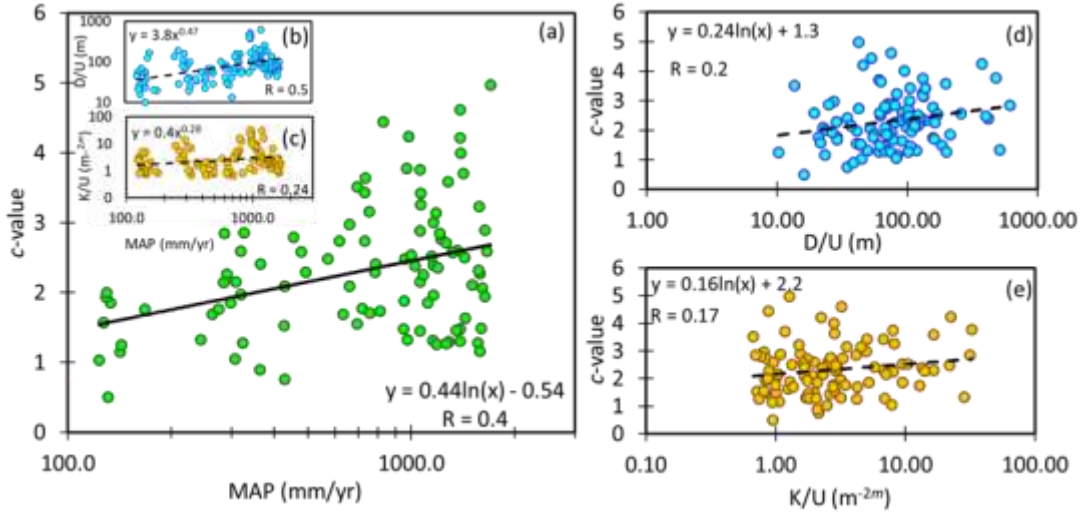
Figure 13. (a), (b), and (c) show the relationship between c-value, diffusion coefficient (D), and advection coefficient (K) with MAP, respectively. (d) and (e) show the relationship of diffusion coefficient (D) and advection coefficient (K) with c-value. For (a), (b), and (c) as shown in the figures although the Pearson correlations coefficient, R is not extremely high, further statistical tests indicate that the correlations are significant. However, for (d) and (e) the correlations are not significant (based on P-value).

We further investigate the correlation between D and K and c-value. The results are shown in Figure 13(d) and (e). It can be seen that although an increasing trend exists for the correlation of c-value with D and K, the correlation is not that significant (P-value is > 0.05 at 95% confidence interval). This implies that although c-value is significantly correlated with MAP, it may not be only controlled by D and K in natural basins; other geomorphic processes operating on landscape evolution in nature, such as groundwater and landslides, may also influence c-value. *Hooshyar et al.* [2019b] suggested a relation between D_d, link lengths and channel junction angles (see also [*Hooshyar et al.*, 2017]). *Seybold et al.* [2017] found that channel junction angles vary with climate. They concluded that these differences

are due to more humid landscapes being dominated by groundwater seepage while arid landscapes primarily experience incision by overland flow. In our model, we assume that landscape evolution is only governed by fluvial incision and soil creep. Therefore by increasing both D and K which implies more humid climate, the side-branching increases.

For the purpose of visualization, in Figure 14 we show four natural basins with varying shapes and sizes located in different climates. Basins (A) and (B) have approximately the same L_c (as assumed in our model) but are located in dry and humid climates, respectively. As shown in this figure, the river network of the basin in dry climate is less feathered (contains less side-branching) than the river network of basin (B) which is located in a relatively humid climate. The c-values of basins (A) and (B) are 0.8 and 3.22, respectively. Higher c-value indicates higher side-branching.

Similar observations can be made from basins (C) and (D) which have higher L_c than basins (A) and (B). Here, again the basin located in humid climate (D) exhibits higher side-branching represented by a larger c-value compared with the basin (C) which is in dry climate. The percentage of side-branching in basin (D) is 70% whereas for basin (C) it is 60%. In general, the average percentage of side-branching and branching junctions in the studied natural landscapes is observed to be ∼ 70% and 30%, respectively. Note that, the average percentages of side-branching and branching junctions in the simulated landscapes are 85% and 15%. The difference in the branching and side-branching proportions of the simulated and natural basins is likely to be related to their L_c. The average L_c of the natural basins was computed as ≈ 13 m whereas the L_c of simulated landscapes is equal to 5.5 m. L_c controls the valley spacing and to some extent, the width of the emerged basins. A larger

width can provide the channel enough area to branch easily. However, for basins with smaller widths, there is not enough space for branching and thus may result in side-branching channels.
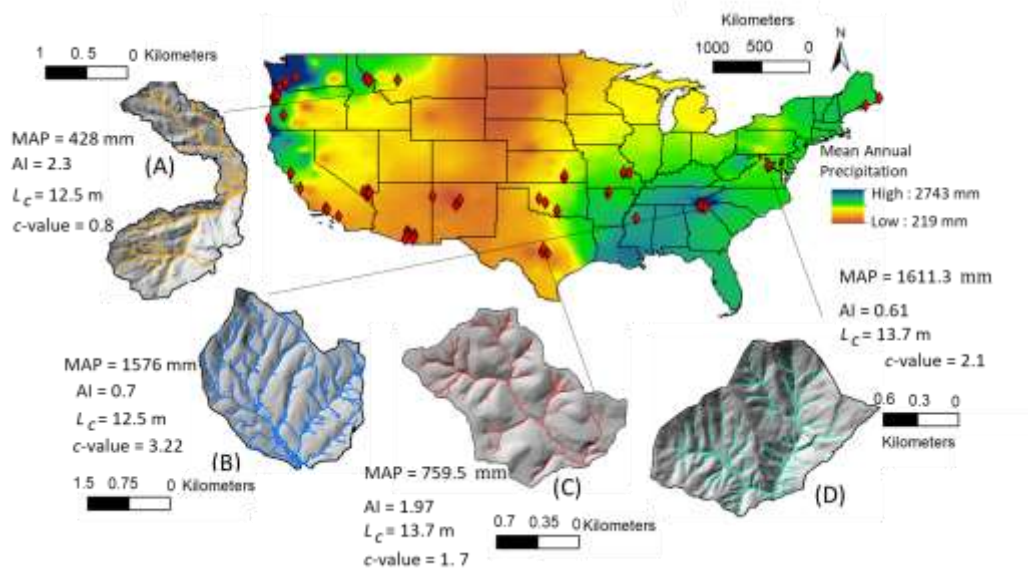
Figure 14. Four examples of natural basins located in different climatic conditions exhibiting different branching patterns. Basin (A) is located in dry climate and basin (B) is located in humid climate; while they have similar L_c , basin (B) contains more side-branching compared to basin (A). Similarly, basin (C) is located in dry climate and basin (D) is located in humid climate; while basins (C) and (D) have similar L_c, basin (D) contains more side-branching compared to basin (C).

CHAPTER 4: EXPLORING THE ROLE OF TOPOLOGICAL CONNECTIVITY ON THE STRUCTURAL AND FUNCTIONAL COMPLEXITY OF RIVER NETWORKS

Landscapes contain fundamental natural features such as channel networks that exert significant control on catchment hydrology [*Bonetti et al.*, 2020; *Gupta and Mesa*, 1988; *Horton*, 1932; *Rodriguez-Iturbe and Valdes*, 1979; *Snell and Sivapalan*, 1994]. These dendritic features are known to deliver environmental fluxes to the outlet via multiple pathways that are highly complex in structure (consisting of topology and geometry) resulting from both internal dynamics and external forcing (e.g. climate and tectonics) [*Dietrich and Dunne*, 1993; *Dietrich et al.*, 2003; *Hack*, 1957; *Hooshyar et al.*, 2016; *Horton*, 1945; *Kirkby*, 1976; *Lashermes et al.*, 2007; *Leopold*, 1971; *Marani et al.*, 1994; *Orlandini et al.*, 2011; *Passalacqua et al.*, 2010]. The channel network (CN) evolved in a catchment reflects the interplay between different geomorphic processes. Understanding and quantifying the complexity in structural and functional patterns emerged in catchments is important for developing quantitative models to predict the catchment behavior in various climatic conditions as well as identifying the roles of different processes in creating these complex patterns [*Casagrande et al.*, 2015; *Gilbert*, 1877; *Howard*, 1994; *Kirkby*, 1971; *Paik and Kumar*, 2010; *Perron*, 2017; *Tucker and Bras*, 1998].

Width functions (W(x)) and area functions (A(x)) are the one-dimensional representations of a two-dimensional CN. *Troutman and Karlinger* [1984] examined the mean properties of W(x) for the random topology model. *Veitzer and Gupta* [2001] established the relationship between W(x) and Horton's scaling properties and used W(x) as a topologic and geometric descriptor to study self-similarity of CNs. *Czuba and Foufoula-Georgiou* [2015] used a response function to explore the CN's hierarchical branching structure and its relation with the heterogeneity of flux distribution in a catchment. *Gangodagamage et al.* [2014] argued that the incremental increase in the contributing area along the mainstream of rivers is directly related to the spatial heterogeneity of environmental fluxes entering the CN from hillslopes and side tributaries, whereas *Zaliapin et al.* [2010] suggested a relation between river network's branching structure and its environmental transport by describing the transport on the river network using a dynamic tree approach.

As discussed above, a catchment may exhibit significant complexity on different aspects of the CN, i.e., the complexity in organization of channels (topology; defined as the connectivity between channels and junctions in a network) and their geometry and the complexity in the flux transport (dynamics) on the CN. We refer to the complexity in channel organization and flux transport as the structural complexity and functional complexity, respectively [*Knudby and Carrera*, 2005; *Larsen et al.*, 2012; *Yang et al.*, 2017]. In this chapter, we aim to study the structural and functional complexity of catchments using two different representations of their CN: width function W(x) and incremental area function IA(x). W(x) is defined in section 2.1. W(x) characterizes patterns of organization of channels

and how they are distributed structurally in a drainage catchment [*Czuba and Foufoula-Georgiou*, 2015; *Lashermes and Foufoula-Georgiou*, 2007; *Ranjbar et al.*, 2018]. On the other hand, IA(x) determines the incremental increase in the contributing area along the main channel in a CN and depicts the patterns of flux delivery to the outlet of a catchment from the tributary junctions by also accounting for the transport on unchannelized surface (hereafter referred to as hillslope) [*Duncan et al.*, 2009; *Gangodagamage et al.*, 2011; *Gangodagamage et al.*, 2014; *Rodriguez-Iturbe et al.*, 2009]. Tributary junctions are locations on the CN where water, sediment, nutrients, and pollutant fluxes increase abruptly. They also reflect the ecologic and morphologic transitions and discontinuities [*Convertino et al.*, 2007; *Richards-Pecou*, 2002]. Assuming that the fluxes are proportional to the drainage area that generates them, IA(x) provides additional insights into the spatial heterogeneity and scaling of the mentioned environmental fluxes and how the flux on a CN is being transported along the main channel.

In this study, we focus on the complexity of CN using W(x) and IA(x) and the factors contributing to their complexity such as topology. Characterizing CNs' structure based on their topological properties provides significant information for identifying the signatures of existent processes and forcing in the past and predicting the future. One way to characterize the topology of a CN is via Tokunaga self-similarity model [*Tokunaga*, 1966; 1978]. Tokunaga self-similarity has been studied not only in hydrology but also as a benchmark criterion in network modeling [*Mcconnell and Gupta*, 2008; *Turcotte et al.*, 1998]. This model describes the degree of side-branching in a CN with two constants. *Zanardo et al.* [2013] showed that

the river networks across the United States obey the Tokunaga self-similarity. According to *Cui et al.* [1999], the influence of regional controls on CN is related to Tokunaga parameters.

In order to study the complexity, we use an entropy-based method at multiple scales [*Fiorentino et al.*, 1993; *Leopold and Langbein*, 1962; *Porporato et al.*, 2007; *V P Singh*, 1997], which characterizes the variability in fluctuations of a series by computing the repetition of the embedded patterns (see section 0 to 2.4) [*Costa et al.*, 2002; 2005]. The questions we address in this chapter are: i) does the topology, or more specifically the degree of side-branching influence the structural and/or functional complexity in CNs and, ii) what physical processes/features contribute to increase in complexity?

4.1 Constructing W(x) and IA(x) of the studied catchments

In order to perform the complexity analysis, we selected 40 catchments across the United States. The criteria for selecting these catchments were the longer channel length and the order of the CN. The selected catchments contained between 3rd and 6th order channels. Also, the selected catchments were all in natural conditions. CN of these catchments was obtained from a 5 m resolution digital elevation model (DEM) using a curvature-based method developed by *Hooshyar et al.* [2016] (see also *Lashermes et al.* [2007] and *Passalacqua et al.* [2010]). After extracting the CN, W(x) was computed using Eq. (2.1).

For IA(x), we start from the channel head on the main channel (i.e., the longest channel in the catchment) and move towards the outlet and measure the incremental contributing area at every dx. Thus, IA(x) captures the lateral contributing area from the hillslopes and tributary junctions. IA(x) can be expressed as:

$$IA(x) = A(x + dx) - A(x), \qquad\qquad (4.1)$$

where $A(x)$ is the contributing area on the main channel at a distance x from the longest channel's head [*Gangodagamage et al.*, 2014]. It should be noted that both W(x) and IA(x) contain information about the CN. W(x) captures the integrated number of channels from all sub-basins located at a flow path of x and $x + dx$ from the outlet; while IA(x) captures the flux contribution from the hillslopes and newly added tributaries along the main channel located between the distances x and $x + dx$. It has been shown that W(x) can be derived from a convolution of the individual sub-basin IA(x) of all tributaries as they join the main channel (for details, see *Gangodagamage et al.* [2014]).

4.2   Quantifying the topology of a CN

CNs have been recognized to exhibit self-similar structure for a range of scales. Characterizing CNs' structure based on their topological properties provides significant information for identifying the signatures of existent processes in the past and predicting future. It has long been known that CNs control natural processes such as sediment and nutrient transport, sediment size distribution, and freshwater biodiversity. Central to comprehending the scaling properties of CN is the ordering system used to categorize the channels. *Horton* [1945]and *Strahler* [1957]developed a stream-ordering framework to classify the CNs. Based on this framework, two same order (ω) channels at a junction form a channel with an order of $\omega + 1$. However, two channels with different orders (ω and ω') at a junction form a channel with the order of max(ω, ω'). Horton's scaling laws, bifurcation, length and area ratios are defined as the number of channels, average length of channels, and

average contributing area in channels with orders of ω divided by those of order $\omega - 1$.

Kirchner [1993] showed that the Hortonian scaling laws are statistically inevitable and describe virtually all possible networks; thus do not compel any particular conclusion about the origin and structure of the CN. He argued that these scaling laws are indifferent to the network structure and are the consequence of Strahler ordering scheme. *Tarboton* [1996] showed that Horton's laws are statistical descriptors of self-similarity and only hold on average. He argued that the channels of different orders meeting more than one order higher channels, introduce a downward bias into the bifurcation ratio and this bias can only be avoided if the structure of the CN is Hortonian (channels only can meet one order higher channels). *Tokunaga* [1978] introduced a framework for describing the CN structure without the above problem. This framework characterizes the topological connectivity in a network and is based on two assumptions; first, the mean number of T_{ij} branches of order i connecting to randomly selected branch of order j is independent of the branch orders and it only depends on the difference *i-j*. T_{ij} can be expressed as $T_{i(i+k)} = T_k$. The mean number of branches of order *i* joining branches of order *j* can be computed as:

$$T_{ij} = \frac{N_{ij}}{N_j} \qquad (4.2)$$

where N_{ij} is the number of channels of order *i* joining channels od order *j*; and N_j is the total number of channels of order *j*.

Second, T_k has an exponential relationship with *K* as:

$$T_k = ac^{k-1} \qquad (4.3)$$

where a and c are constants. The parameter c is called the Tokunaga parameter (hereafter referred to as c-value) which describes the degree of side-branching.

Figure 15 shows an example of a 4th-order Tokunaga self-similar channel network. Tokunaga parameters for this channel network can be calculated as follows: As can be seen from this figure, the number of 1st, 2nd, 3rd, and 4th-order channels is $N_1 = 54$, $N_2 = 13$, $N_3 = 3$, and $N_4 = 1$. The number of 1st-order channels joining other channels is $N_{12} = 13$, $N_{13} = 12$, $N_{14} = 3$. The number of 2nd-order channels connecting to other channels is $N_{23} = 3$, $N_{24} = 4$. Similarly, the number of 3rd-order channels joining 4th-order channels is $N_{34} = 1$. T_{ij} can be calculated as:

$$T_{12} = \frac{N_{12}}{N_2} = \frac{13}{13} = 1, T_{23} = \frac{N_{23}}{N_3} = \frac{3}{3} = 1, T_{34} = \frac{N_{34}}{N_4} = \frac{1}{1} = 1$$

$$T_{13} = \frac{N_{13}}{N_3} = \frac{12}{3} = 4, T_{24} = \frac{N_{24}}{N_4} = \frac{4}{1} = 4$$

$$T_{14} = \frac{N_{14}}{N_4} = \frac{3}{1} = 3$$

Therefore, T_k values can be obtained as:

$$T_1 = \frac{T_{12} + T_{23} + T_{34}}{3} = \frac{3}{3} = 1$$

$$T_2 = \frac{T_{13} + T_{24}}{2} = \frac{8}{2} = 4$$

$$T_3 = \frac{T_{14}}{1} = \frac{3}{1} = 3$$

Based on calculated T_k values, a and c (Tokunaga parameters) can be calculated by fitting an exponential curve to K-1 and T_k. In this example, c-value is 1.73.
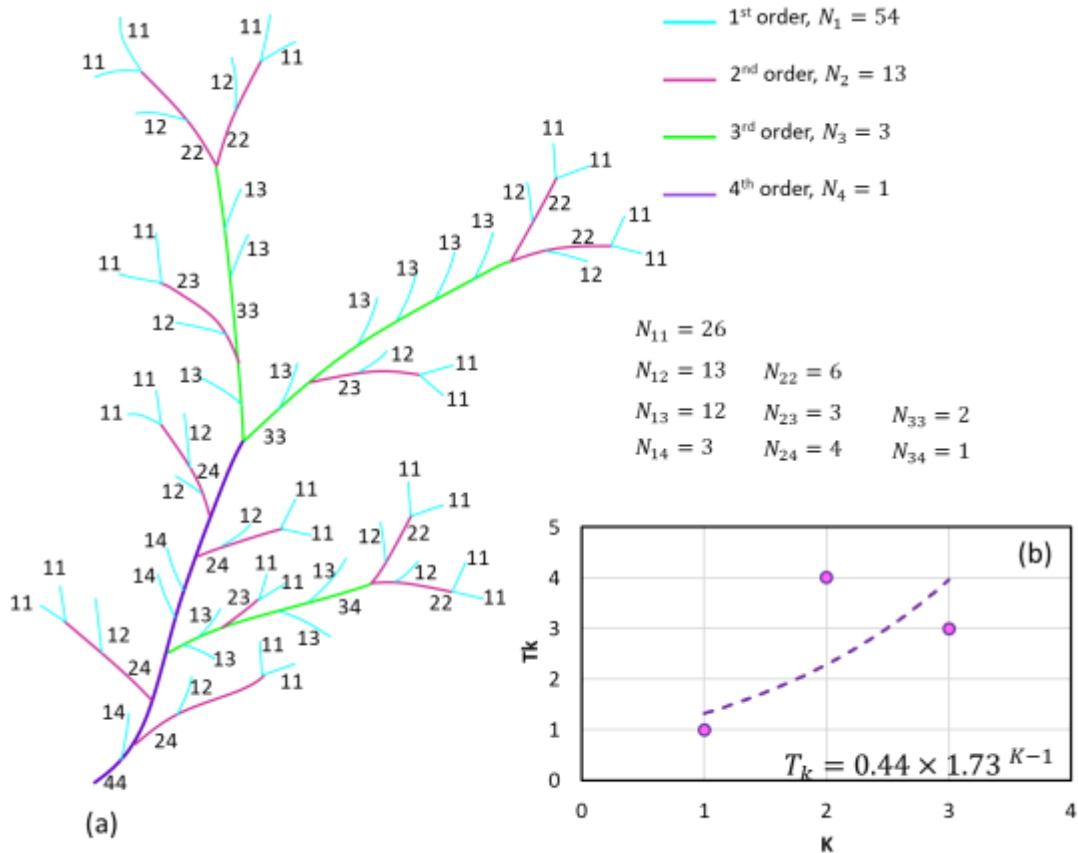
Figure 15. (a) Schematic of a 4th-order channel network. (b) exponential function fitted to K-1 and T_k. This channel network exhibits Tokunaga self-similarity with a c-value of 1.73.

4.3   Results and discussion

Figure 16 shows the CNs, W(x) and IA(x) for two selected catchments for demonstration. These catchments have similar longest channel length (Figure 16(a) and (b)); thus the ranges of x for W(x) (Figure 16(c) and (d)) and IA(x) (Figure 16(e) and (f)) are also similar. The difference in the density of channels along the main channel can be observed from Figure 16(c) and (d). For example, the maximum channel density is at a distance of 1200 m in catchment A and 1600 m in catchment B from the catchment outlet;

however, the number of channels from that peak decreases gradually in catchment A but abruptly in catchment B. The IA(x) for the two catchments are plotted in Figure 16(e) and (f), respectively, showing the difference in the flow accumulation patterns along the main channel. The IA(x) for catchment B contains a higher number of large spikes compared to catchment A, implying that there are more lateral tributaries connected to the main channel in catchment B. For visualization purposes, the insets in Figure 16(e) and (f) show the IA(x) on log-scale, exhibiting significant fluctuations in IA(x).

We use MSE to analyze the characteristics of W(x) and IA(x) signals of CN, which quantifies the complexity in a series and captures the information about emerged patterns in that series at different scales. The emerged patterns in W(x) provide meaningful information about how the density of the channels is distributed in a catchment; whereas, the emerged patterns in IA(x), describes how the environmental fluxes contribute to the main channel through side channels and hillslopes.
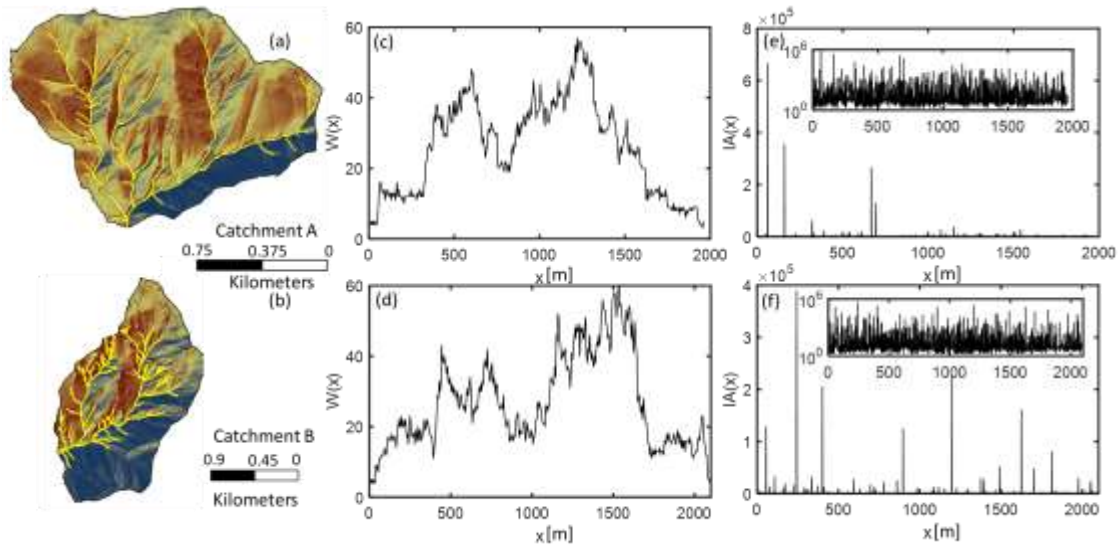
Figure 16. Sample examples of natural catchments, (a) catchment A and (b) catchment B used for complexity analysis with superimposed channel networks. (c) and (d) show the width function W(x) for catchments A and B, respectively. x-axis represents the flow distance from the outlet and 0 on the x-axis represents the outlet. y-axis in these figures represents the number of channels at a certain distance from the catchment outlet. (e) and (f) show the incremental area function IA(x) for the catchments A and B, respectively. Note that IA(x) has been flipped (from right to left) in order to be consistent with W(x). y-axis indicates the incremental change in the contributing area as one moves on the main channel. Insets (e) and (f) show the IA(x) on a log-scale.

In order to investigate the influence of side-branching (i.e., i^{th}-order stream meeting a jth-order stream, where $j > i$) on the structural and functional complexity of CN, we compute the entropy (i.e., MSE) of W(x) and IA(x) for 40 natural catchments at multiple spatial-scales and plot entropy E versus their Tokunaga index, c-value (Figure 17).

Figure 17 shows the relationship between E and the c-value for W(x) and IA(x) at different spatial-scales for 40 catchments. Note that different spatial-scales refer to the coarse-grained W(x) and IA(x) computed using Eq. (2.7) , representing different resolutions of DEM (see schematic representations of catchment B at 2 different spatial-scales as insets in Figure 18(a)). For brevity, we only plot E versus c-value at the scales of 5, 10, and 20 m. As can be seen from Figure 17(a), (b), and (c), the entropy of W(x) increases with the c-value at all the scales. From Figure 17(d), (e), and (f), it can be seen that entropy of IA(x) also increases with the c-value at each scale. The correlations shown in Figure 17 have been evaluated by Pearson's correlation coefficients and the associated P-values (shown inside each figure). Based on *Taylor* [1997] which classifies the correlations as not significant (P-value > 0.05), significant (0.01 < P-value < 0.05) and highly significant (P-value < 0.01), the correlations shown in Figure 17 can be considered as highly significant [*Orlandini et al.*, 2006; *Orlandini et al.*, 2011].

This implies that both structural and functional complexities increase with more complex side-branching in CN across various spatial-scales. Note that higher c-value implies a more complex side-branching arrangement [*Tokunaga*, 1966; *Zanardo et al.*, 2013]. We remind the reader that the structural complexity is referred to the emerged complex patterns in the channel organization and how these patterns are being repeated along the

main channel. Whereas, functional complexity depicts the complexity of flux transport along the main channel. Functional complexity includes channels' and hillslopes' information and describes the flux transport patterns from the side tributaries. The increasing relationship between the c-value and both structural and functional complexity highlights the importance of the role of side-branching in controlling the complexity of channel organization and flux transport on CN. Since the c-value exhibits significant relationship with hydro-climatic parameters and represents the regional controls on the network topology [*Cui et al.*, 1999; *Zanardo et al.*, 2013], our analysis offers the possibility to estimate the behavior of CN in terms of channel reorganization and flux transport under varying external forcing such as climate.

Comparing the values (y-axis) of entropy of W(x) and IA(x), one can conclude that functional complexity of CNs is, in general, larger than structural complexity. The additional complexity which appears in the IA(x) may be due to contribution from hillslopes since the IA(x) includes information from both channels and hillslopes, whereas W(x) includes information only about the channel's structural arrangement. The contribution of hillslopes to the complexity of catchments is invariant with drainage basin size. In other words, a significant relationship is not observed between the complexity due to hillslopes and the drainage basin size. Also, note that the robustness of the complexity analysis was validated for several smaller sub-basins of the original catchments.
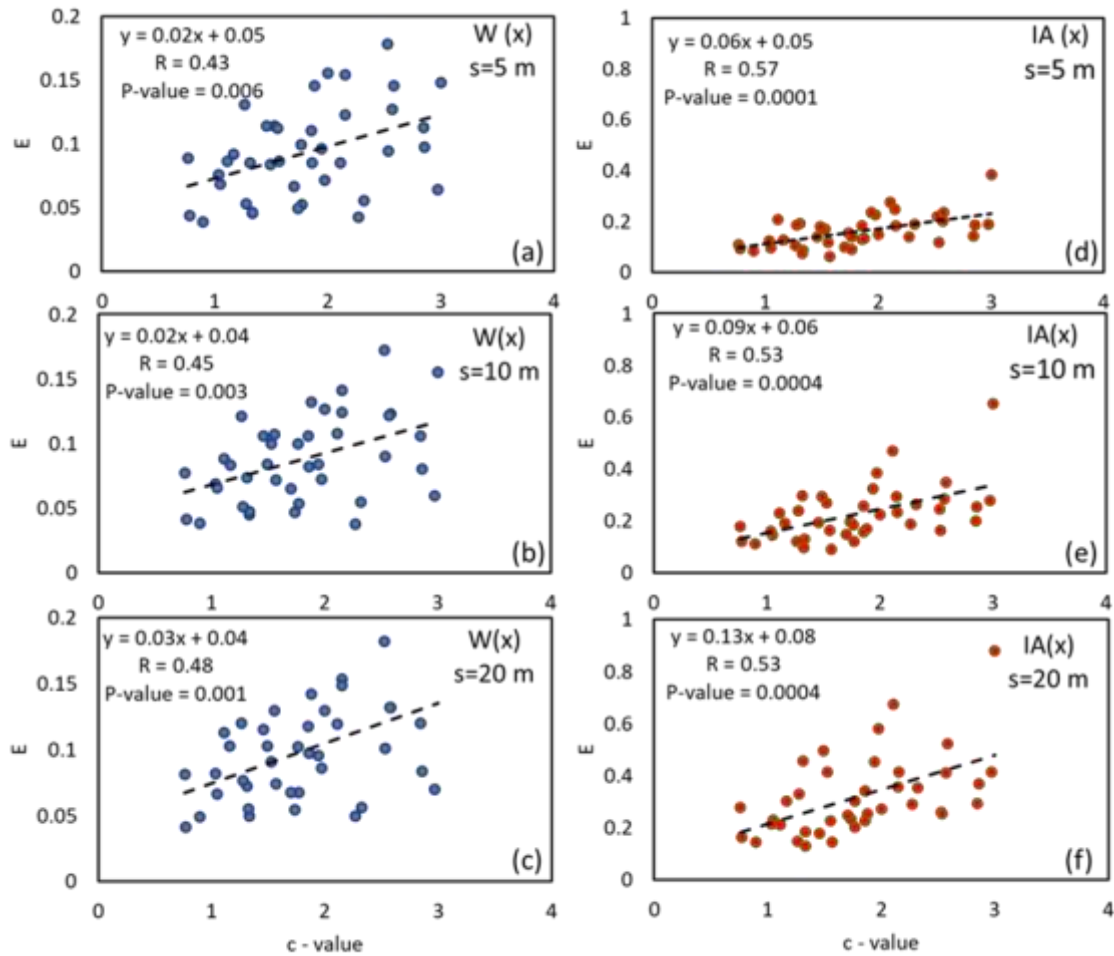
Figure 17. (a), (b), and (c) demonstrate the structural complexity versus c-value; (d), (e), and (f) exhibit the functional complexity versus c-value at spatial-scales of 5, 10, and 20 m, respectively. Structural complexity is computed as the entropy of W(x), whereas functional complexity is computed as the entropy of IA(x). Note that for all the scales the slope of increase is larger for the functional complexity compared to structural complexity (see slopes of linear regressions provided in each subplot).

For any given spatial-scale, the slope of increase in entropy with c-value is smaller in the case of W(x) compared with IA(x) (see slopes of regression lines in Figure 17) indicating that in general, functional complexity is more influenced by complex side-branching patterns

compared to the structural complexity. This observation suggests that catchments with different c-values contain more distinct patterns of flux transport compared with the patterns of channel organization. In other words, topology influences the interaction between hillslopes and channels more than only the channel organization.

Figure 18(a) shows the slope of E versus c-value ($Slope_{E-c}$) as a function of scales obtained from the linear regression for 40 catchments. It can be seen from this figure that there is an increase in $Slope_{E-c}$ with scales for both W(x) and IA(x). As can be seen from this figure, $Slope_{E-c}$ is larger for IA(x) across all spatial-scales compared to W(x). This observation suggests that across multiple spatial-scales, functional complexity increases with c-value much faster compared to structural complexity. In addition, the slope increases logarithmically for IA(x) whereas it increases exponentially for W(x). The difference between the slopes can be attributed to the contribution of hillslopes to the functional complexity.

Based on Figure 18(a) the slope difference between IA(x) and W(x) ($\Delta Slope_{E-c}$) (i.e., the difference between the slopes shown in Figure 17 obtained from 40 catchments for W(x) and IA(x)) is different across different scales. Figure 18(b) shows the $\Delta Slope_{E-c}$ across spatial-scales. It can be seen from this figure that the $\Delta Slope_{E-c}$ generally increases with scales and peaks at a scale of ~ 45 m. This implies that the effect of hillslope processes is overall higher in larger spatial-scales. The additional entropic content observed by $\Delta Slope_{E-c}$ further indicates that predictive models of hydrological processes at the watershed scale must account for hillslope-scale complexity [*Sivapalan*, 2003].

To compare the studied catchments' hillslope processes magnitude, we computed their diffusion coefficient D, which characterizes hillslope processes, using a method proposed by *Perron et al.* [2008]. The inset in Figure 18(b) shows the relationship between D and c-value for our studied catchments where an increasing trend is observed. Although the correlation is not very high (R=0.32), further statistical analysis shows that the correlation is significant within 95 percent confidence-interval (P-value<0.05). As can be seen from the inset, the magnitude of diffusive processes (hillslopes) is larger in the catchments with more complex side-branching behavior (i.e., higher c-value), indicating the increase in hillslope effect with c-value, further manifesting itself in functional complexity across multiple spatial-scales.

In addition, the peak in $\Delta Slope_{E-c}$, occurring at a spatial-scale of ~ 45 m, suggests the scale where the influence of hillslopes on the complexity is maximum. This peak can be attributed to the hillslope length (L_H) in natural catchments. *Horton* [1932] introduced the hillslope length parameter as the average distance that water must travel from a random point in a catchment to reach a channel (see also *Tucker et al.* [2001]). This parameter is also referred to as overland flow length and is of great hydrological importance due to its relation to flood intensities. It has been shown that the hillslope length has an inverse relationship with D_d, i.e., $L_H \approx (2D_d)^{-1}$.

Figure 18(c) shows the elevation profile of catchment B (inset) for four random channels on its CN. The red channel is of the maximum channel length (i.e., the main channel). Note that the W(x) and IA(x) have been computed along this channel for this catchment. The hillslope length computed for a catchment can be related to the average

distance from all channel heads in a CN to the drainage divide (shown with dotted black lines extending the CN, as examples) as the hillslopes vary in shapes, sizes and the underlying subsurface heterogeneities [*Grieve et al.*, 2016; *Sivapalan*, 2003].

The average hillslope length computed for 40 natural catchments used in this study is 56.5m. This observation further confirms the increase in entropy at the scale ~ 45m independently identified via entropy analysis (see Figure 18(b)) and suggests that indeed hillslopes contribute to higher complexity in a catchment. Hillslopes initiate tributaries on lateral slopes of the main channel [*Horton*, 1932] and the average length of them controls the spatial-scale at which the difference between the rate of increase of functional and structural complexity with topology (c-value) is maximum. This may imply that hillslopes introduce a significant amount of complexity to catchment compared to the complexity introduced only by the CN.
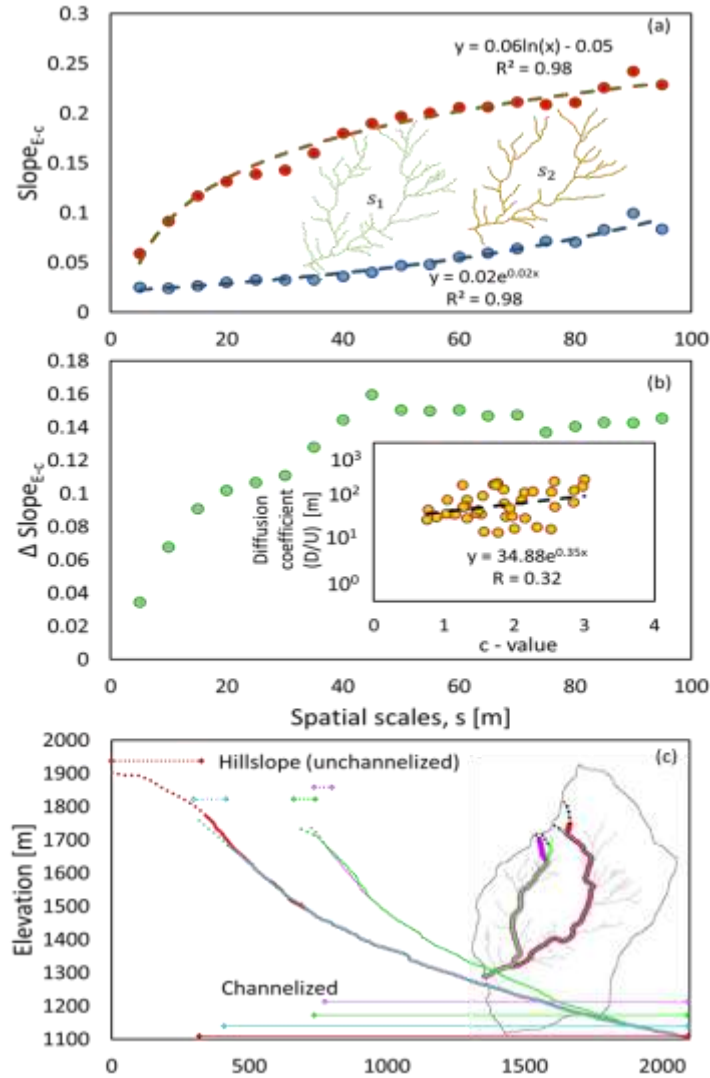
Figure 18. (a) Slope of entropy (E) versus Tokunaga index (c-value) across spatial-scales for both W(x) (blue circles) and IA(x) (red circles). The insets in (a) show the schematic representations of catchment B at scales s_1 and s_2, where $s_1 < s_2$. (b) The difference between slope obtained from W(x) and IA(x). The inset shows the diffusion coefficient (*D*) versus c-value for 40 natural catchments. (c) Elevation profiles along four channels of catchment B from drainage divide to the outlet. The inset shows catchment B with superimposed channel network. These channel profiles are extended to the drainage divide by dotted black lines to represent hillslope length.

CHAPTER 5:   COMPLEXITY OF RIVER BED ELEVATION

FLUCTUATIONS

Bedforms evolve spatially and temporally as a result of a complex interaction between the turbulent flow field, sediment transport, and fluvial bed topography, and vary with local bed shear stress and grain size distribution. They have been shown to exhibit scale-dependent geometrical and statistical properties. Investigating their spatial characteristics and evolution is important for river management and interpreting past sedimentary strata, as well as for predictive modeling of sediment transport rates [*Best*, 2005; *Drake et al.*, 1988; *McElroy and Mohrig*, 2009; *Nelson et al.*, 1993; *Nikora and Walsh*, 2004; *Nikora et al.*, 2002].

Several studies have focused on investigating the statistical structure of bedforms at multiple spatio-temporal scales. However, factors resulting in specific sequential arrangement in bed elevation patterns are not fully understood. Identifying the existing patterns in the bed elevation fluctuations under varying flux conditions can provide significant information for predicting the behavior of rivers under changing environment. The fluctuations of bed elevations have been studied via correlation functions, or second-order structure functions which characterize the second-order moments. However, the probability density function (PDF) of these fluctuations has been shown to exhibit a scale-dependent shape [*Marion et al.*, 2003; *Smart et al.*, 2004]. To account for the change of PDF across scales, *Nikora and Walsh* [2004] suggested to use higher-order statistics to analyze

the characteristics of bed elevations in water-worked gravel surfaces and demonstrated that the topography of gravel surfaces exhibits multiscale behavior which is sensitive to the flow direction. *A Singh et al.* [2009b] analyzed the multiscale statistical structure of highly variable bed elevation time series and documented scaling behavior and intermittency and their relation with simultaneously sampled sediment flux.

One way to characterize the variability of fluctuations for a natural process is via entropy. *Shannon* [1948] defined entropy as a measure of variability, uncertainty, and complexity. The concept of entropy has been used in various fields of science and engineering including hydrology and geomorphology, such as basin geomorphology, water distribution systems, surface and subsurface hydrology, and water quality assessment [*Fiorentino et al.*, 1993; *Goodwell and Kumar*, 2017; *Leopold and Langbein*, 1962; *Pincus*, 1991; *V P Singh*, 1997; *Tejedor et al.*, 2017b]. For example, *Mishra et al.* [2009] employed an entropy-based approach to investigate the spatio-temporal variability of monthly, seasonal, and annual time series of precipitation for the State of Texas, USA, and observed distinct spatial patterns in annual series and different seasons. Their results show that high disorderliness in the amount of precipitation and number

of rainy days caused severe droughts during the 1950's in Texas. More recently, *Chembolu and Dutta* [2016] analyzed the relationship between entropy and energy dissipated in braided river systems. They showed that a 4-year return period flood results in disorderness in the river planform and increases the entropy. *Wrzesiński* [2016] proposed uncertainty measures derived from the Shannon entropy to characterize the river runoff regime. However, Shannon entropy is solely based on the PDF of a series and does not

consider the arrangement or the sequence of the data points in a series. These above-mentioned studies use the Shannon entropy which is a classical probabilistic approach analyzing the randomness of the generating process of a series and not the randomness of a series itself. In other words, Shannon entropy is a metric to study the process of the data, and the order of the generated data does not have any influence on this metric [*Chaitin*, 1975; *Delgado-Bonal and Marshak*, 2019].

In this chapter, we are interested in understanding and quantifying the underlying dynamics of the bed elevation series for varying flow conditions. We study the complexity of rivers from a different point of view and a much smaller scale i.e. bed elevation fluctuations using an entropy-based approach.

5.1   Description of experiments

The experiments presented here were conducted in the Main Channel facility at the St. Anthony Falls Laboratory, University of Minnesota. The data reported consist of time series of bed elevation fluctuations which were collected along the center-line at three different discharges of Q = 1500 L/s, Q = 2600 L/s, and Q = 2800 L/s corresponding to the dimensionless bed shear stresses of 0.049, 0.080, and 0.099, respectively. In addition, we use data of bed elevation collected at a lower discharge, i.e. 600 L/s, in the same flume for comparison purposes [*Keylock et al.*, 2014]. The bed for this discharge was a planar bed compared to the other three discharges.

The main channel was 84 m long, however, the section used was 55 m long, 2.75 m wide, and 1.8 m deep. The channel was filled with a 0.45 m thick layer of sediment. For the

sediment, a mixture of gravel and sand with a median particle size diameter $d_{50}=7.7$ mm was used. The overall grain size distribution was characterized by $d_{16}=2.2$ mm and $d_{84}=21.2$ mm. To achieve dynamic equilibrium in transport and slope adjustment for both water surface and sediment bed, a constant water discharge was fed into the channel prior to the data collection. This dynamic equilibrium state was evaluated by checking the stability of the 60 min average total sediment flux at the downstream end of the test section. Although experiments were run for longer duration (~20 hrs), here we use continuous bed elevation data corresponding to ~ 6 hrs to maintain similar length of bed elevation time series at each analyzed discharge.

The bed elevation data presented here were sampled at point location with a temporal resolution of 5 sec at the downstream end of the flume. This high temporal resolution enabled us to capture a range of bedform scales. Bedform heights were extracted based on the method described in [*A Singh et al.*, 2011]. In this method, first, the high-frequency fluctuations corresponding to the very small bedforms were filtered out from the bed elevation using the Fourier transform. Second, the differences between the consecutive local maxima and minima of the filtered signal were computed. Finally, the bedforms with a height above a certain threshold (i.e. 2 d_{50}) were extracted for each discharge. Note that the bedforms' statistics here, at different discharges, were extracted for the same length of time series. More details about the experimental facility and the data collection can be found in [*A Singh et al.*, 2012a; *A Singh et al.*, 2009b; *A Singh et al.*, 2013].

5.2   Surrogate generation

Surrogates are the linearized representations of the original data. They preserve the linear autocorrelative properties of the data while destroying the inherent nonlinearity. Inherent nonlinearity implies nonlinearity resulting from internal processes. In other words, for an inherent nonlinear process, the nonlinearity is not a result of nonlinear transformation applied to a linear process, but it is related to its dynamics. The nonlinearity appeared as a result of multiplicative cascade generator in the popular phenomenological model used for turbulence is an example of inherent nonlinearity [*Parisi and Frisch*, 1985]. Since nonlinearity is the necessity of chaos, it is important to identify whether a time series is generated by a linear or inherently nonlinear process. Surrogates are used to test for the presence of nonlinearity by comparing the original series with them. The Iterated, Amplitude Adjusted, Fourier Transform (IAAFT) method was developed by [*Schreiber and Schmitz*, 1996] to generate surrogates of a signal and has been applied to characterize various environmental processes [*Basu et al.*, 2007; *Keylock*, 2012; *A Singh et al.*, 2009a]. In this method, first the Fourier transform of the discretely sampled data series (here bed elevation time series), $h(t)$, with a sampling interval of Δ_t is computed as:

$$\hat{F}(\omega) = \sum_{n=1}^{N} h(t) \exp[2\pi i \omega \Delta_t] = A_0(\omega) \exp[i\varphi_0(\omega)] \qquad (5.1)$$

where $A_0(\omega)$ are the original amplitudes which are stored and $\varphi_0(\omega)$ are the original phases that are replaced with $\varphi_{rand}(\omega)$ which are the phases from a random sort of data. Second, the inverse Fourier transform is taken and a rank-order matching procedure is used to substitute the new values for original values in $h(t)$ to obtain $h_1(t)$. Therefore, $h(t)$ and

$h_1(t)$ are similar in terms of their histograms. The difference between them is only the position of particular values in the data series which is changed due to the phase randomization. Taking the Fourier transform of $h_1(t)$, $A_1(\omega)\exp[i\varphi_1(\omega)]$ is obtained. We take the inverse Fourier transform of $A_0(\omega)\exp[i\varphi_0(\omega)]$ and impose the rank-order matching to compute the $h_1(t)$. Mentioned steps are iterated until a convergence criterion is satisfied (at the ith iteration), with the amplitudes in $A_0(\omega)$ combined with $\varphi_i(\omega)$, the inverse Fourier transform and rank-order matching that gives $h_i(t)$. For more details, see *Keylock et al.* [2014]; *Schreiber and Schmitz* [1996]; *A Singh et al.* [2009a].

5.3   Structure function analysis

In order to analyze the multiscale structure of the bed elevation series $h(t)$, the bed elevation increments are used and can be defined as:

$$\Delta h(t,s) = h(t+s) - h(t) \tag{5.2}$$

where t is the time and s is the scale. Note that although $h(t)$ is always positive, the increments $h(t,s)$ can acquire both negative and positive values. The structure function $M(q,s)$ is defined as the estimates of the qth-order statistical moments of the absolute values of the increments at scale s:

$$M(q,s) = \frac{1}{k}\sum_{i=1}^{k}|\Delta h(t,s)|^q \tag{5.3}$$

where k represents the number of data points of the series at scale s. The statistical moments $M(q,s)$ describe the shape of the PDF of the increments of the bed elevation series at scale s. $M(q,s)$ follows a power-law relationship with the scales,

$$M(q,s) \sim s^{\zeta(q)} \tag{5.4}$$

where $\zeta(q)$ is the scaling exponent function. In a scale-invariant series, the variations of the increments' PDF with scales are delimited by the function $\zeta(q)$. For most processes, the nonlinear relationship describing $\zeta(q)$ can be characterized as a polynomial quadratic approximation as:

$$\zeta(q) = c_1 q - \frac{c_2}{2} q^2 \tag{5.5}$$

Thus, the variations of the PDF over a range of scales are characterized using c_1 and c_2. c_1 represents the average roughness of the series and c_2 is the intermittency parameter. A non-zero value of c_2 implies that across different scales, the tails of the PDF stretch in a way different from the body. In other words, pockets of high magnitude fluctuations are distributed over the signal's domain in complicated ways. More details about the structure function analysis can be found in *Parisi and Frisch* [1985] and *Marion et al.* [2003]. Also, note that for $c_2 = 0$, c_1 represents the Hurst exponent (H) which characterizes the degree of linear correlation within a signal, and can be related to the spectral slope (β) of the power spectral density as $\beta = 2H + 1$ [*A Singh et al.*, 2012b].

5.4   Results and discussion

As discussed above, river bed topography exhibits variability across a range of scales. The power spectral density (PSD) is a common way of characterizing variability of a signal (energy distribution or variance) at different scales and shows the strong and weak scales contributing to the signal variance. The PSD of a discrete signal $h(t)$ can be defined as:

$$s(\omega) = \left| \frac{1}{\sqrt{2\pi}} \sum_{-\infty}^{\infty} h(t) exp[-i\omega t] \right|^2 = \frac{\widehat{H}(\omega)\widehat{H}^*(\omega)}{2\pi} \qquad (5.6)$$

where $\widehat{H}(\omega)$ represents the discrete Fourier transform of $h(t)$, $\widehat{H}^*(\omega)$ is the complex conjugate and ω is the wave number [*Stoica and Moses*, 1997].

Here, temporal bed elevation fluctuations for three different discharges are analyzed using the PSD. Note that the temporal bed elevation data are more likely to exhibit complexity compared to spatial data series. This is because the nonlinearity in temporal data series appears at much smaller scales due to accumulation of large scale features (bedforms), depending on the length of temporal duration, as opposed to available spatial series for these experiments where only a few large scale features (bedforms) are present. More specifically, the gradual rise and sudden fall (i.e. ramp and cliff features or stoss and lee sides of dunes or ripples) are more dominant in temporal series than in spatial series. In order to be able to characterize the complexity in spatial data series, one needs sufficiently long data series, which is not practical to obtain in terms of experimental setups. In summary, if spatial data are used, only as many bedforms as fit in the experimental domain can be obtained, whereas in the case of temporal data, from one location one can keep collecting data until required bedforms needed for a robust statistical analysis pass through that measurement location.

Figure 19 shows the bed elevation data collected for three different discharges of 1500, 2600, and 2800 L/s. As can be seen visually, the variability in bed elevation fluctuations increases with increasing discharge. Figure 20 shows the PSD of the bed elevation series for the discharges of 1500, 2600, and 2800 L/s as a function of time scales.

The PSD for all cases follow a power-law relationship for a range of scales (~0.22 min to 6.7 min) with a slope of β 1.83 for the discharge of 1500 L/s, $\beta \sim 2.21$ for the discharge of 2600 L/s and $\beta \sim 2.29$ for the discharge of 2800 L/s, suggesting the presence of statistical scaling in the bed elevation time series. The estimated spectral slopes are statistically different based on the t-test hypothesis testing (p-value < 0.00001).

The increase in the slope of the PSD with increasing discharge has been argued to imply that bedforms of comparable energy move faster at higher discharges [*A Singh et al.*, 2012b]. Also, note that the higher spectral slope at higher discharge indicates a higher auto-correlation in bed elevation of $Q = 2800$ L/s. The PSD characterizes the behavior of variance (second-order moment) at different time scales. Variance quantifies the aggregated variability or the spread in observations (data) around the mean and does not consider or give any information about the dispersion (the magnitude of probabilistic strength assigned to each fluctuation) in the fluctuations of a signal. Unlike variance which measures the concentration only around the mean, entropy measures dispersion and quantifies the diffuseness of the PDF without considering the location of the concentration [*Ebrahimi et al.*, 1999].
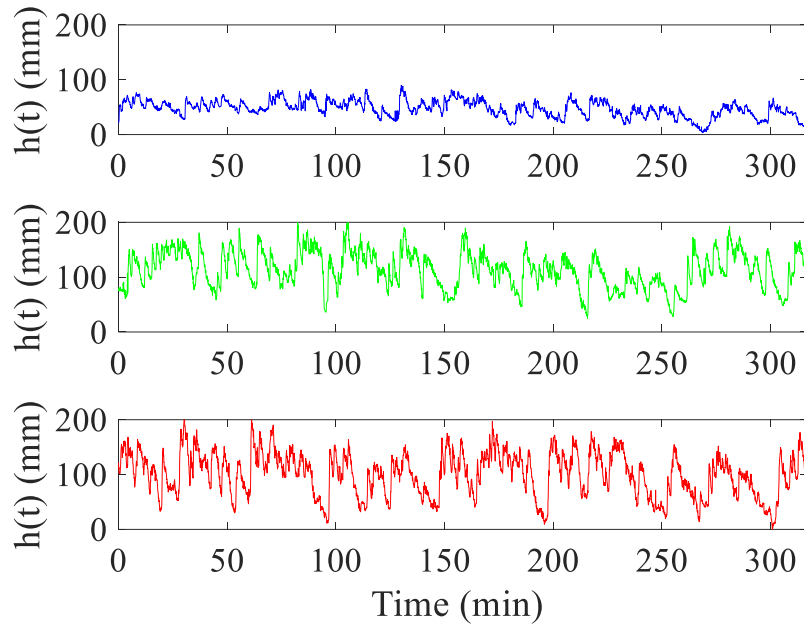
Figure 19. Time series of bed elevation at the discharges of (a) 1500 L/s, (b) 2600 L/s, and (c) 2800 L/s. The bed elevation data were sampled at a temporal resolution of 5 sec. Notice the increase in variability with increasing discharge.
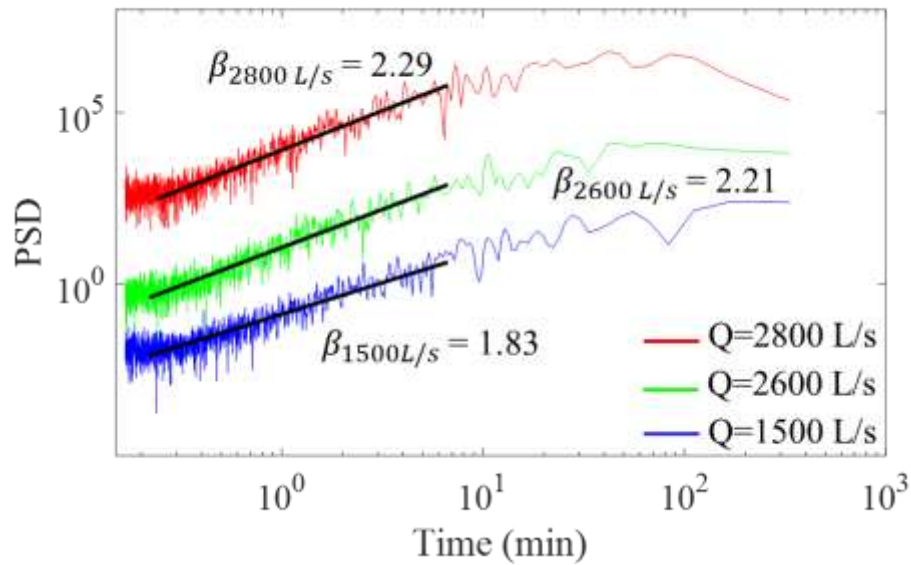
Figure 20. Power spectral density (PSD) of bed elevation for the discharges of 1500 L/s (blue line), 2600 L/s (green line), and 2800 L/s (red line). PSDs of discharges for 1500 L/s and 2800 L/s are displaced vertically for better visualization by multiplying their PSD values by 5×10^{-2} and 5×10^{2}, respectively.

In order to compare the complexity of bed elevation time series for the three different discharges, we used the MSE approach. Figure 21(a) shows the MSE of bed elevation series for the discharges of 1500, 2600, and 2800 L/s. The x-axis represents the scales which show the length of the coarse-graining windows. For example, the scale of 6 min represents a time series with data points corresponding to the average of 6 min non-overlapping windows from the original time series (i.e. 72 data points from the original time series with 5 sec sampling interval).
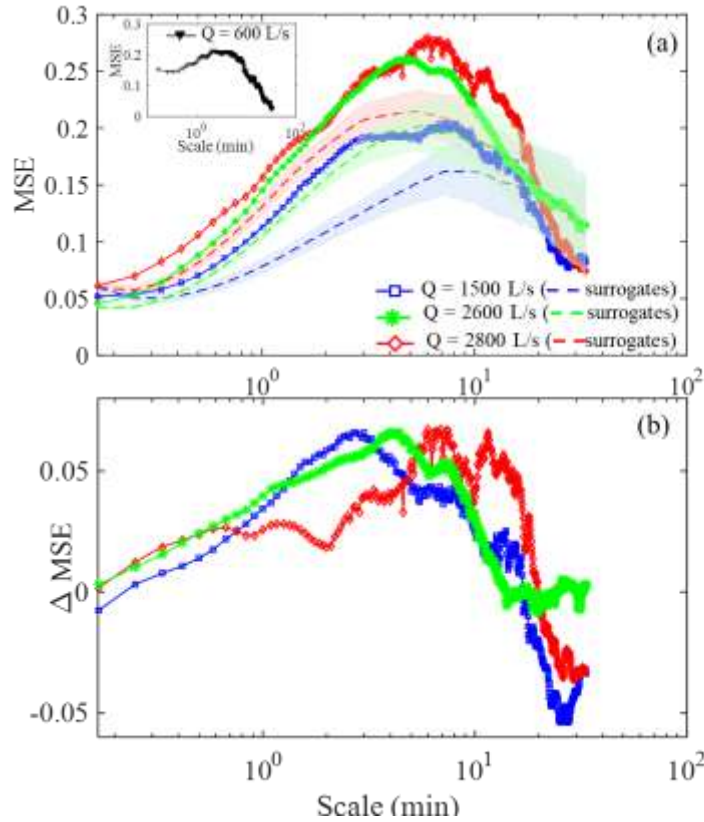
Figure 21. Multiscale entropy (MSE) of bed elevation for different discharges. The blue, green, and red solid lines show the MSE of bed elevation time series for the discharges of 1500 L/s, 2600, and 2800 L/s, respectively. The blue, green, and red dashed lines show the averaged MSE for the synthetically generated surrogates of bed elevation time series for the discharges of 1500 L/s, 2600 L/s, and 2800 L/s, respectively. The average MSEs of surrogates were computed from 50 surrogates for each discharge. The surrogates were generated using the IAAFT algorithm. The shaded area around the dashed lines depicts the variability around the average MSE of surrogates (one standard deviation). The inset shows the MSE of bed elevation for the discharge of 600 L/s for comparison purposes. (b) Difference between the MSE of the original bed elevation time series and the surrogates for each discharge.

From the results shown in Figure 21(a), the following observations can be made:

1. The MSEs of bed elevation for the discharges of 1500, 2600, and 2800 L/s do not follow the same behavior across different scales. This observation suggests the presence of different sequential arrangement in bedform patterns across a range of scales. The MSEs of higher discharges (2600 and 2800 L/s) are higher than the MSE of lower discharge (1500 L/s) at almost all scales. Higher MSE represents higher complexity and thus less predictability. Our results show that the bed elevation (and thus related processes, e.g. erosion and deposition) at higher discharges are less predictable than the bed elevation at lower discharge. It has been shown that the complexity has an inverse relationship with vulnerability. *Tejedor et al.* [2015] investigated the quantitative relationship between an entropy based complexity measure and vulnerability and suggested that a more complex system is more robust to a change. Higher complexity in the bedforms at higher discharges implies that channel beds with higher discharges and their characteristics are less vulnerable to changes in external forcings.

The increase in entropy with increasing discharge can be due to bedforms' spatial (bedform heights) and temporal (bedform time period) characteristics. Figure 22 shows the extracted bedforms at different discharges used in this study. From this figure, it can be seen that bedform height increases with increasing discharge. The average bedform height for the discharges of 1500, 2600 and 2800 L/s is 29.9, 51.3 and 68.9 mm, respectively. In addition, the variability of bedform heights (measured by standard deviation) also increases with discharge (Table 6) resulting in complex patterns for the bed elevations at higher discharges.
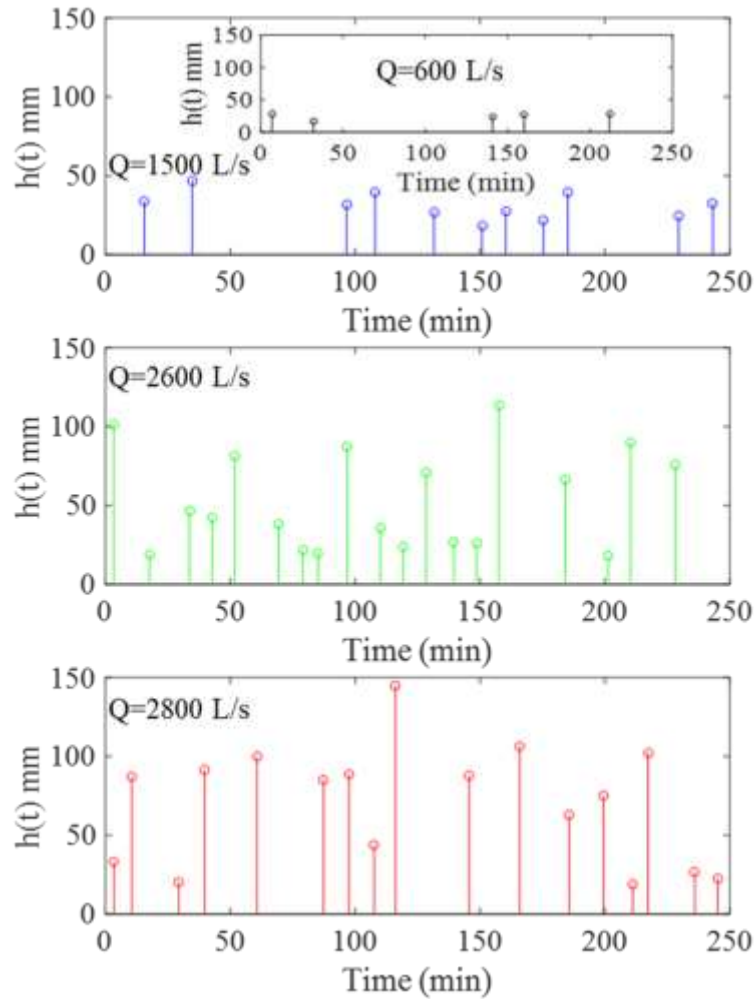
Figure 22. (a), (b) and (c) Extracted bedform heights above a certain threshold for the discharges of 1500, 2600, and 2800 L/s, respectively. The inset in (a) shows the extracted bedforms for the discharge of 600 L/s.

Table 6. Hydraulic and statistical properties of bed elevation time series. D : average flow depth, S_w: water surface slope, h_R : hydraulic radius, τ^*_b: dimensionless shield stress, $t_{h_{bf}}$: average bedform height, $std_{h_{bf}}$: standard-deviation of bedform heights, $t_{h_{bf}}$: mean bedform inter-arrival time $\pm$ one standard-deviation, β: spectral slope, c_2: intermittency. Note that the bedform statistics are computed for the same length (~ 6 hrs) of bed elevation time series for different discharges.

Q [L/s]	D [m]	S_w	h_R [m]	τ^*_b	h_{bf} [mm]	$std_{(hbf)}$ [mm]	t_{hbf} [min]	β	c_2
600	0.21	0.005	0.18	0.085	24.8	4.7	51.2 ± 40.8	1.31	0.05
1500	0.43	0.00195	0.33	0.049	29.9	9.1	24 ± 16.7	1.83	0.09
2600	0.62	0.0024	0.43	0.08	51.3	29.3	12.8 ± 4.2	2.21	0.12
2800	0.64	0.0029	0.44	0.099	68.9	36.4	14.8 ± 6.8	2.29	0.14

2. At the smaller time scales (scales $\geq$ 0.3 min), the bed elevation for all discharges have similar MSEs indicating that the ratio of total number of matches for smaller patterns (n_m) and larger patterns (n_{m+1}) are almost equivalent at all discharges (see Eq. ((2.1)). This observation indicates that the information revealed by the three sets of bed elevation series is not clearly distinguishable at the smaller scales since the same entropy is obtained for them implying the presence of similar patterns in the bed elevations of different discharges.

Note that in this case, if large and small patterns are not similarly repeated (i.e. random structure as in white noise) a higher entropy would be observed at smaller scales. This can be seen from the MSE of bed elevations for Q = 600 L/s (see the inset in Figure 21(a)) which exhibits more random bed elevation fluctuations similar to white noise and the

bedforms are considerably smaller compared to other discharges. For example, the average bedform height for 600 L/s is 24.8 mm. Furthermore, based on the entropy at smaller scales, it is difficult to infer whether the bed elevations at 600 L/s are more complex than other discharges since smaller scales may not always reflect the amount of complexity due to the presence of random fluctuations. In contrast, for sufficiently larger (intermediate) time scales, a lower entropy value is obtained for the 600 L/s suggesting that bed elevation at 600 L/s contain less complex dynamics compared with higher discharges. This is consistent with the behavior shown by the MSE of white noise.

3. The entropy of the bed elevation for higher discharges continues to increase and peak at a scale of approximately 5-7 min, similar to the half of the mean inter-arrival time of bedforms (see Table 6). The peak observed at the scale smaller than the mean inter-arrival time could be due to bedform features, such as stoss and lee features, as they result in transition in the bedform profile. However, the entropy of the bed elevation for lower discharge attains almost a constant value across the time scales between 3 and 6 min. This observation indicates that the bed elevation of higher discharges, in comparison to the lower discharge, continues to reveal different structural arrangement from scales 3 to 6 min, whereas the bed elevation of lower discharge reveals the same amount of information (change in the arrangement of the elevations) from scale 3 to 6 min.

4. Although for scales < 6 min the bed elevation series at higher and lower discharges exhibit an increasing trend of MSE in general (except for 3 to 6 min for Q = 1500 L/s), the overall slope of this increase is different. A higher rate of increase is observed for the bed elevation of higher discharges compared to the bed elevation of lower discharge for the same

time scale (between the time scales of 5 sec to 8 min), implying that the rate of addition of complexity (information) to these scales is higher for higher discharges compared to the lower discharge.

In order to further investigate the causes of the emergence and increase in complexity across different scales, several different measures (e.g. surrogate time series, structure functions, and asymmetry) are computed. The surrogates of bed elevation series for higher and lower discharges were generated using the IAAFT method (see section 5.2). Figure 21(a) shows that the MSEs of the surrogates, which represent the MSEs of original bed elevation resulting only from linear correlation, are smaller than the original bed elevation series for different discharges. We argue that the difference between the MSEs of the surrogates and the original time series (shown in Figure 21(b)) is the amount of complexity resulting from the inherent nonlinearity. This is due to the fact that the correlation structure (auto-correlation) of the bed elevation time series does not have any contribution to this share (nonlinearity) of complexity since the effect of correlation is isolated by removing the entropy content of the surrogate time series.

As can be seen from Figure 21 the MSE of surrogates is much larger than the difference between surrogates and the original bed elevation. This suggests that a significant portion of the complexity in bed elevation series is due to the correlation structure (auto-correlations) in the time series since the complexity of the surrogates is only due to the linear correlation. Note that the MSEs of the surrogates are smaller than the original bed elevation series for different discharges. Also, the surrogates of bed elevation at higher discharges (also exhibiting higher spectral slope; see Figure 20) show higher complexity compared to

the lower discharge. This is consistent with observations of *Costa et al.* [2002; 2005] where they have shown that the pink noise with higher spectral slope contains higher complexity.

From Figure 21(b), it can be concluded that for scales < 0.8 min, the effect of nonlinearity on the complexity of the bed elevation is more significant for the higher discharge. At scales > 0.8 min, the effect of nonlinearity increases considerably for the lower discharge until scales of ∼ 3 min.

In order to understand the role of nonlinearity in inducing the complexity in bed elevation time series, their increments (Eq. (5.6)) were analyzed using the structure function analysis discussed in section5.3. This analysis evaluates the manner in which various statistical moments of the local fluctuations in the bed elevation time series change with scales. The scaling exponents $\zeta(q)$ for moments $M(q, s)$ are shown in Figure 23 for different discharges and their surrogates. For the original bed elevation time series, a deviation from the simple scaling is observed for all discharges, implying the presence of temporal heterogeneity in the local roughness which is referred to as intermittency in the bed fluctuations [*A Singh et al.*, 2009b]. In the case of surrogates, Figure 23(b), (d), and (f), a significant deviation from the linearity is not observed, indicating and confirming that the nonlinearity in the surrogate bed elevation series is destroyed.

A value of $c_2 \neq 0$ implies a spatially heterogeneous arrangement of fluctuations in the bed elevation time series.
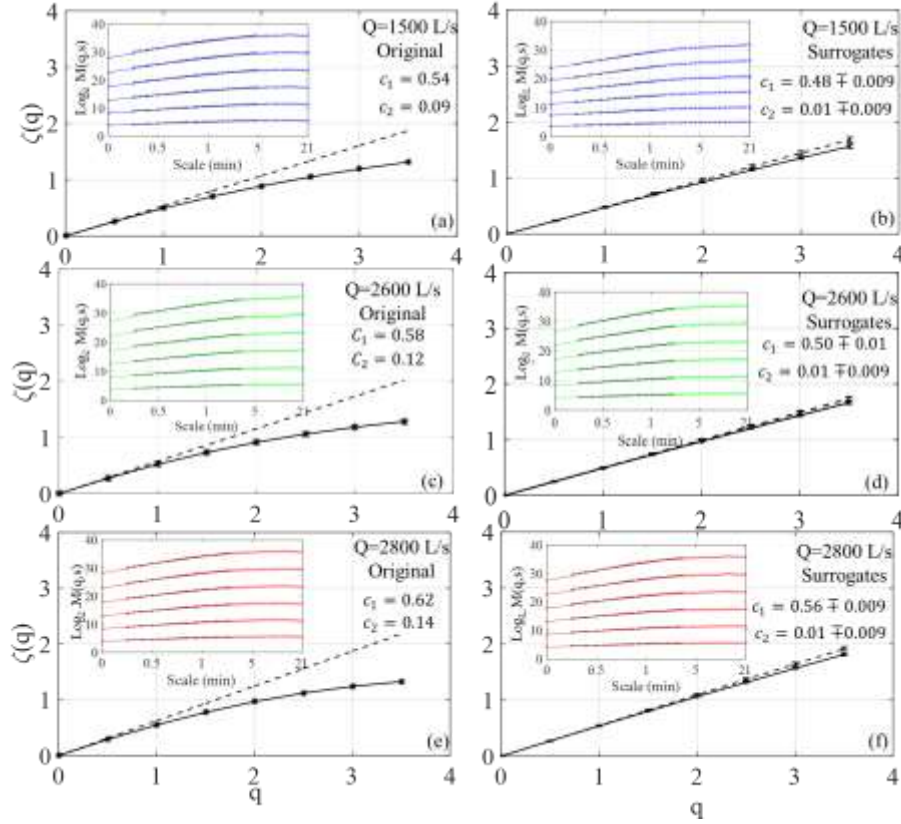
Figure 23. Scaling exponents $\zeta(q)$ estimated from the log-log linear regressions within the scaling regions shown with black lines in the insets of each plot for (a) bed elevations series of discharge 1500 L/s, (b) the surrogates of bed elevations series for discharge 1500 L/s, (c) bed elevations series of discharge 2600 L/s, (d) the surrogates of bed elevations series for discharge 2600 L/s, (e) bed elevations series of discharge 2800 L/s, and (f) the surrogates of bed elevations series for discharge 2800 L/s. The curves in the insets show the statistical moments of the fluctuations of bed elevation time series as a function of scale. In particular, different curves in the insets represent the log of $M(q, s)$ computed using Eq. 5.3 for a given q across different scales. As shown in (a), (c), and (e), the c_2 value increases with increasing discharge indicating a more heterogeneous bed elevation fluctuation structure compared to the lower discharge. The $\zeta(q)$ of the surrogates for different discharges shown in (b), (d), and (f) is the mean $\zeta(q)$ computed for 50 surrogate series. The average c_1 and c_2 values and their standard deviations are also presented in the sub-figures.

From Figure 23(a), (c) and (e) it can be seen that c_2 increases with increasing discharge indicating that the bed elevation with higher discharges contains more heterogeneous fluctuation structures (measured via c_2) compared to the bed elevation of lower discharge. This inhomogeneity manifests itself in the MSE of bed elevation time series where the arrangement of the extreme fluctuations contributes to the increase in the complexity of the series.

Bed elevation fluctuations have also been shown to exhibit asymmetric PDFs especially in the presence of bedforms [*Aberle and Nikora*, 2006; *A Singh et al.*, 2012a; *Wong and Parker*, 2006].

To further explore the effect of asymmetry in the PDFs of bed elevation increments on the emergent complexity of bed elevation time series, we computed the asymmetry of bed elevation increments (Eq(5.2)) expressed as:

$$A(s) = \frac{\langle \Delta h(t,s)^3 \rangle}{\langle |\Delta h(t,s)^3| \rangle} \tag{5.7}$$

where the angled brackets are a mean value and $A(s)$ denotes the asymmetry index as a function of scale s [*Basu et al.*, 2007; *Malecot et al.*, 2000]. Figure 24 shows the asymmetry index for the increments of the bed elevation and their surrogates. As can be seen from this figure, at the smaller scales, the asymmetry of bed elevation has a higher value compared to the larger scales in contrast to the complexity shown in Figure 21(a) where MSE peaks at intermediate scales. This indicates a lack of a direct relationship between the asymmetry and MSE of the bed elevation time series. This is related to the fact that MSE is based on the

sequential arrangement of the data points in a series and aggregated changes in the PDF are not captured by the MSE. In addition, it can be seen from Figure 24 that i) asymmetry peaks at a smaller scale for the higher discharges (scale $\sim$ 0.3 min) than for the lower discharge (asymmetry peaks at scale $\sim$ 1 min), and ii) asymmetry is larger for higher discharge at scales smaller than 0.9 min suggesting more asymmetric PDF at higher discharge. The increase and then decrease of asymmetry at smaller scales (approximately < 1.2 min) for different discharges need further investigation and will be the focus of a future study. We argue that the higher asymmetry at smaller time scales and higher entropy at larger time scales correspond to bedform time scales. Bedform time scale refers to the average time scale at which a characteristic scale bedform passes a channel cross-section. This suggests that there might be a lagged relationship between the asymmetry and MSE. The high asymmetry at smaller time scales is the manifestation of larger slopes (increments) from the ramp-cliff (stoss-lee) structures at smaller scales (i.e. the small fluctuation in bed elevation time series. At larger scales, these slopes are smoothed out. However, in the case of MSE, the peak is observed at bedform scales. The results of asymmetry together with entropy analyses suggest that both small and large scale features (information) should be included for accurate predictive modeling of sediment transport.
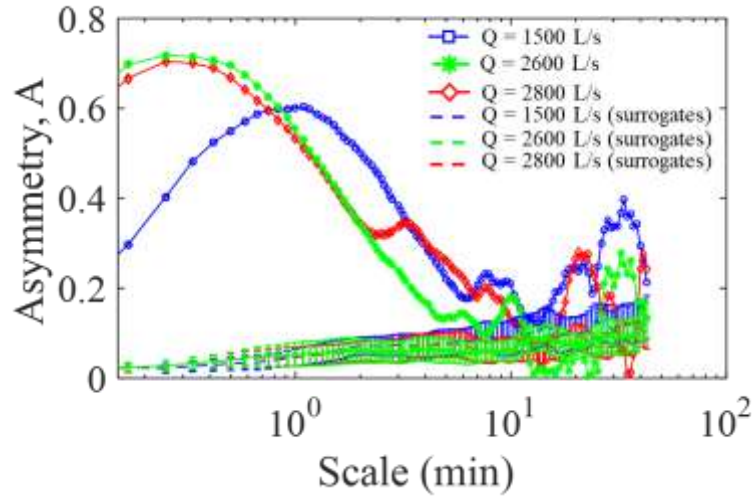
Figure 24. Asymmetry (*A*) of bed elevation increments and their surrogates for different discharges. The blue, green, and red solid lines show the asymmetry of bed elevation time series for the discharges of 1500 L/s, 2600 L/s, and 2800 L/s, respectively. The blue, green, and red dashed lines show the average asymmetry for the surrogates of bed elevation time series for the discharges of 1500 L/s, 2600 L/s, and 2800 L/s, respectively. The asymmetry of the surrogates shown here is the average asymmetry computed from the 50 surrogate series. The variability is shown via error bars which are one standard deviation from the mean values at each scale.

CHAPTER 6: SUMMARY AND CONCLUSION

Natural drainage networks emerge as an interplay between several external and internal factors such as climate, tectonics, and vegetation. Climate has been identified as one of the most significant controls on landscape evolution. Several studies revealed that drainage density is influenced by the long-term climate and has U-shape relationship between drainage density and climate [*Abrahams*, 1984; *Madduma Bandara*, 1974; *Melton*, 1957]. The U-shape relationship suggests that two different basins can exhibit similar drainage densities, although, in a different climate.

In chapter 2, we investigate the effects of different climatic conditions on structural patterns (geometry and topology) of river networks obtained from basins with varying climate aridity index but equal drainage density. The structure of the two-dimensional river network was translated into a one-dimensional space using the concept of width functions. This transformation enabled us to study network structure by focusing on the complexity of the width function quantified using a multiscale entropy framework.

Our analysis indicates that basins with dry climate have higher relative relief and higher channel concavity compared to humid basins. The dry basins exhibit higher entropy as compared to humid basins across several spatial scales. The higher entropy for dry basins suggests that dry basins, in general, contain a more complex organizational structure of river network over multiple scales. Higher entropy also suggests more heterogeneity of river network in dry basins. This heterogeneity is manifested in channels and their junctions resulting in larger junction angle, smaller junction density, and larger link length in dry

basins compared to humid basins. Given the fact that our study was focused on basins with equal drainage density, our observations clearly demonstrate that climate controls on drainage networks go beyond drainage density and cover several geometric and topologic features across multiple scales. In other words, by comparing basins with the same drainage density in very different climates, we show that it is not the drainage density which creates the network complexity but rather is the topology (arrangement of channels) together with geometry of the river network that create such complexity (see *Ranjbar et al.* [2018] for more details).

In chapter 3, we used numerical simulations to investigate the branching structure of the channel networks. The parameters of the simulated landscapes can represent variable climatic conditions. For example, higher D (diffusion coefficient) and K (advection coefficient) may represent humid climate whereas lower D and K may represent dry climate. These assumptions were verified from 100 basins across the United States located in various climatic conditions quantified via mean annual precipitation (MAP).

The initiation, evolution, and extent of a channel network is controlled by the competition between the advection and diffusion on a landscape controls and can be characterized by the ratio between the dimensionless diffusion and advection coefficients, commonly referred to as Péclet number, Pe. However, with different magnitude combinations of diffusion and advection coefficients, the same Pe and thus the same characteristic length scale can be obtained. Different magnitudes of diffusive and advective processes manifest themselves on the landscape with very different geomorphic and topologic properties.

In order to study the effect of changing climatic conditions on the channel network branching structure, we first simulated a landscape with a set of parameters (D, K, and m), referred to as original scenario, chosen based on a *Pe* equal to 2600. This value corresponds to the landscapes with branching channel networks (see *Perron et al.* [2008]). Keeping the ratio of D and K constant for the simulated landscapes, we performed two different sets of simulations referred to as humid and dry scenarios. For humid and dry scenarios, we increased (mimicking humid conditions) and decreased (mimicking dry conditions) both D and K systematically from 10 to 90% with increments of 10%, respectively. This way, the competition between the soil creep and fluvial incision was maintained the same, and simultaneously different climatic conditions were simulated. Different morphologic and topologic behaviors were observed for the simulated scenarios. A slightly lower mean relief was observed for the landscapes of humid scenario whereas a considerably higher mean relief was obtained for the landscapes in dry scenarios compared to the landscape in the original scenario. The signature of different climatic conditions was not limited to the changes in relief only; it was also manifested in the branching structure of the channel networks of the simulated landscapes. For the landscapes from humid conditions, a more side-branched channel structure was observed compared to the landscapes from dry conditions. These results are consistent with the observations from natural basins where the Tokunaga parameter, c-value (implying side-branching) increases with increasing precipitation.

From the above discussion, one can infer that landscapes with similar competition between the advective and diffusive processes might contain a completely distinct branching

channel network structure depending on the magnitudes of these processes. In other words, although the ratio between fluvial incision and soil creep (determined by the Pe) may be the same for different landscapes, the strength of these processes control the branching channel network structure of the landscapes, suggesting distinct signatures in different climatic conditions (for more details [*Ranjbar et al.*, 2020b] under consideration).

In chapter 4, we investigate the complexity of CN (i.e., complexity in channel organization and flux transport patterns) from 2 different perspectives. The complexity in channel organization and flux transport are referred to as the structural and functional complexity, respectively. Width function (W(x)) and incremental area function (IA(x)) are used to explore the influence of topology on structural and functional complexity. Tokunaga self-similarity model characterizes the topology of a CN by quantifying the degree of side-branching. An entropy-based approach that computes the repetition of patterns in series (here W(x) and IA(x)) and quantifies the degree of randomness at different spatial-scales was used to assess the variability of W(x) and IA(x). Based on our results, functional complexity is higher than structural complexity across scales. The additional complexity emerged in IA(x) is attributed to the effects of hillslope processes, since unlike W(x), IA(x) considers the information of hillslopes and CN organization patterns. Both structural and functional complexities are influenced by topology based on the increasing relationship between c-value and entropy at all considered spatial-scales. However, due to a larger $Slope_{E-c}$, functional complexity is more influenced by topology compared to the structural complexity. More specifically, for catchments with different side-branching degrees (i.e., c-value) the functional complexity may be significantly different compared to structural

complexity. The slope of increase in both structural and functional complexity versus topology increases with scales. The difference in the increase of slope with topology as a function of scales between W(x) and IA(x) also increases with scales and peaks at a spatial-scale of~ $45\ m$. The average hillslope length for the 40 natural catchments studied in here is 56.5 m which is similar to the scale of peak of slope difference for W(x) and IA(x) computed by the complexity analysis via multiscale entropy approach. This result suggests that indeed hillslopes contribute to higher complexity in catchments compared to CNs.

Finally, our analysis provides meaningful information (e.g. represented by the magnitude of difference between W(x) and IA(x) entropic contents) on how much hillslope-scale complexity should be accounted for in predictive modeling of hydrological processes at the catchment scale (for more details see *Ranjbar et al.* [2020a] under consideration).

In chapter 5, we investigate the underlying dynamics of rivers with varying flow conditions using their bed elevation time series. The data used in this study were collected from an experimental flume in the Main Channel facility at the St. Anthony Falls Laboratory at three distinct discharges of 1500, 2600, and 2800 L/s. The multiscale entropy (MSE) method is used to characterize the bed elevation fluctuations. Based on our results, bed elevations of higher discharges exhibit higher MSE compared to bed elevations of lower discharges. This indicates that the fluctuation pattern is more complex for the bed elevation of higher discharges compared to lower discharges suggesting that the bedform structure at higher discharge is less predictable compared with lower discharge and is attributed to both nonlinearity and linear correlation of the bed elevation series.

The surrogates of the bed elevation time series were computed using the IAAFT algorithm to further explore the factors contributing to this complexity. The IAAFT method destroys any inherent nonlinearity but preserves the linear correlation structure of the original series. A lower MSE is observed for surrogates compared to the original series. The difference between the MSEs of the original and surrogate bed elevation time series indicates the presence of nonlinearity in the bed elevation time series which is due to the distinct spatial arrangement of extreme heterogeneous fluctuations. This is consistent with the presence of intermittency, computed based on structure function analysis and indicates the relative contribution of inherent nonlinearity to the overall complexity. In other words, our results suggest that the entropy of bed elevation series across different scales is a function of both linear correlation and heterogeneous arrangement of fluctuations. We also show that the MSE of bed elevation surrogates is higher in the case of higher discharge compared to the lower discharge. This is related consistent with results of the spectral slope of PSD observed in Figure 20 where a higher spectral slope is observed for the bed elevation of higher discharges compared to the lower discharge. In addition, the asymmetry analysis of the bed elevation increments, suggests that the asymmetry may not contribute to the complexity directly. In summary, our complexity analysis can provide useful insights into various riverine processes and their interactions with river bed topography and can be further used for developing better predictive models of sediment transport. Our results indicate the amount of information on physical processes (e.g. multiscale migrating velocity, bedform height and bedform length variabilities) that should be included in the predictive modeling of sediment transport (for more details see *Ranjbar and Singh* [2020]). For

example, a higher entropy in bed elevation fluctuations at higher discharges indicates that for the accurate prediction of sediment transport at higher discharges one needs to account for multiscale variability in bedform characteristics [*Nikora and Hicks*, 1997]

Some interesting research directions for future work are listed below:

1. Explore the effects of initial conditions on basin formation and evolution. The ability of landscapes to preserve different types of drainage perturbation can be characterized throughout the evolution process as the memory of its initial condition.

2. Explore the role of variabilities in the ecosystem such as vegetation and biodiversity in rivers on the structural and functional complexities on channel networks. Also, the impact of changing climate and human activities can be considered explicitly by comparing the functional and structural complexities in catchments for example located in arid versus wet climate as well as comparing the river networks of natural versus urbanized areas which can be a subject for future studies.

3. The MSE approach has the potential to discern the signature of perennial and ephemeral streams of a river network based on flow duration curves [*Ghotbi et al.*, 2020]. In addition, the MSE approach can be used to explore the role of changing hydrologic forcing (e.g. hurricane and drought) on wetlands dynamics. Wetlands offer numerous imperative functions by supporting a large diversity of lifeforms and act as interacting tissues between upland (e.g. river networks) and coastal areas [*Sandhu et al.*, 2016; *Tahsin et al.*, 2020].

4. Using the stratigraphic data i.e. the spatial and temporal distribution of sedimentary layers, one could investigate the complexity in depositional patterns and the factors resulting in complexity such as bedforms.

REFERENCES

Abed-Elmdoust, A., M. A. Miri, and A. Singh (2016), Reorganization of river networks under changing spatiotemporal precipitation patterns: An optimal channel network approach, *Water Resources Research*, *52*(11), 8845-8860.

Abed-Elmdoust, A., A. Singh, and Z.-L. Yang (2017), Emergent spectral properties of river network topology: An optimal channel network approach, *Scientific Reports*, *7*(1), 1-9.

Abedin, P., S. Akbari, M. Demange, T. J. G. Ekim, and Combinatorics (2017), Complexity of the improper twin edge coloring of graphs, *33*(4), 595-615.

Abedin, P., A. Ganguly, W.-K. Hon, K. Matsuda, Y. Nekrich, K. Sadakane, R. Shah, and S. V. Thankachan (2020), A linear-space data structure for range-LCP queries in poly-logarithmic time, *Theoretical Computer Science*.

Aberle, J., and V. Nikora (2006), Statistical properties of armored gravel bed surfaces, *Water Resources Research*, *42*(11), W11414.

Abrahams, A. D. (1984), Channel networks: a geomorphological perspective, *Water Resources Research*, *20*(2), 161-188.

Abrahams, A. D., and J. J. Ponczynski (1984), Drainage density in relation to precipitation intensity in the USA, *Journal of Hydrology*, *75*(1-4), 383-388.

Arora, V. K. (2002), The use of the aridity index to assess climate change effect on annual runoff, *Journal of Hydrology*, *265*(1-4), 164-177.

Azami, H., A. Fernández, and J. Escudero (2017), Refined multiscale fuzzy entropy based on standard deviation for biomedical signal analysis, *Medical & Biological Engineering & Computing*, *55*(11), 2037-2052.

Basso, S., A. Frascati, M. Marani, M. Schirmer, and G. Botter (2015), Climatic and landscape controls on effective discharge, *Geophysical Research Letters*, *42*(20), 8441-8447.

Basu, S., E. Foufoula-Georgiou, B. Lashermes, and A. Arnéodo (2007), Estimating intermittency exponent in neutrally stratified atmospheric surface layer flows: a robust framework based on magnitude cumulant and surrogate analyses, *Physics of Fluids*, *19*(11), 115102.

Bertuzzo, E., S. Azaele, A. Maritan, M. Gatto, I. Rodriguez-Iturbe, and A. Rinaldo (2008), On the space-time evolution of a cholera epidemic, *Water Resources Research*, *44*(1), W01424.

Best, J. (2005), The fluid dynamics of river dunes: A review and some future research directions, *Journal of Geophysical Research: Earth Surface*, *110*(F4).

Biswal, B., and M. Marani (2010), Geomorphological origin of recession curves, *Geophysical Research Letters*, *37*(24), L24403.

Black, B. A., J. T. Perron, D. M. Burr, and S. A. Drummond (2012), Estimating erosional exhumation on Titan from drainage network morphology, *Journal of Geophysical Research: Planets*, *117*(E8).

Bonetti, S., M. Hooshyar, C. Camporeale, and A. Porporato (2020), Channelization cascade in landscape evolution, *Proceedings of the National Academy of Sciences*, *117*(3), 1375-1382.

Budyko, M. I. (1974), Climate and Life, 508 pp, edited, Academic Press, New York.

Casagrande, E., B. Mueller, D. G. Miralles, D. Entekhabi, and A. Molini (2015), Wavelet correlations to reveal multiscale coupling in geophysical systems, *Journal of Geophysical Research: Atmospheres*, *120*(15), 7555-7572.

Chaitin, G. J. (1975), Randomness and mathematical proof, *Scientific American*, *232*(5), 47-53.

Chembolu, V., and S. Dutta (2016), Entropy and energy dissipation of a braided river system, *Procedia Engineering*, *144*, 1175-1179.

Chen, W., Z. Wang, H. Xie, and W. Yu (2007), Characterization of surface EMG signal based on fuzzy entropy, *IEEE Transactions on Neural Systems and Rehabilitation Engineering*, *15*(2), 266-272.

Collins, D., and R. Bras (2010), Climatic and ecological controls of equilibrium drainage density, relief, and channel concavity in dry lands, *Water Resources Research*, *46*, W04508.

Convertino, M., R. Rigon, A. Maritan, I. Rodriguez-Iturbe, and A. Rinaldo (2007), Probabilistic structure of the distance between tributaries of given size in river networks, *Water Resources Research*, *43*(11), W11418.

Costa, M., A. L. Goldberger, and C.-K. Peng (2002), Multiscale entropy analysis of complex physiologic time series, *Physical Review Letters*, *89*(6), 068102.

Costa, M., A. L. Goldberger, and C.-K. Peng (2005), Multiscale entropy analysis of biological signals, *Physical Review E*, *71*(2), 021906.

Cui, G., B. Williams, and G. Kuczera (1999), A stochastic Tokunaga model for stream networks, *Water Resources Research*, *35*(10), 3139-3147.

Czuba, J. A., and E. Foufoula-Georgiou (2015), Dynamic connectivity in a fluvial network for identifying hotspots of geomorphic change, *Water Resources Research*, *51*(3), 1401-1421.

Delgado-Bonal, A., and A. Marshak (2019), Approximate entropy and sample entropy: A comprehensive tutorial, *Entropy*, *21*(6), 541.

Devauchelle, O., A. P. Petroff, H. F. Seybold, and D. H. Rothman (2012), Ramification of stream networks, *Proceedings of the National Academy of Sciences*, *109*(51), 20832-20836.

Dietrich, W. E., and T. Dunne (1993), The channel head, in *Channel Network Hydrology*, edited by K. Beven and M. J. Kirkby, pp. 175-219, Wiley, New York.

Dietrich, W. E., C. J. Wilson, D. R. Montgomery, and J. McKean (1993), Analysis of erosion thresholds, channel networks, and landscape morphology using a digital terrain model, *The Journal of Geology*, *101*(2), 259-278.

Dietrich, W. E., D. G. Bellugi, L. S. Sklar, J. D. Stock, A. M. Heimsath, and J. J. Roering (2003), Geomorphic transport laws for predicting landscape form and dynamics, *Prediction in Geomorphology*, *135*, 103-132.

Drake, T. G., R. L. Shreve, W. E. Dietrich, P. J. Whiting, and L. B. Leopold (1988), Bedload transport of fine gravel observed by motion-picture photography, *Journal of Fluid Mechanics*, *192*, 193-217.

Duncan, W. W., G. C. Poole, and J. L. Meyer (2009), Large channel confluences influence geomorphic heterogeneity of a southeastern United States river, *Water Resources Research*, *45*(10), W10405.

Ebrahimi, N., E. Maasoumi, and E. S. Soofi (1999), Ordering univariate distributions by entropy and variance, *Journal of Econometrics*, *90*(2), 317-336.

Ferrier, K. L., K. L. Huppert, and J. T. Perron (2013), Climatic control of bedrock river incision, *Nature*, *496*(7444), 206-209.

Fiorentino, M., P. Claps, and V. P. Singh (1993), An entropy-based morphological analysis of river basin networks, *Water Resources Research*, *29*(4), 1215-1224.

Gangodagamage, C., P. Belmont, and E. Foufoula-Georgiou (2011), Revisiting scaling laws in river basins: New considerations across hillslope and fluvial regimes, *Water Resources Research*, *47*(7), W07508.

Gangodagamage, C., E. Foufoula-Georgiou, and P. Belmont (2014), River basin organization around the main stem: Scale invariance in tributary branching and the incremental area function, *Journal of Geophysical Research: Earth Surface*, *119*(10), 2174-2193.

Ghotbi, S., D. Wang, A. Singh, G. Blöschl, and M. Sivapalan (2020), A New Framework for Exploring Process Controls of Flow Duration Curves, *Water Resources Research*, e2019WR026083.

Gilbert, G. K. (1877), Report on the Geology of the Henry mountains, Government Printing Office, Washington, D. C.

Goodwell, A., and P. Kumar (2017), Temporal Information Partitioning Networks (TIPNets): Characterizing emergent behavior in complex ecohydrologic systems, paper presented at EGU General Assembly Conference Abstracts.

Goren, L. (2016), A theoretical model for fluvial channel response time during time‐dependent climatic and tectonic forcing and its inverse applications, *Geophysical Research Letters*, *43*, 10,753–710,763.

Grieve, S. W., S. M. Mudd, and M. D. Hurst (2016), How long is a hillslope?, *Earth Surface Processes and Landforms*, *41*(8), 1039-1054.

Gupta, V. K., and O. J. Mesa (1988), Runoff generation and hydrologic response via channel network geomorphology—Recent progress and open problems, *Journal of Hydrology*, *102*(1-4), 3-28.

Hack, J. T. (1957), *Studies of longitudinal stream profiles in Virginia and Maryland*, Geological Survey Professional Paper, 294- B.

Han, J., N. M. Gasparini, and J. P. Johnson (2015), Measuring the imprint of orographic rainfall gradients on the morphology of steady-state numerical fluvial landscapes, *Earth Surface Processes and Landforms*, *40*(10), 1334-1350.

Han, J., N. M. Gasparini, J. P. Johnson, and B. P. Murphy (2014), Modeling the influence of rainfall gradients on discharge, bedrock erodibility, and river profile evolution, with application to the Big Island, Hawai'i, *Journal of Geophysical Research: Earth Surface*, *119*(6), 1418-1440.

Hanks, T. C. (2000), The age of scarplike landforms from diffusion-equation analysis, *Quaternary Geochronology: Methods and Applications*, *4*, 313-338.

Hansen, A., and A. Singh (2018), High-frequency sensor data reveal across-scale nitrate dynamics in response to hydrology and biogeochemistry in intensively managed agricultural basins, *Journal of Geophysical Research: Biogeosciences*, *123*(7), 2168-2182.

Hooshmand, S., P. Abedin, M. O. Külekci, and S. V. Thankachan (2018), Non-Overlapping Indexing-Cache Obliviously, paper presented at Annual Symposium on Combinatorial Pattern Matching (CPM 2018), Schloss Dagstuhl-Leibniz-Zentrum fuer Informatik.

Hooshyar, M., A. Singh, and D. Wang (2017), Hydrologic controls on junction angle of river networks, *Water Resources Research*, *53*(5), 4073-4083.

Hooshyar, M., A. Singh, and D. Wang (2019a), Interbasin and Intrabasin Competitions Control Drainage Network Density, *Geophysical Research Letters*, *46*, 661-669.

Hooshyar, M., A. Singh, D. Wang, and E. Foufoula-Georgiou (2019b), Climatic controls on landscape dissection and network structure in the absence of vegetation, *Geophysical Research Letters*, *46*(6), 3216-3224.

Hooshyar, M., D. Wang, S. Kim, S. C. Medeiros, and S. C. Hagen (2016), Valley and channel networks extraction based on local topographic curvature and k-means clustering of contours, *Water Resources Research*, *52*(10), 8081-8102.

Horton, R. E. (1932), Drainage-basin characteristics, *Eos, Transactions American Geophysical Union*, *13*(1), 350-361.

Horton, R. E. (1945), Erosional development of streams and their drainage basins; hydrophysical approach to quantitative morphology, *Geological Society of America Bulletin*, *56*(3), 275-370.

Hosking, J. R. (1981), Fractional differencing, *Biometrika*, *68*(1), 165-176.

Howard, A. D. (1994), A detachment-limited model of drainage basin evolution, *Water Resources Research*, *30*(7), 2261-2285.

Hurst, M. D., S. M. Mudd, K. Yoo, M. Attal, and R. Walcott (2013), Influence of lithology on hillslope morphology and response to tectonic forcing in the northern Sierra Nevada of California, *Journal of Geophysical Research: Earth Surface*, *118*(2), 832-851.

Istanbulluoglu, E., and R. L. Bras (2005), Vegetation-modulated landscape evolution: Effects of vegetation on landscape processes, drainage density, and topography, *Journal of Geophysical Research: Earth Surface*, *110*, F02012.

Kelly, S. A., Z. Takbiri, P. Belmont, and E. Foufoula-Georgiou (2016), Human amplified changes in precipitation-runoff patterns in large river basins of the Midwestern United States, *Hydrology and Earth System Sciences*, *21*, 5065-5088.

Keylock, C. J. (2012), A resampling method for generating synthetic hydrological time series with preservation of cross-correlative structure and higher-order properties, *Water Resources Research*, *48*(12), W12521.

Keylock, C. J., A. Singh, and E. Foufoula-Georgiou (2014), The complexity of gravel bed river topography examined with gradual wavelet reconstruction, *Journal of Geophysical Research: Earth Surface*, *119*(3), 682-700.

Kirchner, J. W. (1993), Statistical inevitability of Horton's laws and the apparent randomness of stream channel networks, *Geology*, *21*(7), 591-594.

Kirkby, M. (1971), Hillslope process-response models based on the continuity equation, *Institute of British Geographers Special Publication*, *3*(1), 5-30.

Kirkby, M. (1976), Tests of the random network model, and its application to basin hydrology, *Earth Surface Processes and Landforms*, *1*(3), 197-212.

Kirkby, M. (1987), Modelling some influences of soil erosion, landslides and valley gradient on drainage density and hollow development, *Catena Supplement*, *10*, 1-11.

Knudby, C., and J. Carrera (2005), On the relationship between indicators of geostatistical, flow and transport connectivity, *Advances in Water Resources*, *28*(4), 405-421.

Larsen, L. G., J. Choi, M. K. Nungesser, and J. W. Harvey (2012), Directional connectivity in hydrology and ecology, *Ecological Applications*, *22*(8), 2204-2220.

Lashermes, B., and E. Foufoula-Georgiou (2007), Area and width functions of river networks: New results on multifractal properties, *Water Resources Research*, *43*(9), W09405.

Lashermes, B., E. Foufoula-Georgiou, and W. E. Dietrich (2007), Channel network extraction from high resolution topography using wavelets, *Geophysical Research Letters*, *34*(23), L23S04.

Leopold, L. (1971), Trees and streams: the efficiency of branching patterns, *Journal of Theoretical Biology*, *31*(2), 339-354.

Leopold, L., and W. B. Langbein (1962), The concept of entropy in landscape evolution, *U.S. Geological Survey Professional Paper*, *500A*.

Liu, B., X. Chen, Y. Lian, and L. Wu (2013), Entropy-based assessment and zoning of rainfall distribution, *Journal of Hydrology*, *490*, 32-40.

Madduma Bandara, C. M. (1974), Drainage density and effective precipitation, *Journal of Hydrology*, *21*(2), 187-190.

Malecot, Y., C. Auriault, H. Kahalerras, Y. Gagne, O. Chanal, B. Chabaud, and B. Castaing (2000), A statistical estimator of turbulence intermittency in physical and numerical experiments, *The European Physical Journal B-Condensed Matter*

Complex Systems, *16*(3), 549-561.

Mandelbrot, B. B., and J. W. Van Ness (1968), Fractional Brownian motions, fractional noises and applications, *SIAM Review*, *10*(4), 422-437.

Marani, M., A. Rinaldo, R. Rigon, and I. Rodriguez-Iturbe (1994), Geomorphological width functions and the random cascade, *Geophysical Research Letters*, *21*(19), 2123-2126.

Marion, A., S. J. Tait, and I. K. McEwan (2003), Analysis of small-scale gravel bed topography during armoring, *Water Resources Research*, *39*(12), 1334.

Mcconnell, M., and V. K. Gupta (2008), A proof of the Horton law of stream numbers for the Tokunaga model of river networks, *Fractals*, *16*(03), 227-233.

McElroy, B., and D. Mohrig (2009), Nature of deformation of sandy bed forms, *Journal of Geophysical Research: Earth Surface*, *114*(F3).

Melton, M. A. (1957), An analysis of the relations among elements of climate, surface properties, and geomorphology, Columbia University of New York.

Mishra, A. K., M. Özger, and V. P. Singh (2009), An entropy-based investigation into the variability of precipitation, *Journal of Hydrology*, *370*(1-4), 139-154.

Moglen, G. E., E. A. B. Eltahir, and R. L. Bras (1998), On the sensitivity of drainage density to climate change, *Water Resources Research*, *34*(4), 855-862.

Molnar, P. (2001), Climate change, flooding in arid environments, and erosion rates, *Geology*, *29*(12), 1071-1074.

Montgomery, D. R., and W. E. Dietrich (1992), Channel initiation and the problem of landscape scale, *Science*, *255*(5046), 826-830.

Montgomery, D. R., and E. Foufoula-Georgiou (1993), Channel network source representation using digital elevation models, *Water Resources Research*, *29*(12), 3925-3934.

Moussa, R. (2008), What controls the width function shape, and can it be used for channel network comparison and regionalization?, *Water Resources Research*, *44*(8), W08456.

Mutlu, E. C., T. A. Oghaz, A. Rajabi, and I. Garibay (2019), Review on graph feature learning and feature extraction techniques for link prediction, *arXiv preprint arXiv:.03425*.

Nelson, J. M., S. R. McLean, and S. R. Wolfe (1993), Mean flow and turbulence fields over two‐dimensional bed forms, *Water Resources Research*, *29*(12), 3935-3953.

Nikora, V., and D. M. Hicks (1997), Scaling relationships for sand wave development in unidirectional flow, *Journal of Hydraulic Engineering*, *123*(12), 1152-1156.

Nikora, V., and J. Walsh (2004), Water‐worked gravel surfaces: High‐order structure functions at the particle scale, *Water Resources Research*, *40*(12), W12601.

Nikora, V., H. Habersack, T. Huber, and I. McEwan (2002), On bed particle diffusion in gravel bed flows under weak bed load transport, *Water Resources Research*, *38*(6), 17-11-17-19.

Nourani, V., M. T. Alami, and F. D. Vousoughi (2015), Wavelet-entropy data pre-processing approach for ANN-based groundwater level modeling, *Journal of Hydrology*, *524*, 255-269.

Oguchi, T. (1997), Drainage density and relative relief in humid steep mountains with frequent slope failure, *Earth Surface Processes and Landforms: The Journal of the British Geomorphological Group*, *22*(2), 107-120.

Orlandini, S., C. Boaretti, V. Guidi, and G. Sfondrini (2006), Field determination of the spatial variation of resistance to flow along a steep Alpine stream, *Hydrological Processes: An International Journal*, *20*(18), 3897-3913.

Orlandini, S., P. Tarolli, G. Moretti, and G. Dalla Fontana (2011), On the prediction of channel heads in a complex alpine terrain using gridded elevation data, *Water Resources Research*, *47*(2), W02538.

Paik, K., and P. Kumar (2010), Optimality approaches to describe characteristic fluvial patterns on landscapes, *Philosophical Transactions of the Royal Society B: Biological Sciences*, *365*(1545), 1387-1395.

Parisi, G., and U. Frisch (1985), On the singularity structure of fully developed turbulence, *Turbulence and predictability in geophysical fluid dynamics and climate dynamics, North-Holland*, 84-87.

Passalacqua, P., T. Do Trung, E. Foufoula-Georgiou, G. Sapiro, and W. E. Dietrich (2010), A geometric framework for channel network extraction from lidar: Nonlinear diffusion and geodesic paths, *Journal of Geophysical Research: Earth Surface*, *115*(F1), F01002.

Peckham, S. D. (1995), New results for self‐similar trees with applications to river networks, *Water Resources Research*, *31*(4), 1023-1029.

Peckham, S. D., and V. K. Gupta (1999), A reformulation of Horton's laws for large river networks in terms of statistical self‐similarity, *Water Resources Research*, *35*(9), 2763-2777.

Perona, P., and J. Malik (1990), Scale-space and edge detection using anisotropic diffusion, *IEEE Transactions on pattern analysis and machine intelligence*, *12*(7), 629-639.

Perron, J. T. (2017), Climate and the pace of erosional landscape evolution, *Annual Review of Earth and Planetary Sciences*, *45*, 561–591.

Perron, J. T., W. E. Dietrich, and J. W. Kirchner (2008), Controls on the spacing of first‐order valleys, *Journal of Geophysical Research: Earth Surface*, *113*(F4), F04016.

Perron, J. T., J. W. Kirchner, and W. E. Dietrich (2009), Formation of evenly spaced ridges and valleys, *Nature*, *460*(7254), 502–505.

Perron, J. T., P. W. Richardson, K. L. Ferrier, and M. Lapôtre (2012), The root of branching river networks, *Nature*, *492*(7427), 100-103.

Pincus, S. M. (1991), Approximate entropy as a measure of system complexity, *Proceedings of the National Academy of Sciences*, *88*(6), 2297-2301.

Ponce, V. M., R. P. Pandey, and S. Ercan (2000), Characterization of drought across climatic spectrum, *Journal of Hydrologic Engineering*, *5*(2), 222-224.

Porporato, A., J. Rigby, and E. Daly (2007), Irreversibility and fluctuation theorem in stationary time series, *Physical Review Letters*, *98*(9), 094101.

Rajabi, A. (2018), Sinkhole Detection and Quantification Using LiDAR Data, University of Central Florida, Orlando, FL.

Rajabi, A., Y. Kim, S.-H. Kim, Y. Kim, B. Kim, and B. H. Nam (2018), A Preliminary Study on Use of LiDAR Data to Characterize Sinkholes in Central Florida, in *IFCEE* edited, pp. 23-31.

Ranjbar, S., and A. Singh (2020), Entropy and Intermittency of River Bed Elevation Fluctuations, *Journal of Geophysical Research: Earth Surface*, *125*, e2019JF005499, DOI:005410.001029/002019JF005499.

Ranjbar, S., A. Singh, and D. Wang (2020a), Controls of the Topological Connectivity on the Structural and Functional Complexity of River Networks, *Geophysical Research Letters*, Under Review.

Ranjbar, S., A. Singh, and D. Wang (2020b), Signatures of varying climate on geomorphic and topologic characteristics of channel networks, *Water Resources Research*, Under Review.

Ranjbar, S., M. Hooshyar, A. Singh, and D. Wang (2018), Quantifying climatic controls on river network branching structure across scales, *Water Resources Research*, *54*(10), 7347-7360.

Richards-Pecou, B. (2002), Scale invariance analysis of channel network width function and possible implications for flood behaviour, *Hydrological Sciences Journal*, *47*(3), 387-404.

Richardson, P. W., J. T. Perron, and N. D. Schurr (2019), Influences of climate and life on hillslope sediment transport, *Geology*, *47*(5), 423-426.

Richman, J. S., and J. R. Moorman (2000), Physiological time-series analysis using approximate entropy and sample entropy, *American Journal of Physiology-Heart and Circulatory Physiology*, *278*(6), H2039-H2049.

Rigon, R., I. Rodriguez-Iturbe, and A. Rinaldo (1998), Feasible optimality implies Hack's law, *Water Resources Research*, *34*(11), 3181-3189.

Rigon, R., I. Rodriguez-Iturbe, A. Maritan, A. Giacometti, D. G. Tarboton, and A. Rinaldo (1996), On Hack's law, *Water Resources Research*, *32*(11), 3367-3374.

Rinaldo, A., W. E. Dietrich, R. Rigon, G. K. Vogel, and I. Rodrlguez-Iturbe (1995a), Geomorphological signatures of varying climate, *Nature*, *374*(6523), 632-635.

Rinaldo, A., W. E. Dietrich, R. Rigon, G. K. Vogel, and I. Rodrlguez-Iturbe (1995b), Geomorphological signatures of varying climate, *Nature*, *374*(6523), 632–635.

Rodriguez-Iturbe, I., and J. B. Valdes (1979), The geomorphologic structure of hydrologic response, *Water Resources Research*, *15*(6), 1409-1420.

Rodriguez-Iturbe, I., and A. Rinaldo (2001), *Fractal river basins: chance and self-organization*, Cambridge University Press.

Rodriguez-Iturbe, I., M. Marani, R. Rigon, and A. Rinaldo (1994), Self‐organized river basin landscapes: Fractal and multifractal characteristics, *Water Resources Research*, *30*(12), 3531-3539.

Rodriguez-Iturbe, I., R. Muneepeerakul, E. Bertuzzo, S. A. Levin, and A. Rinaldo (2009), River networks as ecological corridors: A complex systems perspective for integrating hydrologic, geomorphologic, and ecologic dynamics, *Water Resources Research*, *45*(1), W01413.

Rodríguez‐Iturbe, I., and J. B. Valdes (1979), The geomorphologic structure of hydrologic response, *Water Resources Research*, *15*(6), 1409-1420.

Roering, J. J., J. W. Kirchner, and W. E. Dietrich (2001), Hillslope evolution by nonlinear, slope‐dependent transport: Steady state morphology and equilibrium adjustment timescales, *Journal of Geophysical Research: Solid Earth*, *106*(B8), 16499-16513.

Sandhu, D., A. Singh, N. Fan, D. Wang, and S. Duranceau (2016), Hydro-geomorphic response of Everglades to changing climate and anthropogenic activities, *Journal of Hydrology*, *543*, 861-872.

Sangireddy, H., R. A. Carothers, C. P. Stark, and P. Passalacqua (2016), Controls of climate, topography, vegetation, and lithology on drainage density extracted from high resolution topography data, *Journal of Hydrology*, *537*, 271-282.

Sarker, S., A. Veremyev, V. Boginski, and A. Singh (2019), Critical nodes in river networks, *Scientific Reports*, *9*(1), 1-11.

Schreiber, T., and A. Schmitz (1996), Improved surrogate data for nonlinearity tests, *Physical Review Letters*, *77*(4), 635.

Schumm, S. A. (1956), Evolution of drainage systems and slopes in badlands at Perth Amboy, New Jersey, *Geological society of America Bulletin*, *67*(5), 597-646.

Seybold, H., D. H. Rothman, and J. W. Kirchner (2017), Climate's watermark in the geometry of stream networks, *Geophysical Research Letters*, *44*(5), 2272-2280.

Shannon, C. (1948), A Mathematical Theory of Communication, *Bell System Technical Journal*, *27*, 379-423 & 623-656.

Shelef, E. (2018), Channel Profile and Plan‐View Controls on the Aspect Ratio of River Basins, *Geophysical Research Letters*, *45*(21), 11,712-711,721.

Shelef, E., and G. E. Hilley (2014), Symmetry, randomness, and process in the structure of branched channel networks, *Geophysical Research Letters*, *41*(10), 3485-3493.

Singh, A., S. Lanzoni, and E. Foufoula-Georgiou (2009a), Nonlinearity and complexity in gravel bed dynamics, *Stochastic Environmental Research and Risk Assessment*, *23*(7), 967-975.

Singh, A., L. Reinhardt, and E. Foufoula-Georgiou (2015), Landscape reorganization under changing climatic forcing: Results from an experimental landscape, *Water Resources Research*, *51*(6), 4320-4337.

Singh, A., S. Lanzoni, P. R. Wilcock, and E. Foufoula-Georgiou (2011), Multiscale statistical characterization of migrating bed forms in gravel and sand bed rivers, *Water Resources Research*, *47*(12), W12526.

Singh, A., E. Foufoula-Georgiou, F. Porté-Agel, and P. R. Wilcock (2012a), Coupled dynamics of the co‐evolution of gravel bed topography, flow turbulence and sediment transport in an experimental channel, *Journal of Geophysical Research: Earth Surface*, *117*(F4), F04016.

Singh, A., M. Guala, S. Lanzoni, and E. Foufoula-Georgiou (2012b), Bedform effect on the reorganization of surface and subsurface grain size distribution in gravel bedded channels, *Acta Geophysica*, *60*(6), 1607-1638.

Singh, A., K. Fienberg, D. J. Jerolmack, J. Marr, and E. Foufoula-Georgiou (2009b), Experimental evidence for statistical scaling and intermittency in sediment transport rates, *Journal of Geophysical Research: Earth Surface*, *114*(F1).

Singh, A., J. A. Czuba, E. Foufoula-Georgiou, J. D. Marr, C. Hill, S. Johnson, C. Ellis, J. Mullin, C. H. Orr, and P. R. Wilcock (2013), StreamLab Collaboratory: Experiments, data sets, and research synthesis, *Water Resources Research*, *49*(3), 1746-1752.

Singh, V. P. (1997), The use of entropy in hydrology and water resources, *Hydrological Processes*, *11*(6), 587-626.

Sivapalan, M. (2003), Process complexity at hillslope scale, process simplicity at the watershed scale: is there a connection?, *Hydrological Processes*, *17*(5), 1037-1041.

Smart, G., J. Aberle, M. Duncan, and J. Walsh (2004), Measurement and analysis of alluvial bed roughness, *Journal of Hydraulic Research*, *42*(3), 227-237.

Smith, T. R., and F. P. Bretherton (1972), Stability and the conservation of mass in drainage basin evolution, *Water Resources Research*, *8*(6), 1506-1529.

Snell, J. D., and M. Sivapalan (1994), On geomorphological dispersion in natural catchments and the geomorphological unit hydrograph, *Water Resources Research*, *30*(7), 2311-2323.

Stoica, P., and R. L. Moses (1997), Introduction to spectral analysis, Prentice hall Upper Saddle River, NJ.

Strahler, A. (1952), Hypsometric (area altitude) analysis of erosional topology, *Geological Society of America Bulletin*, *63*, 1117-1142.

Strahler, A. (1957), Quantitative analysis of watershed geomorphology, *Eos, Transactions American Geophysical Union*, *38*(6), 913-920.

Tahsin, S., S. C. Medeiros, and A. Singh (2020), Wetland Dynamics Inferred from Spectral Analyses of Hydro-Meteorological Signals and Landsat Derived Vegetation Indices, *Remote Sensing*, *12*(1), 12.

Tarboton, D. G. (1996), Fractal river networks, Horton's laws and Tokunaga cyclicity, *Journal of Hydrology*, *187*(1-2), 105-117.

Tarboton, D. G. (1997), A new method for the determination of flow directions and upslope areas in grid digital elevation models, *Water Resources Research*, *33*(2), 309-319.

Tarboton, D. G., R. L. Bras, and I. Rodriguez-Iturbe (1988), The fractal nature of river networks, *Water Resources Research*, *24*(8), 1317-1322.

Taylor, J. (1997), *Introduction to error analysis, the study of uncertainties in physical measurements*, University Science Books, Sausalito, California.

Tejedor, A., A. Longjas, I. Zaliapin, and E. Foufoula-Georgiou (2015), Delta channel networks: 2. Metrics of topologic and dynamic complexity for delta comparison, physical inference, and vulnerability assessment, *Water Resources Research*, *51*(6), 4019-4045.

Tejedor, A., A. Singh, I. Zaliapin, A. L. Densmore, and E. Foufoula-Georgiou (2017a), Scale-dependent erosional patterns in steady-state and transient-state landscapes, *Science Advances*, *3*(9), e1701683.

Tejedor, A., A. Longjas, D. A. Edmonds, I. Zaliapin, T. T. Georgiou, A. Rinaldo, and E. Foufoula-Georgiou (2017b), Entropy and optimality in river deltas, *Proceedings of the National Academy of Sciences*, 201708404.

Tokunaga, E. (1966), The composition of drainage network in Toyohira River Basin and valuation of Horton's first law, *Geophysical Bulletin of Hokkaido University*, *15*, 1-19.

Tokunaga, E. (1978), Consideration on the composition of drainage networks and their evolution, *Geographical Reporst of Tokyo Metropolitan University*, *13*, 1-27.

Troch, P. A., G. F. Martinez, V. Pauwels, M. Durcik, M. Sivapalan, C. Harman, P. D. Brooks, H. V. Gupta, and T. Huxman (2009), Climate and vegetation water use efficiency at catchment scales, *Hydrological Processes*, *23*(16), 2409-2414.

Troutman, B. M., and M. R. Karlinger (1984), On the expected width function for topologically random channel networks, *Journal of Applied Probability*, *21*(4), 836-849.

Troutman, B. M., and M. R. Karlinger (1985), Unit hydrograph approximations assuming linear flow through topologically random channel networks, *Water Resources Research*, *21*(5), 743-754.

Tucker, G. E., and R. Slingerland (1997), Drainage basin responses to climate change, *Water Resources Research*, *33*(8), 2031-2047.

Tucker, G. E., and R. L. Bras (1998), Hillslope processes, drainage density, and landscape morphology, *Water Resources Research*, *34*(10), 2751-2764.

Tucker, G. E., F. Catani, A. Rinaldo, and R. L. Bras (2001), Statistical analysis of drainage density from digital terrain data, *Geomorphology*, *36*(3-4), 187-202.

Turcotte, D., J. Pelletier, and W. Newman (1998), Networks with side branching in biology, *Journal of Theoretical Biology*, *193*(4), 577-592.

Veitzer, S. A., and V. K. Gupta (2000), Random self‐similar river networks and derivations of generalized Horton laws in terms of statistical simple scaling, *Water Resources Research*, *36*(4), 1033-1048.

Veitzer, S. A., and V. K. Gupta (2001), Statistical self-similarity of width function maxima with implications to floods, *Advances in Water Resources*, *24*(9-10), 955-965.

Wagener, T., M. Sivapalan, P. A. Troch, B. L. McGlynn, C. J. Harman, H. V. Gupta, P. Kumar, P. S. C. Rao, N. B. Basu, and J. S. Wilson (2010), The future of hydrology: An evolving science for a changing world, *Water Resources Research*, *46*(5), W05301.

Wang, D., and Y. Tang (2014), A one‐parameter Budyko model for water balance captures emergent behavior in Darwinian hydrologic models, *Geophysical Research Letters*, *41*(13), 4569-4577.

Willett, S. D., S. W. McCoy, J. T. Perron, L. Goren, and C.-Y. Chen (2014), Dynamic reorganization of river basins, *Science*, *343*(6175), 1248765.

Willgoose, G., R. L. Bras, and I. Rodriguez-Iturbe (1991), Results from a new model of river basin evolution, *Earth Surface Processes and Landforms*, *16*(3), 237-254.

Wong, M., and G. J. J. o. H. E. Parker (2006), Reanalysis and correction of bed-load relation of Meyer-Peter and Müller using their own database, *132*(11), 1159-1168.

Wrzesiński, D. J. A. G. (2016), Use of entropy in the assessment of uncertainty of river runoff regime in Poland, *64*(5), 1825-1839.

Yang, S., K. Paik, G. S. McGrath, C. Urich, E. Krueger, P. Kumar, and P. S. C. Rao (2017), Functional topology of evolving urban drainage networks, *Water Resources Research*, *53*(11), 8966-8979.

Yao, L., D. Wang, M. Hooshyar, A. Singh, and M. Sivapalan (2018), Time Compression Approximation Relationship for Infiltration in the Presence of a Shallow Water Table: Evaluating the Role of Péclet Number, *Water Resources Research*, *54*(11), 9384-9397.

Zadeh, L. A. (1965), Information and control, *Fuzzy Sets*, *8*(3), 338-353.

Zaliapin, I., E. Foufoula-Georgiou, and M. Ghil (2010), Transport on river networks: A dynamic tree approach, *Journal of Geophysical Research: Earth Surface*, *115*(F2), F00A15.

Zanardo, S., I. Zaliapin, and E. Foufoula-Georgiou (2013), Are American rivers Tokunaga self‐similar? New results on fluvial network topology and its climatic dependence, *Journal of Geophysical Research: Earth Surface*, *118*(1), 166-183.

Zomer, R. J., D. A. Bossio, A. Trabucco, L. Yuanjie, D. C. Gupta, and V. P. Singh (2007), *Trees and water: smallholder agroforestry on irrigated lands in Northern India*, IWMI.